THE UNIVERSITY OF ADELAIDE

School of Electrical and Electronic Engineering

Analysis and Modelling of the Effects of Inertia and Parameter Errors on Wind Turbine Output Power

Chun Tang

A thesis presented for the degree of Master of Engineering Science

2009

Dedicated to my late grandmother, Honghui Xu

THE UNIVERSITY
OF ADELAIDE
AUSTRALIA

Analysis and Modelling of the Effects of Inertia and Parameter Errors on Wind Turbine Output Power

Chun Tang

Submitted for the degree of Master of Engineering Science
2009

Abstract

Wind energy is an important renewable energy source. The average output power of a wind turbine is one of the main concerns in wind generation systems. The factors which affect the average output power include the location, the wind characteristics, the design of the blades and the control system etc. In this thesis, the effects of the inertia of a wind turbine under dynamic wind speed conditions, and the effects of the parameter errors under steady-state operation on the average output power are examined.

Maximum power point tracking is used to control the generator of a wind turbine in order to maximise the electrical output power of the wind turbine. However, under rapidly changing wind conditions, the output power of the wind turbines is reduced due to their inertia preventing them operating at the optimal turbine speed. Limited research into analysing this power reduction has been performed. Even under steady-state operating conditions, the maximum power coefficient and the optimal tip-speed ratio of the wind turbine generally need to be known for maximum power point tracking. Errors in the estimated parameters will result in an output power reduction for the wind turbine.

Therefore, an understanding of the sensitivity of wind turbine blade parameter errors to the output power reduction under steady-state conditions of wind turbines is also a significant issue.

The first part of the work in this thesis investigates the wind turbine output power reduction due to inertia under dynamic wind speed conditions. It is assumed that the wind turbine blade characteristics is known accurately and that a maximum power point strategy based on controlling the generator input torque as a function of generator speed is used (optimal torque control). The concept of the small-signal turbine time constant is introduced to denote the time constant of the response of a wind turbine for a small change in wind speed under the maximum power point operating conditions. It is shown that the turbine time constant is inversely proportional to the average wind speed, and the natural time constant is defined as the turbine time constant at the rated wind speed. An analytical equation for the small-signal output power reduction of a wind turbine with infinite inertia is then derived as the function of the ratio of the variance to the square of the average wind speed. For the small-signal finite inertia case, a scaling factor is added which is a function of the turbine time constant at the average wind speed and the “equivalent frequency” of the wind speed variations. Real wind speed data is utilised to test the analytical equation against simulation results for the power reduction with both infinite and finite inertia. As the wind speed profiles are not small-signal variations, the analytical results do not accurately predict the actual power reductions. The analytical results however provide useful physical insights into the differences in the power reductions with the different wind speed profiles and turbine inertia. Finally, some limited experimental measurements of the time-constant of a turbine are performed.

The second part of the work in this thesis investigates the effect of wind turbine blade parameter errors on the steady-state output power of a wind turbine. Two types of maximum power point tracking control strategies are investigated: constant tip-speed ratio control and optimal torque control. The analysis is carried out for a particular wind turbine blade characteristic. The steady-state output power reduction with errors in the maximum power coefficient and the optimal tip-speed ratio is shown graphically and compared for the two control strategies.

Statement of Originality

This work contains no material that has been accepted for the award of any other degree or diploma in any university or other tertiary institution and, to the best of my knowledge and belief, contains no material previously published or written by another person, except where due reference has been made in the text.

I give consent to this copy of the thesis, when deposited in the University Library, being available for loan, photocopying, and dissemination through the library digital thesis collection, subject to the provisions of the Copyright Act 1968.

I also give permission for the digital version of my thesis to be made available on the web, via the University's digital research repository, the Library catalogue, the Australasian Digital Thesis Program (ADTP) and also through web search engines, unless permission has been granted by the University to restrict access for a period of time. The author acknowledges that copyright of published works contained within this thesis (as listed below) resides with the copyright holder(s) of those works.

List of Publications

[P1] C. Tang, M. Pathmanathan, W.L. Soong and N. Ertugrul, “Effects of Inertia on Dynamic Performance of Wind Turbines,” Australasian Universities Power Engineering Conference, AUPEC, Sydney 2008.

[P2] M. Pathmanathan, C. Tang, W.L. Soong, N. Ertugrul, “Comparison of power converters for small-scale wind turbine operation”, Australasian Universities Power Engineering Conference, AUPEC, Sydney 2008.

[P3] M. Pathmanathan, C. Tang, W.L. Soong, N. Ertugrul,, “Detailed investigation of semi-bridge switched-mode rectifier for small-scale wind turbine applications”, IEEE International Conference on Sustainable Energy Technologies, 2008, Singapore, pp. 950-955.

Signed: ………………………………. Date: ……………………………….

Acknowledgements

I would like to thank Dr. Wen L. Soong for his constant guidance and help in directing the research. His supervision has been tremendous in the development of the project. I am also very grateful to Assoc. Prof. Nesimi Ertugrul for the insightful conversations, the advice, and the resources that he provided throughout the research.

My thanks also go to Mehanathan Pathmanathan and all members of the School of Electrical and Electronic Engineering, especially the members of the ‘Power and Control Systems’ group, the administration team, and the members of the Computer Support team, for their friendliness and help. I also would like to thank Dr. Peter Freere, Monash University, for providing the real time wind data, and Dr. David Whaley, for collecting the parameters of commercial wind turbines, which were used in this research.

Last but not least I wish to thank my parents and sister for their constant support and love. A special thanks to my fiancée, Ruijun Wang, for her encouragement and patience during this journey.

Contents

List of Figures

Symbols

ω	turbine speed in rad/s
η	combined efficiency of the generator and the power electronics
ρ	air density or plastic density
λ	tip-speed ratio
γ	blade pitch angle
τ	turbine time constant
σ	standard deviation of a wind speed variation
β	factor of the finite inertia effect on the power reduction
σ^2	variance of a wind speed variation
$\lambda_{(res)}$	resultant tip-speed ratio
$\lambda_{0(act)}$	actual optimal tip-speed ratio
$\lambda_{0(est)}$	estimated optimal tip-speed ratio

ω_{eq}	equivalent frequency of a real wind speed variation
λ_o	optimal tip-speed ratio
τ_o	natural time constant
ΔP	power reduction
ω_{rated}	rated turbine speed in rad/s
ΔT	acceleration torque
Δv	peak variation of wind speed
A	swept area of blades
C_p	power coefficient of wind turbines
$C_{p(res)}$	resultant power coefficient
C_{p0}	maximum power coefficient
$C_{p0(act)}$	actual maximum power coefficient
$C_{p0(est)}$	estimated maximum power coefficient
C_{pmax}	maximum power coefficient
C_t	torque coefficient
J_g	rotor inertia of the generator
J_t	turbine inertia
k	ratio of the optimal turbine speed to the current wind speed
k_0	ratio of the optimal torque to the square of turbine speed
m_R	mass of the rectangular shape blade
m_{rotor}	mass of the rotor blades
m_T	mass of the triangular shape blade
n	turbine speed in rpm
n_{opt}	optimal turbine speed in rpm
$P_{(res)}$	resultant output power

$P_{0(act)}$	actual maximum output power
$P_{0(est)}$	estimated maximum output power
P_J	output power with finite inertia
$P_{J=\infty}$	output power with infinite inertia
$P_{J=0}$	output power with zero inertia
P_m	mechanical output power
P_{out}	output power of the wind turbine system
P_{rated}	power rating
$P_{reduction}$	power reduction
R	radius of the rotor of a wind turbine
T_g	generator torque
T_{opt}	optimal generator torque
T_{opt}^*	reference of the optimal generator torque
T_{rated}	rated torque of a wind turbine
T_t	turbine torque
v	wind speed
v_{CMC}	cube-root-mean-cube of wind speed
v_m	average wind speed
v_{rated}	rated wind speed

Abbreviations

CTC	constant tip-speed ratio control
MPPT	maximum power point tracking
OSP	over-speed protection
OTC	optimal torque control
PR	power reduction
TI	turbulence intensity
TSR	tip-speed ratio

Chapter 1. Introduction

1.1. Wind Energy and Wind Turbines

Wind turbines are increasingly attractive as an environmentally friendly electric power generation system. Fig. 1.1 shows that the world total installed capacity of wind turbines increased annually during the years from 2000 to 2009 [1]. Wind-powered electric generation systems have no by-products and so are sustainable in comparison to conventional electric generation plants. In addition, the operation and maintenance costs of wind generation systems are much lower than for conventional power generation systems.

The format of wind generation systems is flexible and covers large wind turbines (MW) and also small wind turbines (kW). Large wind turbines, commonly seen in wind farms, are mainly grid-connected, that is, they provide electric power to the power grid. The power capability of large wind turbines has been continuously growing over the last twenty years. The increase in the power capability is produced by the increase in the rotor diameter, and hence the increase in the turbine inertia which in turn increases its response time to changes in wind speed. Fig. 1.2 shows the power rating versus the rotor diameter for commercial wind turbines from several major manufacturers (see Appendix A). The power rating increase with rotor diameter can be approximately modelled by the relationship that the power rating P_{rated} is proportional to the square of the rotor diameter D as the rated wind speed of these wind turbines is similar. The smaller wind turbines are utilized in applications such as powering households and can be grid-connected or stand-alone. In a stand-alone system the electric power generated is used locally or stored in batteries.

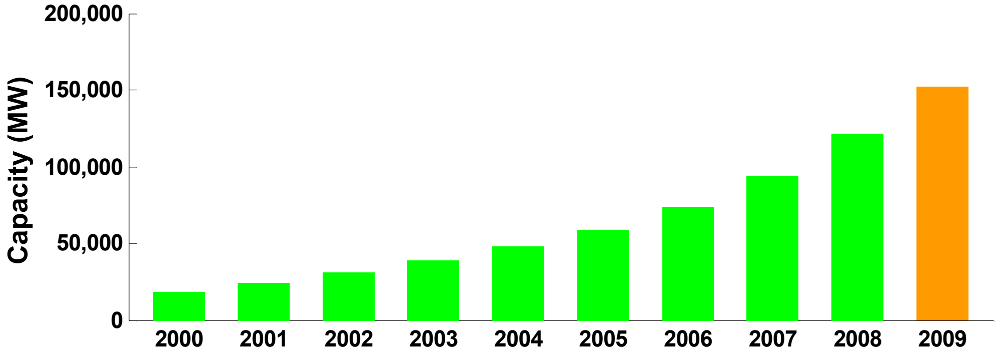

Fig. 1.1 World total installed capacity of wind power

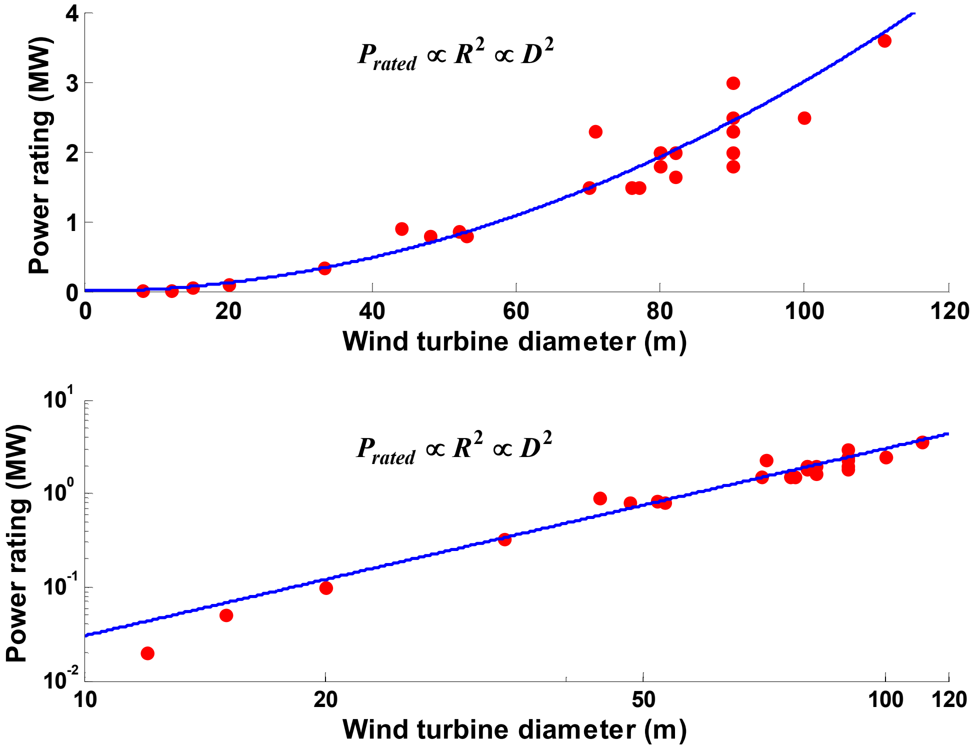

Fig. 1.2 Wind turbine capacity plotted against turbine diameter for a linear scale (upper) and logarithmic scale (lower)

In order to maximize the output power, different control systems are used in wind turbines. Generally the turbine (rotor) characteristics need to be known, which is usually defined by the power coefficient C_p as a function of the tip-speed ratio (TSR). The TSR denotes the ratio of the tip speed of the rotor to the wind speed, and the power coefficient of the turbine represents the "efficiency" by which the rotor converts the available wind power into mechanical power. The maximum value of power coefficient C_{pmax} corresponds to the optimal value of $TSR\ \lambda_o$.

Fig. 1.3 shows wind turbines can be classified into fixed-speed and variable-speed wind turbines. The fixed-speed wind turbines operate under a relatively constant rotational speed and attain the maximum power coefficient at only one wind speed. Comparably, the variable-speed wind turbines are implemented with a maximum power point tracking (MPPT) algorithm which maintains the *TSR* at the optimal value in order to obtain the maximum power coefficient, and hence, the maximum output power over a wide range of wind speeds. Nowadays, variable-speed wind turbines are used more often than fixed-speed wind turbines in commercial applications. In this thesis, the variable-speed horizontal-axis wind turbines are investigated, which include the fixed-pitch design for small wind turbines and the variable-pitch design for large wind turbines.

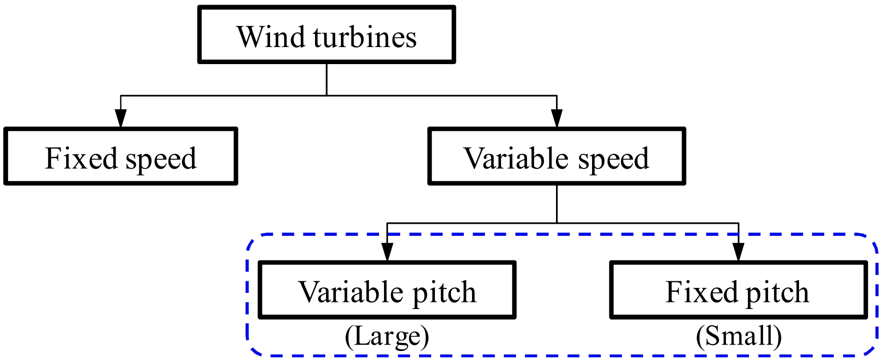

Fig. 1.3. The categories of wind turbines based on their control system

As shown in Table 1.1, both fixed-pitch and variable-pitch wind turbines track the peak power below the rated wind speed, where the variable-speed wind turbine generally operates with a fixed pitch angle [2]. Above the rated wind speed, the output power of both types of wind turbines is limited to the rated output power, and to maintain this variable-pitch wind turbines operate under the pitch control whilst fixed-pitch wind turbines operate with stall control or furling.

Table 1.1 Comparison of the control method for variable-pitch and fixed-pitch wind turbines

	Variable pitch	**Fixed pitch**
Below rated wind speed (MPPT)	- speed control (fixed pitch angle)	- speed control
Above rated wind speed (power limit)	- pitch control	- stall control - furling

For both wind turbines, their inertia restricts their ability to control the rotor speed and hence obtain maximum power coefficient under dynamically changing wind speeds. Moreover, discrepancies in the estimated turbine characteristics can cause non-optimal steady-state tracking. Both of these effects reduce the turbine output power, and will be investigated in this thesis.

1.2. Literature Review

Earlier studies with respect to the dynamic analysis of wind turbines included the following scenarios.

The primary research with respect to the dynamic analysis of wind turbines in earlier studies focused on investigating the mechanical stresses and power quality caused by random wind speed fluctuations and periodic pulsations due to wind shear and tower shadow [3-11]. Wind speed increases with the height above the ground, which is called wind shear. Thus the upward-facing blades will encounter a higher wind speed than the downward-facing blades, causing periodic pulsations of the instantaneous torque and output power. In the case of three-bladed horizontal-axis wind turbines, wind shear causes the rotor to oscillate three times in each rotation, so the pulsations of torque and power are at a frequency which is three times the rotor frequency. There is also an output power pulsation frequency which equals that with which the blades pass in front of the tower, which is commonly called tower shadow. These two types of periodic pulsations are called the *3p* frequency (three periodic pulsations per rotation, see Fig. 1.4) which causes significant harmonics in the output power of large wind turbines [7]. The rotor speed is denoted by *1p* (one periodic pulsation per rotation). Both these effects result in fluctuations of the instantaneous output power, output voltage and frequency.

NOTE:
This figure is included on page 5
of the print copy of the thesis held in
the University of Adelaide Library.

Fig. 1.4 Frequency spectra of the *3p* and *1p* pulsations of two example wind turbine output power characteristics [7]

The effect of wind shear and tower shadow on the periodic output power component was investigated in reference [7]. An analytical model of the dynamic turbine torque including the effects of wind shear and tower shadow was developed in reference [5]. Moreover, in order to reduce the fluctuation of instantaneous output power and voltage, previous research was also made to smooth the instantaneous output power by adding an inductive energy storage circuit in the grid-connected inverter [10].

Earlier studies also investigated the dynamic effect of inertia on the power system stability, which focused on using the kinetic energy stored in the wind turbines to support the frequency control of the power system and thus improve its stability [12-13].

Research was also done in developing control strategies in order to maximize the output power of a wind turbine [14-22]. In these studies, simulations and experiments were constructed to examine their performance under dynamic conditions. For instance, reference [14] developed an optimum control method for an interior permanent magnet synchronous generator for a fixed-pitch wind turbine. It combined optimal torque control (MPPT), maximum efficiency control and maximum torque control. This maximized the power coefficient and hence output power of the wind turbine while minimizing the losses of the generator.

In [14], the principles of optimal torque control (MPPT) was simulated, where the generator torque was controlled along the optimum torque curve according to the current generator speed (see Fig. 1.5 a). In this simulation, a step change in wind speed was given (see Fig. 1.5 b (top)), which resulted in variations of the turbine speed and the generator and turbine torques (see Fig. 1.5 b). These variations correspond to the transient trajectories of the turbine and generator operating points which are highlighted on the torque versus speed characteristic in Fig. 1.5 a. These transient trajectories illustrated the transient behaviour under the optimal torque control. The time constant of the step response was not determined and the turbine characteristic stored in the MPPT controller was assumed to be same as the actual turbine characteristic.

NOTE:
This figure is included on page 6 of the print copy of
the thesis held in the University of Adelaide Library.

(a) Torque versus generator speed (b) Wind speed, generator speed and torque

Fig. 1.5 The dynamic response of the wind turbine when tracking the peak power [14]

The same paper also indicated that inertia delays the response time of the turbine speed. In addition, reference [22] presented a pitch control strategy for variable-speed wind turbines, where the effect of the inertia of wind turbine was reduced by adjusting the pitch rate in order to improve the smoothness of the turbine speed variation and hence instantaneous output power.

Some other studies focused on developing a dynamometer based real-time wind turbine simulator which is able to simulate the mechanical behaviour of a wind turbine, where a DC or AC motor was controlled to output a variable turbine torque to drive the generator [23-26]. This was used to test the performance of the generator control algorithms under "hardware simulation". Static and dynamic characteristics were commonly provided in order to verify the accuracy of the simulator. For instance, reference [23] simulated the step responses of a wind turbine under MPPT control. The variation of turbine speed with a constant load under a step change of wind speed is shown in Fig. 1.6 a, and with a step change in load under a constant wind speed in Fig. 1.6 b.

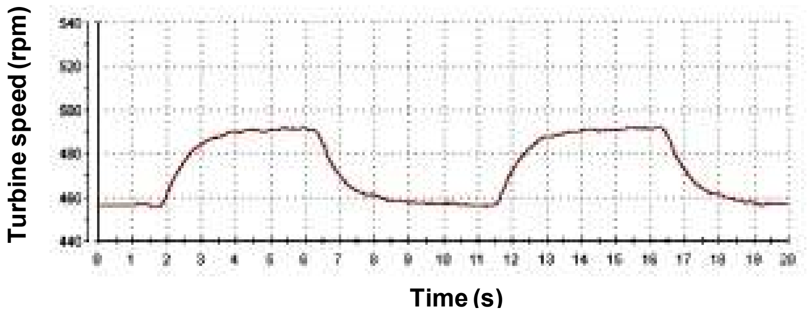

(a) Wind turbine behaviour for wind speed steps

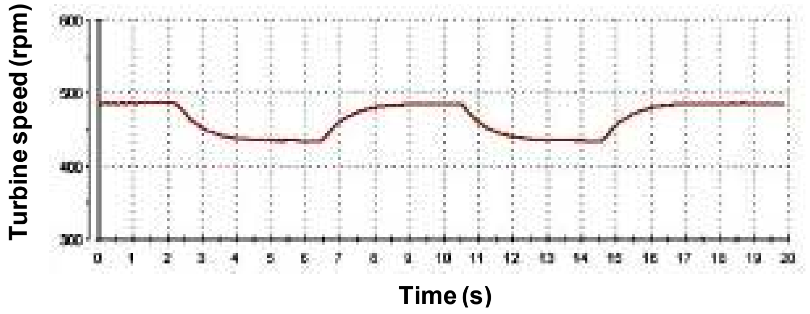

(b) Wind turbine behaviour for load torque steps

Fig. 1.6 The dynamic response of a wind turbine under the conditions of (a) step change of wind speed, (b) step change of load torque [23]

It should be noted that the estimated turbine characteristics were assumed to be correct in all of the above studies. However, the discrepancy between the measured and estimated C_p versus TSR curves has been indicated in the earlier studies, such as reference [27] which presented the detailed system modelling for a grid-connected 5kW fixed-pitch wind turbine under MPPT control. In this paper, the estimated and measured C_p curves were compared.

As accurate optimal parameters are hard to determine, reference [40] proposed an improved control scheme based on the standard optimal torque control with inaccurate optimal parameters and demonstrated a 0.5% to 1% increase in output power by simulation.

Another important source of power loss is due to yaw errors, that is, the turbine not being controlled to face directly into the wind direction. This effect is analysed in [40]. In this thesis, zero yaw error is assumed when the wind turbine tracking the maximum power point.

The above literature reviews has identified two research gaps in the operation of wind turbines with MPPT:

- The effect of inertia on the average output power under dynamically varying wind speed and,
- The effect of wind turbine model parameter errors on the steady-state output power.

1.3. Research Contributions

In the first part of the study, the effect of inertia on the dynamic performance of wind turbines under MPPT will be investigated. The turbine time constant will be introduced to denote the transient response time of a wind turbine system with inertia under maximum power point tracking control. An analytical equation for the turbine time constant is derived for small step changes of wind speed, which shows the turbine time constant is inversely proportional to wind speed. The new concept of the natural time-constant τ_o is introduced as the time constant at rated wind speed. The natural time-constant varies roughly from 1s (small wind turbines) to 10s (large wind turbines). It is a function of the inertia and the rated turbine speed. It can be predicted by its approximate relationship with power rating as $\tau_o \propto P_{\text{rated}}^{0.3}$. Moreover, analytical equations are derived for the power reduction with both infinite inertia and finite inertia by taking into account of the wind characteristics and also the turbine characteristics using the turbine time constant. A dynamic simulation model of a wind turbine system consisting of the turbine characteristics, an idealised generator model and the MPPT control algorithm is built up using the PSIM$^{®}$ package to verify the analytical results.

In the second part of the study, the effects of parameter errors on the steady-state output power of a wind turbine are investigated under MPPT control. Two different control strategies of MPPT are analysed in this part. Finally, the power reduction versus the error in the estimated maximum power coefficient and the optimal tip-speed ratio with an example power coefficient curve was determined.

1.4. Thesis Layout

CHAPTER 2: This chapter introduces the dynamic model of a wind turbine system in detail, and provides the definition of the turbine time-constant.

CHAPTER 3: It provides the analysis of time constant with a small step change in wind speed, and the numerical results generated by the dynamic model of a wind turbine system are compared with the analytical results.

CHAPTER 4: In this chapter, the power reduction due to the inertia under dynamic wind conditions is defined and analysed under the extreme condition where infinite inertia of the wind turbine is assumed. The analytical result generated is compared with the numerical result which is obtained from the dynamic model.

CHAPTER 5: The effects of finite inertia on the power reduction are analysed. The analytical equation including the effect of finite inertia is compared with the numerical results from the dynamic model.

CHAPTER 6: The chapter provides the analysis of the power reduction due to the inertia from the simulation using real wind data recorded by an anemometer. The analytical equation of the power reduction has been used to compare with the simulation results.

CHAPTER 7: Some limited experimental measurements of the turbine time constant are provided in this chapter.

CHAPTER 8: A steady-state study of the turbine parameter sensitivity of MPPT is presented. This provides a physical understanding of the power reduction caused by the discrepancy of the estimated turbine characteristics for constant TSR control and optimal torque control.

CHAPTER 9: The conclusions of the dynamic study of the inertia effects on MPPT and the steady-state study of the parameter sensitivity on MPPT are given in the final chapter. The chapter also includes suggestions for future studies.

Chapter 2. Dynamic Model of a Wind Turbine System

2.1. Introduction

In this chapter, the detailed description of the dynamic model of a wind turbine system under the MPPT control is provided. This wind turbine system model will be utilized to simulate the variations of the system variables and generate the numerical power reduction in this research.

A general diagram of a wind generation system is given in Fig. 2.1 which consists of the turbine, the generator, the power electronics and generator controller with the controls for MPPT.

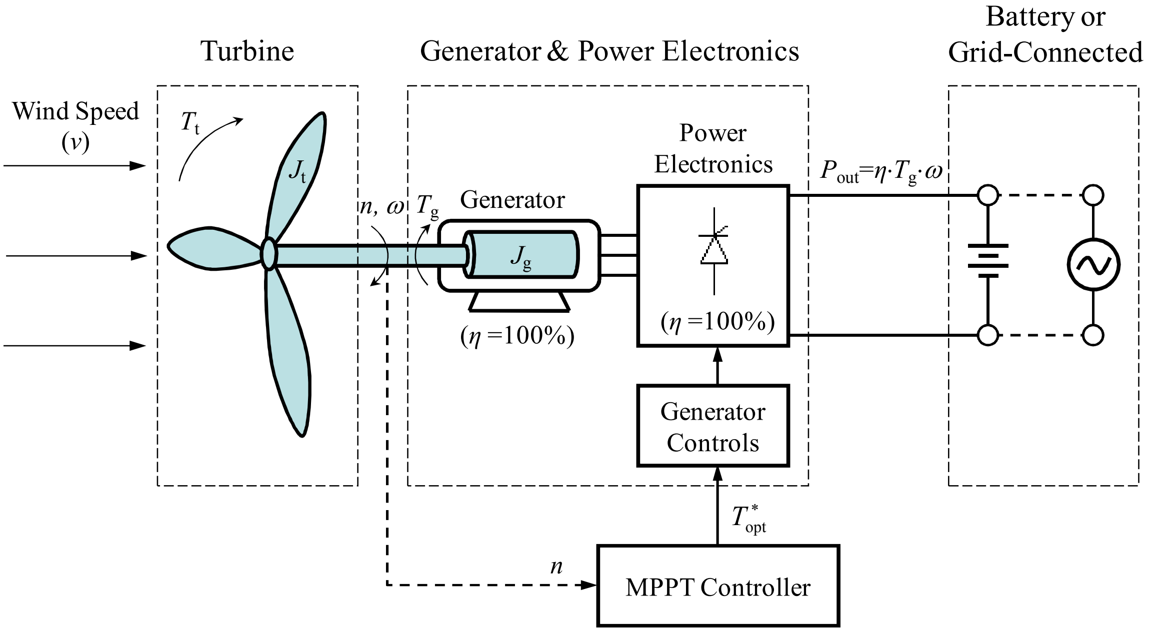

Fig. 2.1 The overview of a direct-driven wind turbine system

Where, v is the wind speed; J_t is the turbine inertia; T_t is the turbine torque; J_g is the rotor inertia of the generator; T_g is the generator torque; n is turbine speed in rpm, ω is turbine speed in rad/s; η is the combined efficiency of the generator and the power electronics; P_{out} is the output power of the wind turbine system; and T_{opt}^* is the reference for optimal generator torque.

The previous studies, which focus on the implementation of the power electronics topologies or the control strategies for a wind generation system, involve detailed modellings of the power electronics modulation and the control algorithms in order to examine the control system's performance [14-20]. The simulation studies in these detailed models commonly required longer execution time to simulate few seconds or minutes of wind speed data. To study the inertia effects on the dynamic power reduction in this thesis however, hours of wind speed data are proposed to be simulated within a few seconds. Therefore, a simplified model of the wind turbine system is proposed in this thesis, which consists of the turbine, the generator and MPPT control only. The detailed operation of the power electronics and generator controls is neglected by assuming that the generator precisely follows the commands provided by the MPPT controller. In addition, it is further assumed that both the generator and the power electronics have no losses. As it was aimed, the proposed wind turbine system model in this thesis is able to simulate hours of wind speed data in seconds.

In the dynamic study of inertia effects on the output power reduction of a wind turbine under MPPT control, it is assumed that the actual power coefficient curve (C_p curve) of the wind turbine is identical to the estimated C_p curve which is used in MPPT (see Fig. 2.2). Due to the existence of inertia, the acceleration and the deceleration of a wind turbine are delayed, and the wind turbine does not operate at its optimal output power point during the wind speed changes. It will be shown that this results in an output power reduction. Specifically, when wind speed varies rapidly, the power reduction is significant. In Chapter 4 and 5, the analytical equations of the power reduction are derived in order to give a physical understanding of the effects of inertia on the output power reduction under MPPT control, and a wind turbine system model based on the diagram in Fig. 2.2 is developed using PSIM® to generate the numerical results which are then compared with those obtained from the analytical equations.

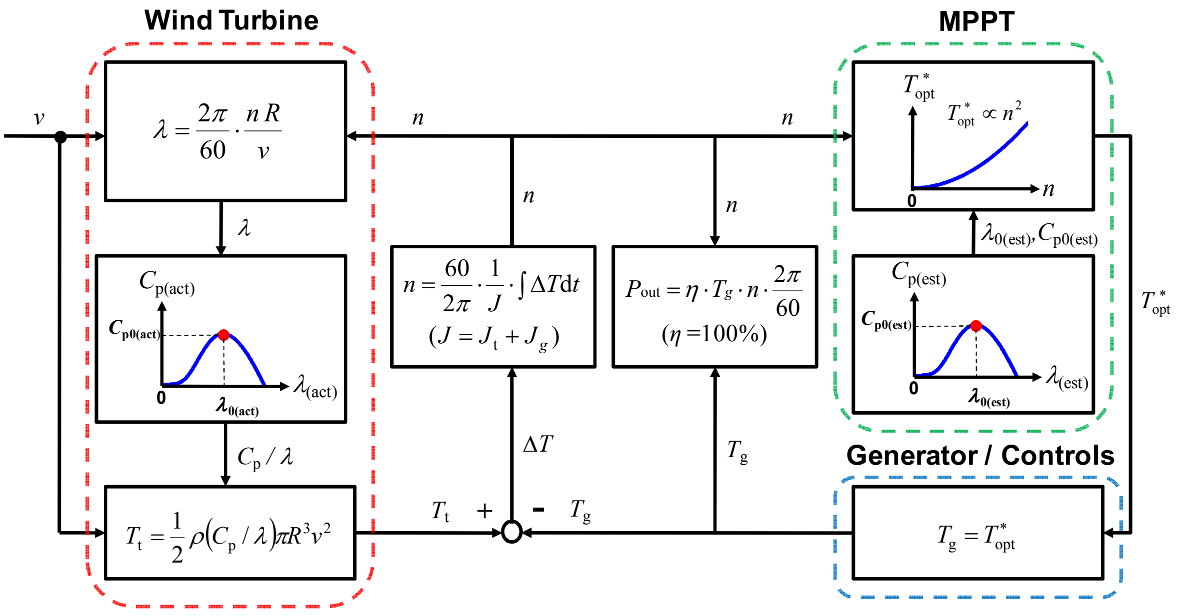

Fig. 2.2 The diagram of the dynamic model of a wind turbine system for the analysis of inertia effects on the output power reduction under the MPPT control

2.2. Wind Modelling

The wind is characterised by the wind direction and the wind speed. It this thesis, the wind direction is assumed to face the rotor plane of the wind turbine, and wind speed is only treated in the study. In practice, wind turbines operate with various turbulences from the wind speed. Typical wind behaviours include gusting, ramp and random variations [3] which are commonly considered in the study of the dynamic performance of large wind turbines. In the thesis, the square variation is used to model the wind gusting, the sinusoidal and the triangular variations are used to model the wind ramps, and the real wind speed data is used to model the random as shown in Fig. 2.3.

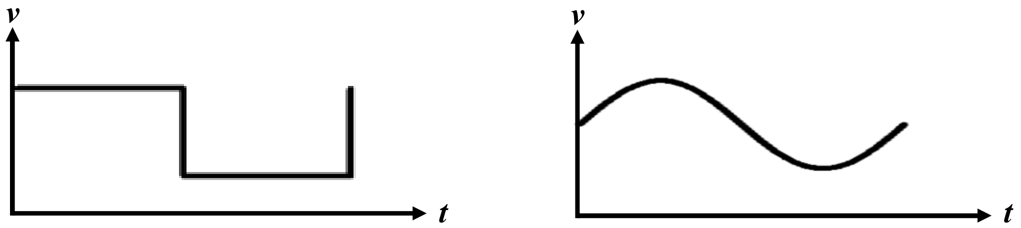

(a) Square variation (gusting) **(b) Sinusoidal variation (ramp 1)**

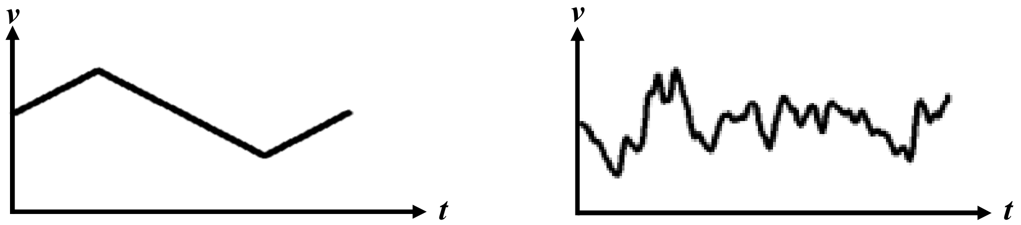

(c) Triangular variation (ramp 2) **(d) Real wind speed (random)**

Fig. 2.3 The models for the wind speed variations: (a) square wind speed variation; (b) sinusoidal wind speed variation; (c) triangular wind speed variation; (d) real wind speed.

2.3. Wind Turbine Modelling

The modelling of wind turbines is based on the performance equation. The main terms of a turbine's characteristics are its power coefficient (C_p) and tip-speed ratio (λ or *TSR*). At a given wind speed v, the mechanical power P_m converted from the kinetic power of the wind by a wind turbine is given as,

$$P_m = \frac{1}{2}\rho C_p \pi R^2 v^3 \tag{2.1}$$

where, C_p is the power coefficient and is a measure of the efficiency at which the wind turbine converts the aerodynamic power in the wind into mechanical power. Note that, the mechanical power P_m equals to the output power P_{out} as both the generator and the power electronics are assumed to have no losses. The turbine torque as a function of turbine shaft rotational speed n can be obtained as,

$$T_{\mathrm{t}} = \frac{1}{2}\rho C_{\mathrm{t}} \pi R^3 v^2 = \frac{1}{2}\rho (C_{\mathrm{p}}/\lambda) \pi R^3 v^2 \tag{2.2}$$

where, ρ is the air density; R is the radius of the turbine blades; C_{t} is torque coefficient; and λ is given as,

$$\lambda = \frac{\omega R}{v} = \frac{2\pi n R}{60 v} \tag{2.3}$$

where, ωR is the linear tip speed of the turbine blades.

The power coefficient C_{p} of a wind turbine is dependent on the blade pitch angle γ, the tip-speed ratio λ, and the number and design of the rotor blades. The pitch angle γ is defined in [2] as the angle between the rotor plane and the chord of blade as shown in Fig. 2.4.

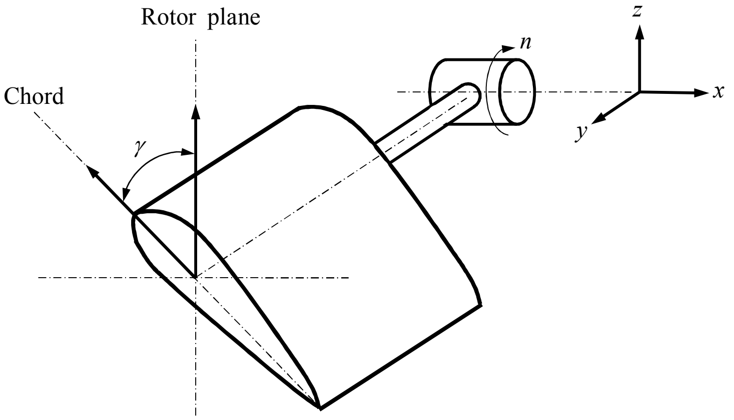

Fig. 2.4 The blade pitch angle of a wind turbine

For a variable-pitch wind turbine, the pitch angle γ is adjustable and the pitch control is usually used in order to improve the performance of operation.

According to [28], a general model for the C_p-TSR curve is,

$$C_{\mathrm{p}} = c_1\left(c_2 - c_3\gamma - c_4\gamma^x - c_5\right)e^{-c_6} \tag{2.4}$$

where the constants $c_1 - c_6$ are determined by the type of wind turbine. In the case of the MOD 2 turbine (a two-bladed wind turbine), the constants are given as c_1=0.5, c_2=116/λ_i, c_3=0.4, c_4=0, c_5=5, c_6=21/λ_i, and $\frac{1}{\lambda_i} = \frac{1}{\lambda + 0.08\gamma} - \frac{0.035}{\gamma^3 + 1}$.

Another C_p model is provided in the Matlab Help profile [29] for a variable-pitch wind turbine (the specific model can not found in the reference). This is given by,

$$C_p = c_1 (c_2 - c_3\,\gamma - c_4) e^{-c_5} + c_6 \lambda \tag{2.5}$$

where, the constants are given as c_1=0.5176, c_2=116/λ_i, c_3=0.4, c_4=5, c_5=21/λ_i, c_6=0.0068, and $\frac{1}{\lambda_i} = \frac{1}{\lambda + 0.08\gamma} - \frac{0.035}{\gamma^3 + 1}$.

The two C_p models in [29] and [28] are compared in Fig. 2.5. It shows the two models are similar in profile but slightly different in the peak values. The peak trajectories highlighted generally decline as the pitch angle γ increases. The largest peak values of a C_p model commonly appears with a small blade pitch angle, and ideally the highest power coefficient C_{pmax} is at zero pitch angle.

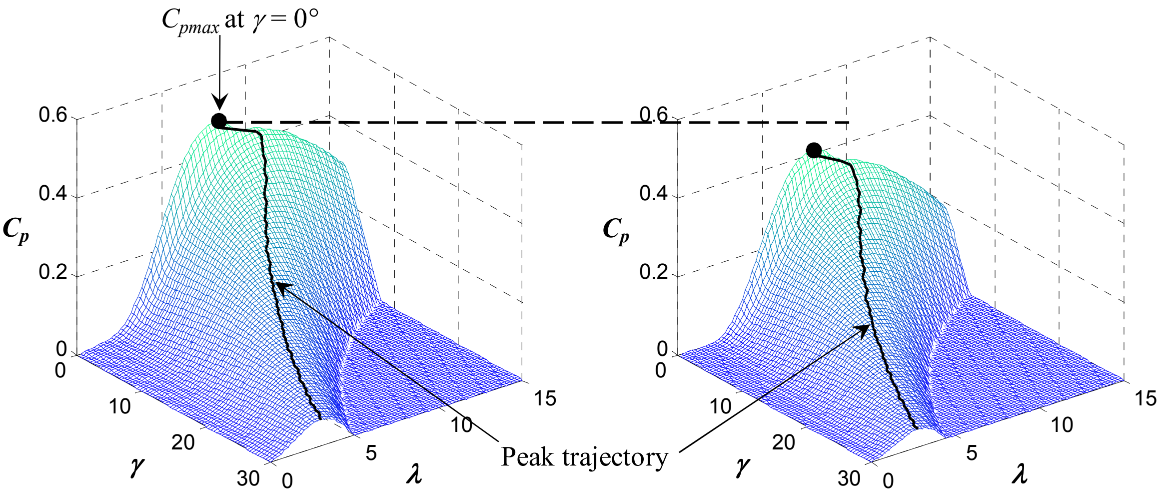

(a) The C_p model in [29] (b) The C_p model in [28]

Fig. 2.5 Example power coefficient curves for a variable-pitch wind turbine in [28] and [29]

It is assumed that a variable-pitch wind turbine operates at a small pitch angle most of the time in order to obtain a high value of C_p. Therefore, in this thesis, the ideal zero-degree pitch angle for a variable-pitch wind turbine is assumed when it operates under pitch control.

For a fixed-pitch wind turbine, the pitch angle γ is manufactured with a fixed value which is commonly small in order to achieve a large peak value of C_p. Therefore, the C_p (λ) curve of a fixed-pitch wind turbine can be seen as the same as a variable-pitch wind turbine at a certain optimised pitch angle. The zero-degree pitch angle wind turbine is an idealised case with the highest maximum C_p (see Fig. 2.5) but may be harder to start at low wind speeds due to the low value of torque coefficient C_t ($C_t = C_p/\lambda$) at a low TSR. The C_p curves from the references [29] and [28] with the zero-degree pitch angle are compared in Fig. 2.6, which displays the difference in the peak value whilst the optimal tip-speed ratio λ_o corresponding to the peaks and the shape of the two C_p curves are similar. The thesis uses the C_p model given in [29] with the zero degree of pitch angle in Fig. 2.6, where the maximum power coefficient C_{pmax} is 0.48 which corresponds to an optimal *TSR* of 8.1. Note that this C_p (λ) model is only valid for values of *TSR* between 0 and 13.4 (the no-load value).

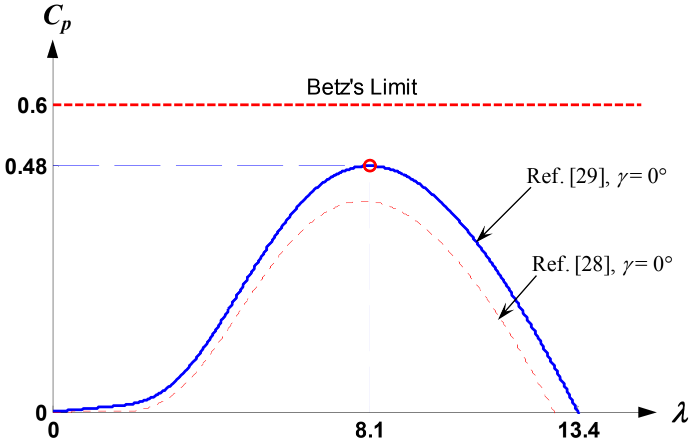

Fig. 2.6 Power coefficient curves with a fixed pitch angle

As shown in Fig. 2.6, the two curves have a similar profile. The shape of the C_p curve is an important factor in determining the loss of power under dynamic wind conditions. On the other hand, the peak value of the C_p is not critical in the estimation of the average power reduction for a wind turbine operating under the MPPT control. This is due to the fact that the power reduction $P_{reduction}$ is defined to be equal the difference between the output power with zero inertia $P_{J=0}$ and the output power with inertia P_J

divided by the output power with zero inertia. This is equal to the difference between the C_p with zero inertia $C_{p(J=0)}$ and the C_p with inertia $C_{p(J)}$ divided by the C_p with zero inertia as shown in Equation (2.6). In the calculation, the error on the peak value of the C_p curves is cancelled.

$$P_{\text{reduction}} = \frac{P_{J=0} - P_J}{P_{J=0}} = \frac{C_{\text{p}(J=0)} - C_{\text{p}(J)}}{C_{\text{p}(J=0)}} \tag{2.6}$$

A C_p curve for a three-bladed wind turbine with a blade pitch angle of 0° is provided by a turbine manufacturer in reference [21] as shown in Fig. 2.7. Comparing this C_p curve with Fig. 2.6, the maximum power coefficient C_{pmax} is similar whilst the optimal tip-speed ratio λ_o is somewhat smaller. The profile of the C_p curve in Fig. 2.7 is similar to Fig. 2.6 except at low values of TSR.

NOTE:
This figure is included on page 18 of the print copy of the thesis held in the University of Adelaide Library.

Fig. 2.7 The C_p curve for a 3-bladed wind turbine provided by the turbine manufacturer in reference [21] with $\gamma = 0°$.

It should be noted that the $C_p(\lambda)$ curve is assumed as constant with respect to wind speed in this thesis. This basically means that the blades are assumed to be rigid. The stall delay effects [41] [42] on the $C_p(\lambda)$ curve are not included in this study.

2.4. Principle of Maximum Power Point Tracking

In order to produce the maximum output power at a given wind speed, maximum power point tracking (MPPT) is used to control the wind turbine generator to maintain the tip speed ratio at the optimal value. It should be noted that since the rated wind speed of a wind turbine generally varies around 12m/s-15m/s, a wind turbine only tracks the maximum power point below the rated wind speed. When the wind speed rises above the rated wind speed, the over-speed protection control limits the output power of the wind turbine. Fig. 2.8 shows an example of the turbine output power versus turbine speed characteristics and the maximum power operating points for wind speeds ranging from 5 m/s to 12 m/s. This is based on the parameters of a 400 W wind turbine (see Table 3.1 in Chapter 3).

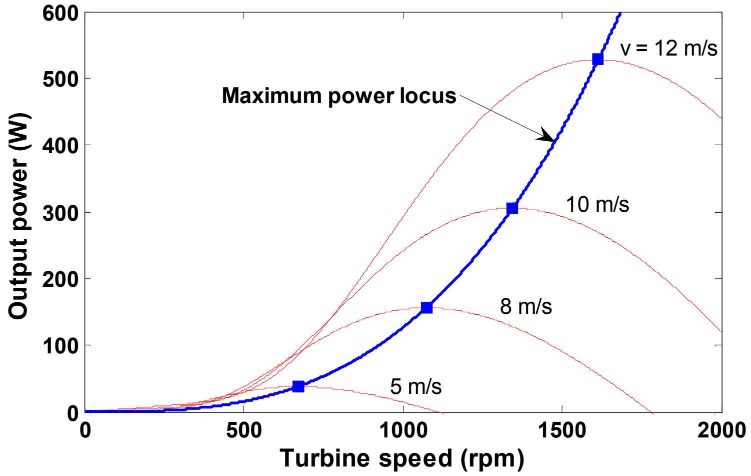

Fig. 2.8 An example maximum power locus based on the output power versus turbine speed for wind speeds from 5 m/s to 12 m/s.

The maximum power locus in Fig. 2.8 can be analysed by using the maximum output power as a function of turbine speed which is obtained by combining Equations (2.3) and (2.1),

$$P_{\max} = \frac{1}{2} \rho C_{\text{pmax}} \pi R^2 \left(\frac{2\pi R}{60\lambda_0} \right)^3 \cdot n^3 \tag{2.7}$$

In order to control a wind turbine to produce maximum output power, different control strategies are investigated in the literature, including optimal torque control, current control, neural network control, wind speed tracking control, fuzzy-logic control and hill-climbing control [14-20]. Amongst these control strategies, optimal torque control, current control, wind speed tracking control, and fuzzy-logic control are based on the knowledge of the wind turbine characteristics, while this is not needed for hill-climbing control and neural network control.

The choice of MPPT algorithm affects the performance under dynamic conditions. The optimal torque control scheme was chosen as it is commonly used in simulations and is one of the simplest to analyse. It should be noted that when implemented in a real wind turbine, significant modifications to this algorithm are often used to improve performance under step changes in wind speed. For instance, if a step increase in wind speed is detected it is often desirable in practice to drop the generator torque to zero to give the wind turbine a chance to accelerate to its optimal speed. Analysis of these modifications is beyond the scope of this work and only the basic optimal torque scheme will be analysed.

In this thesis, the optimal torque control strategy is chosen to construct the MPPT control system, where the information of the turbine optimal torque versus the turbine speed characteristics is needed. The 400 W wind turbine torque versus turbine speed characteristics for wind speeds from 5 m/s to 12 m/s is shown in Fig. 2.9.

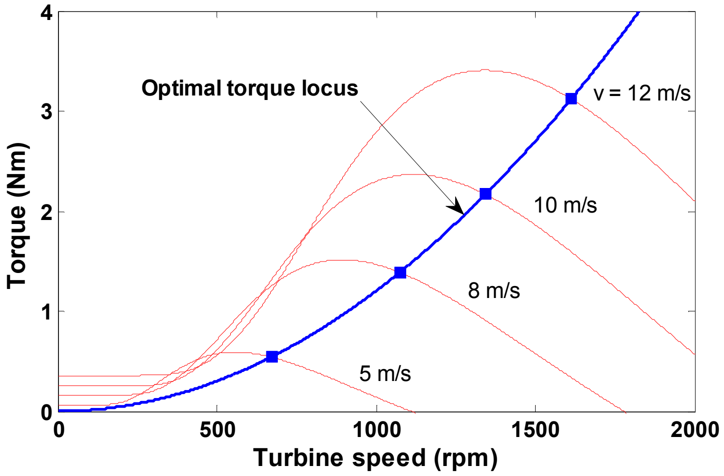

Fig. 2.9 An example turbine torque versus turbine speed characteristics for wind speeds from 5 m/s to 12 m/s.

The optimal torque locus in Fig. 2.9 can be analysed by using the optimal torque as a function of turbine speed which is obtained by combining Equations (2.2) and (2.1),

$$T_{\mathrm{opt}} = \frac{1}{2}\rho\,(C_{\mathrm{pmax}}/\lambda_0)\,\pi R^3 \left(\frac{2\pi R}{60\,\lambda_0}\right)^2 \cdot n^2 \tag{2.8}$$

where, the optimal torque is proportional to the square of the turbine speed. In optimal torque control, the generator torque is controlled to follow the optimal torque reference which is equal to T_{opt} in Equation (2.8).

The optimal torque reference is generated by the MPPT controller for a given turbine speed through the turbine optimal torque versus speed characteristics stored in the MPPT controller as shown in Fig. 2.10. In this approach, it is assumed that the generator torque is controlled to be exactly the same as the optimal torque reference in order to simplify the wind turbine system model.

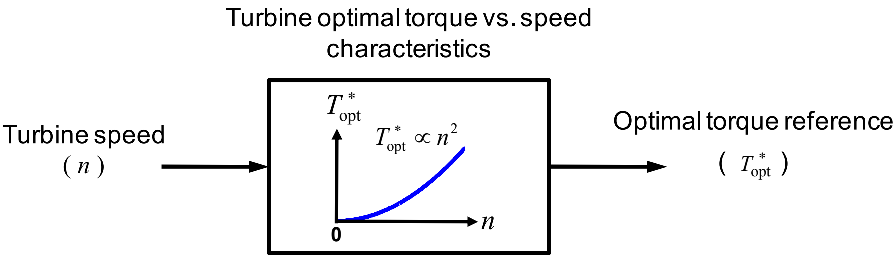

Fig. 2.10 The block diagram of the optimal torque control strategy

When MPPT control is implemented in a wind turbine system, the optimal turbine speed of the wind turbine is the value of turbine speed corresponding to the maximum power point for a given wind speed. This is linearly proportional to the wind speed as shown in Fig. 2.11 for the 400 W wind turbine.

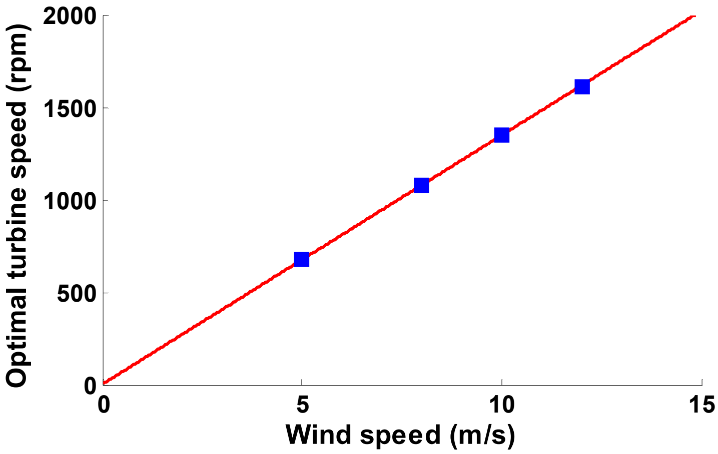

Fig. 2.11 The optimal turbine speed versus wind speed for the turbine characteristics shown in Fig. 2.8 and Fig. 2.9.

In Fig. 2.11, the ratio of the optimal turbine speed n_{opt} to the current wind speed v is defined as the constant k,

$$k = \frac{n_{\text{opt}}}{v} = \frac{60}{2\pi} \cdot \frac{\lambda_o}{R} \tag{2.9}$$

where, λ_o is the optimal TSR. Based on Equations (2.1) and (2.9), the relationship between the output power and the optimal turbine speed is obtained as,

$$P_{\max} \propto v^3 \propto n_{\text{opt}}^3 \tag{2.10}$$

2.5. Example Simulation Using the Dynamic Model of a Wind Turbine System

In Fig. 2.12, a square-wave variation of wind speed is shown with an average value of 8 m/s and an amplitude of 2 m/s. The simulation study has been done in the wind turbine system model using the parameters of the sample 400 W wind turbine. The variations of the generator and turbine torque, the turbine speed and the output power is shown in Fig. 2.12 with and without the effect of inertia.

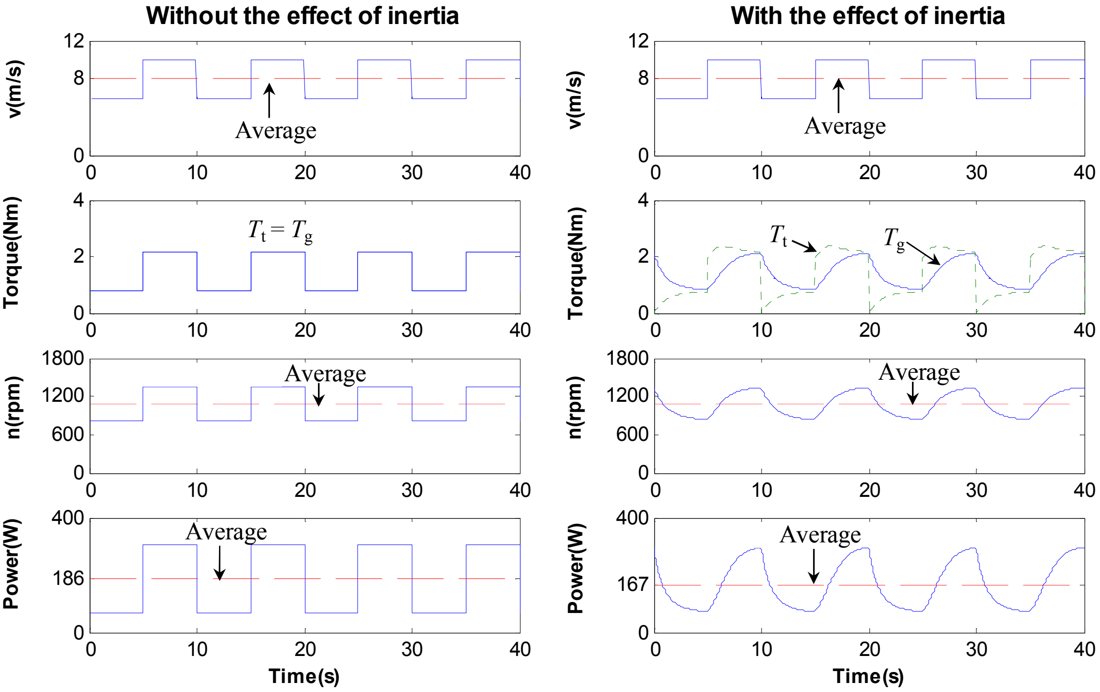

Fig. 2.12 The variations of the system variables with and without the effects of inertia under the MPPT control

In Fig. 2.12, it can be seen that the variations of the generator torque, the turbine speed and the output power generally become smoother with the effect of inertia. Moreover, the average turbine speed without the effect of inertia is 1076 rpm, which is similar to the average turbine speed with the effect of inertia. Furthermore, 1076 rpm is also the optimal turbine speed corresponding to the wind speed of 8 m/s. In addition, with the effect of inertia, the average power is reduced to 167 W which was 186 W without the inertia effect.

2.6. Summary

In this chapter, the detailed description of the dynamic model of a wind turbine system is provided. The proposed C_p curve model is given and compared with the C_p curve from a manufacturer, which displays similar characteristics. The principle of maximum power point tracking is also explained. The optimal torque control is proposed to be used in the dynamic model of the wind turbine system.

For the purpose of investigating the dynamic power reduction due to inertia, the dynamic wind turbine system model is used to construct the numerical simulation model of dynamic power reduction (see Fig. 2.13 (a)). The numerical results of the dynamic power reduction generated from this numerical simulation model are accurate but still slow if the wind data set is large, such as days of wind data.

In the following chapters, an analytical model of dynamic power reduction (see Fig. 2.13 (b)) is developed based on the derived analytical equations. The analytical model gives a physical understanding of the correlation between the wind and turbine characteristics and the dynamic power reduction of wind turbines. It can also rapidly estimate the power reduction due to the effects of inertia under varying wind conditions. The results obtained from the numerical simulation model of the dynamic power reduction are used to verify the analytical results obtained from the analytical model of dynamic power reduction.

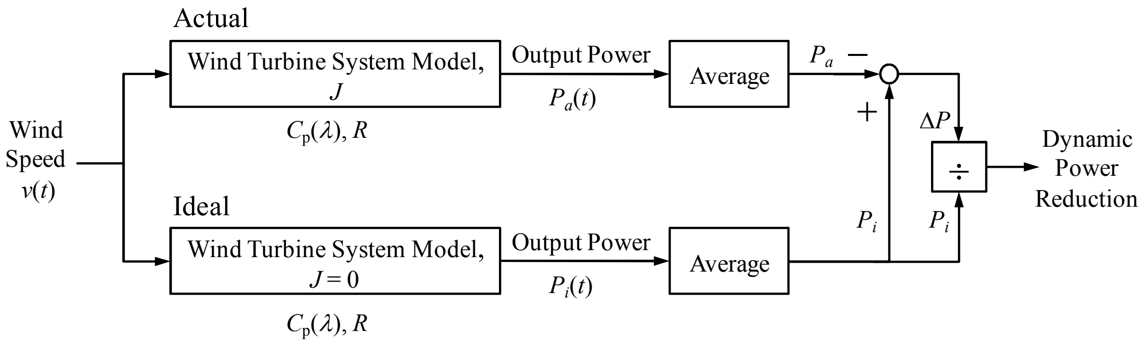

(a) Numerical simulation model

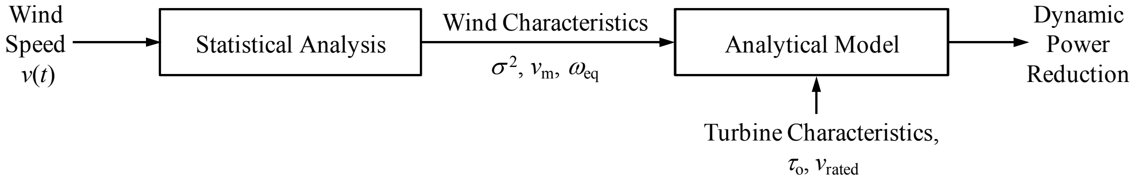

(b) Analytical model

Fig. 2.13 The numerical simulation model (a) and the analytical model (b) of the dynamic power reduction of a wind turbine

Chapter 3. Turbine Time Constant

3.1. Introduction

In this Chapter, a small step change in wind speed is given to the wind turbine system model which then demonstrates performance like a first-order system. The turbine response time is investigated as the turbine time-constant under the different wind speeds. The analytical equation of the turbine time-constant is derived for a wind turbine under a small step change of the wind speed input. In addition, the numerical turbine time-constants obtained by running the wind turbine system model in PSIM® at different wind speed levels are then compared with the analytical results. Furthermore, the natural time-constant is defined as the turbine time-constant at the rated wind speed of the wind turbine. Finally, the trend of the natural time-constant versus power rating is predicted for commercial wind turbines.

3.2. Analytical Equation of the Small-Signal Time Constant

In order to evaluate the inertia effect on the dynamic response of a wind turbine, the concept of turbine time constant τ is introduced to denote the transient response time of a wind turbine. The turbine time constant τ is defined as the interval time by which the shaft speed reaches 63.2% of the change between the two steady-state speeds. In this section, the analysis of the turbine time constant τ as a function of wind speed is performed assuming small wind speed step changes.

A step change is given in wind speed from v_1 to v_2 to a wind turbine under MPPT as shown in Fig. 3.1, which results in the variation of optimal turbine speed in the steady-state proportional to the wind speed, $n_{\mathrm{opt}} \propto v$. Due to the effect of inertia, there is a transient process with time constant τ between the two optimal turbine speed at the two steady-state operating points, which acts like in a first-order system. The turbine torque equals the generator torque at the optimal values in the steady-state whilst they are different during the transient state. In Fig. 3.1, the C_{p} of the wind turbine has the maximum value C_{pmax} under the two different steady-state operating points, where the turbine speed, the generator torque and the turbine torque have their optimal values. In comparison, during the transient operation caused by the wind speed change, C_{p} becomes lower than the maximum value C_{pmax}. Therefore, a wind turbine under MPPT can only generate the optimal output power with the maximum power coefficient in steady-state operation, and during the transient operation power is lost due to the lower value of C_{p}.

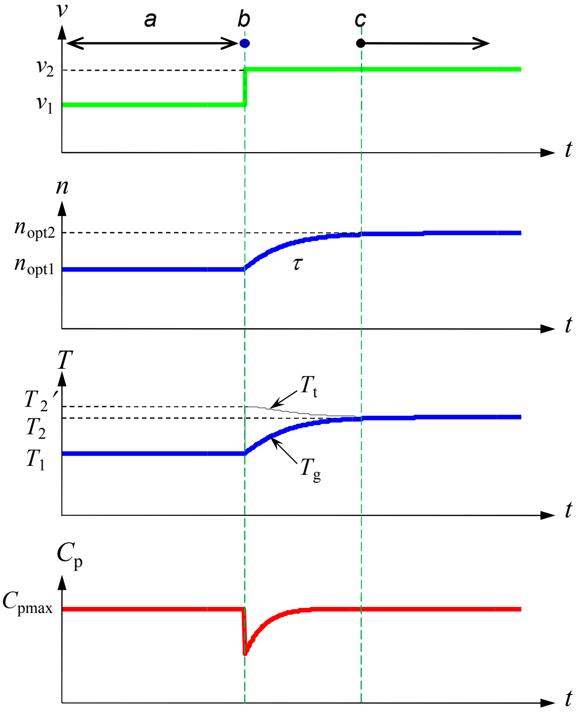

Fig. 3.1 The example variations of the system variables with finite inertia for a step change of wind speed under MPPT

In this thesis, small wind speed variations are assumed so that large changes in C_p are avoided and so the wind turbine does not stall when the wind speed increases.

Moreover, for larger wind speed variations where the minimum wind speed is low ($v < 1$m/s), the instantaneous TSR can be much greater than the no-load value (13.4) where the $C_p(\lambda)$ curve is no longer valid (see Fig. 2.6). However, this does not affect the results significantly as the power which is close to zero in this situation. This is because the turbine power is proportional to the cube of wind speed, $P \propto v^3$.

As it can be seen in Fig. 3.1, when MPPT is utilized, the turbine torque equals the generator torque at the optimal value under the steady-state operation, while the turbine speed is at its optimal value. Therefore, the tip-speed ratio in the steady-state has its optimal value λ_o which corresponds to the maximum output power and can be calculated for two different wind speeds of v_1 and v_2,

$$\frac{\omega_1 \cdot R}{v_1} = \frac{\omega_2 \cdot R}{v_2} = \lambda_o \tag{3.1}$$

The two steady-state operating points a and c in Fig. 3.1 correspond to the same point (the peak) in the C_p versus TSR characteristic in Fig. 3.2. However, they represent different points in the turbine torque versus speed curves in Fig. 3.3. At Point a, the turbine torque T_t equals the generator torque T_g at the optimal value T_1 under the wind speed v_1, which corresponds to the steady-state operation point under wind speed v_1.

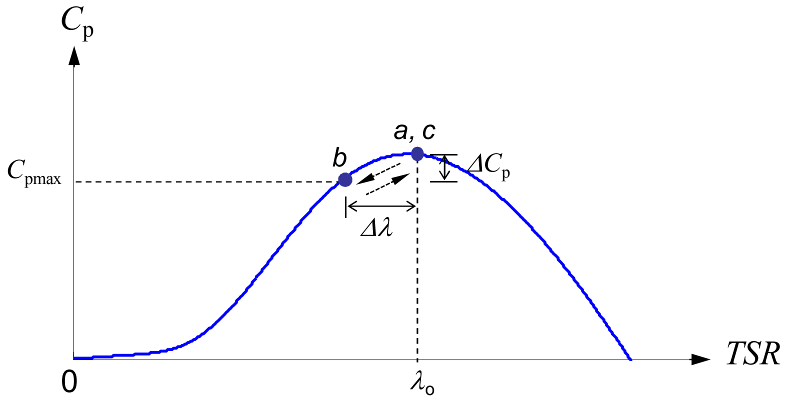

Fig. 3.2 The C_p versus TSR characteristic

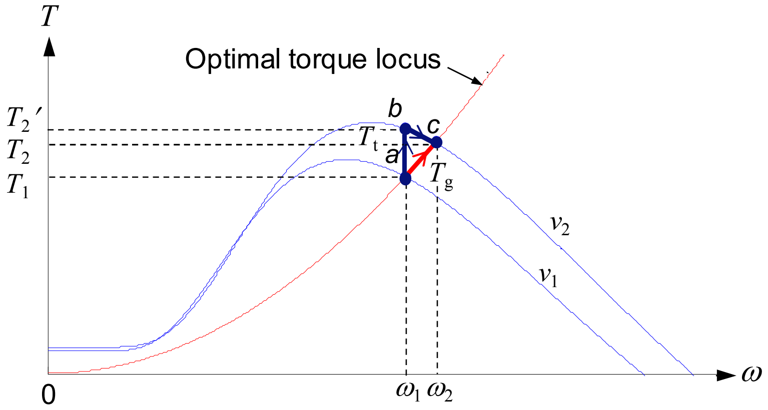

Fig. 3.3 The turbine torque versus turbine speed characteristics for two different wind speeds with the optimal torque tracking

Using Fig. 3.2 and Fig. 3.3, the transient process for the turbine torque can be defined by two intermediate stages. In the first stage, the operating point moves from Point *a* to Point *b* as the wind speed instantaneously changes from v_1 to v_2 (Fig. 3.1), and the generator torque T_g is constant at the optimal value T_1 while the turbine torque T_t increases from T_1 to T_2' immediately. The turbine torque T_2' is larger than the generator torque T_1 so the wind turbine starts to accelerate. During the second stage of the transient progress (from Point *b* to Point *c*), the generator torque increases from T_1 to T_2 as the turbine speed increases from ω_1 to ω_2 while the turbine torque decreases from T_2' to T_2. At Point *c*, the turbine torque equals the generator torque at the optimal value T_2 under the wind speed v_2. The values of T_1 and T_2' are given by,

$$T_1 = \frac{1}{2} \cdot \left(\frac{C_{\text{pmax}}}{\lambda_o} \right) \cdot \rho \cdot A \cdot R \cdot v_1^2 \tag{3.2}$$

and

$$T_2' = \frac{1}{2} \cdot \left(\frac{C_{\text{pmax}} - \Delta C_p}{\lambda_o - \Delta \lambda} \right) \cdot \rho \cdot A \cdot R \cdot v_2^2 \tag{3.3}$$

where, $A=\pi R^2$ is the swept area of the blades. The power coefficient changes from C_{pmax} to C_{pmax}-ΔC_p when the tip speed ratio changes from λ_o at Point *a* to λ_o-$\Delta\lambda$ at Point *b*. Since the wind speed change is assumed to be small, $\Delta\lambda$ is small and if the peak of the C_p versus

λ curve is fairly broad (see Fig. 3.2) then $\Delta C_p \approx 0$ in Equation (3.3) so $T_2' \approx T_2$ is obtained. The denominator $\lambda_o - \Delta\lambda$ in Equation (3.3) can be given by,

$$\lambda_o - \Delta\lambda = \frac{\omega_1 \cdot R}{v_2} \tag{3.4}$$

The acceleration torque ΔT produced by the step change in wind speed is given by,

$$\Delta T = T_2 - T_1 \tag{3.5}$$

The region surrounded by Points *a*, *b* and *c* in Fig. 3.3 can be approximated as a triangular shape. In this triangular region, the acceleration torque is proportional to the turbine speed change, $\Delta T \propto \omega_2 - \omega_1$. Therefore, the wind turbine system model with a small-signal wind speed input can be seen as a first-order linear system, where the turbine time constant can be obtained as,

$$\tau = \frac{\omega_2 - \omega_1}{\Delta T / J} \tag{3.6}$$

where J is the total inertia of the wind turbine. Then, combining the equations from (3.2) to (3.6), and assuming that $v_1 \approx v_2$ ($v_1 = v_2 = v$), the small-signal time constant can be obtained as,

$$\tau = \frac{J \cdot \lambda_0^2}{0.5 \cdot \rho \cdot A \cdot R^2} \cdot \frac{1}{3 \cdot C_{\mathrm{pmax}}} \cdot \frac{1}{v} \tag{3.7}$$

Note that Equation (3.7) can be rearranged as,

$$\tau = \frac{J}{3} \cdot \frac{\dfrac{\lambda_o \cdot v_{\mathrm{rated}}}{R}}{\dfrac{1}{2} \cdot \dfrac{C_{\mathrm{pmax}}}{\lambda_o} \cdot \rho \cdot A \cdot R \cdot v_{\mathrm{rated}}^2} \cdot \frac{v_{\mathrm{rated}}}{v}$$

$$= \frac{J}{3} \cdot \frac{\omega_{\mathrm{rated}}}{T_{\mathrm{rated}}} \cdot \frac{v_{\mathrm{rated}}}{v} \tag{3.8}$$

where, v_{rated} is the rated wind speed, ω_{rated} is the rated angular speed of the wind turbine and T_{rated} is the turbine torque at the rated wind speed.

In above analysis, the turbine time constant is derived by using a small step change of wind speed and the linearization of torque versus speed characteristics. This will introduce errors when analysing large-signal wind speed cases. Despite this, it is still useful to do this type of analysis as it is the only method to obtain analytical results for the non-linear system. These analytical results are useful as they provide physical insight of the key factors affecting the power reduction in the wind turbine.

3.3. Definition of the Natural Time Constant

The natural time constant in this thesis is defined as the small-signal turbine time-constant at the rated wind speed under the MPPT control at a constant pitch angle. Based on Equation (3.8), the natural time constant of a wind turbine τ_o is defined by,

$$\tau_o \equiv \frac{J}{3} \cdot \frac{\omega_{rated}}{T_{rated}} \tag{3.9}$$

From Equation (3.9), the natural time-constant τ_o is 1/3 of the time it takes rated torque to accelerate the wind turbine inertia (without considering any aerodynamic torque on the wind turbine) from standstill to the rated turbine speed. Therefore, the time constant as a function of the natural time constant τ_o can be given as,

$$\tau = \tau_o \cdot \frac{v_{rated}}{v} \tag{3.10}$$

In Equation (3.10), it can be seen that the turbine time constant under a certain wind speed depends on the natural time-constant of the wind turbine as the rated wind speeds for the different size wind turbines are similar. Therefore, the natural time-constant versus the power rating characteristics is useful to estimate the response time of a wind turbine at different wind speed levels using the information on its specifications.

3.4. Numerical Simulation under a Small-Step Change of Wind Speed

In this section, the numerical simulation is done in the wind turbine system model for a step wind speed change of ±0.1 m/s to obtain the turbine time-constant at different wind speeds. The parameters of the wind turbine system model are obtained from the specification [30] of an example fixed-pitch 400 W wind turbine as shown in Table 3.1.

Table 3.1 The parameters of the wind turbine system mode

Power rating	400 W
Rotor diameter	0.575 m
Rated wind speed	12 m/s
Blade pitch angle	0°
Optimal TSR	8.1
Maximum C_p	0.48
Density of air	1.225 kg/m^3

Note that, the optimal TSR and the maximum C_p in Table 3.1 is obtained from the C_p model in Fig. 2.6.

The turbine speed responses for the example fixed-pitch 400 W wind turbine with the rated wind speed of 12m/s is simulated at wind speeds of 6 m/s and 12 m/s as shown in Fig. 3.4. In Fig. 3.4, the turbine time-constant τ at the wind speed of 6 m/s is obtained under the step change of the wind speeds from 5.9 m/s to 6.1 m/s, and also the turbine time-constant at the wind speed of 12 m/s is obtained under the step change of the wind speeds from 11.9 m/s to 12.1 m/s. It can be seen that the turbine time-constant at the wind speed of 6 m/s (1.84 s) is double of that at the wind speed of 12 m/s (0.92 s) for the 400 W wind turbine, which matches the predictions from Equations (3.7) or (3.8) that the turbine time-constant is inversely proportional to the wind speed where doubling the wind speed results in halving the turbine time-constant.

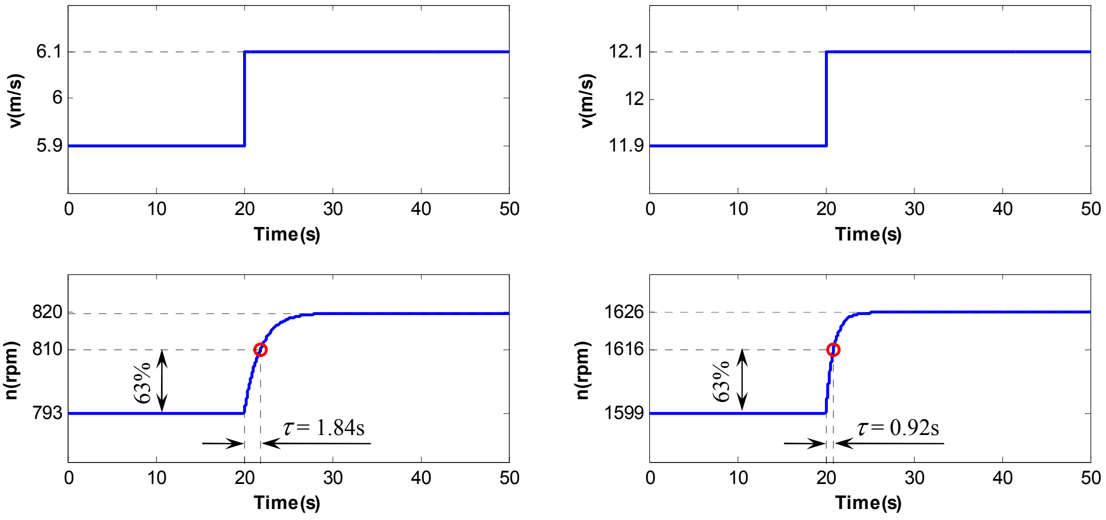

(a) τ with the wind speed of 6m/s

(b) τ with the wind speed of 12m/s

Fig. 3.4 The turbine time-constants for a 400 W wind turbine under MPPT with the wind speeds of (a) 6 m/s and (b) 12 m/s

The numerical results of the turbine time-constant are obtained from a series of simulations using the wind turbine system model at wind speeds from 1 m/s to 15 m/s, which are compared with the analytical results in Fig. 3.5, where *Analytical I* is calculated by using Equation (3.7) based on the same C_p characteristic, and *Analytical II* in Fig. 3.5 is calculated by using Equation (3.8) based on the specification.

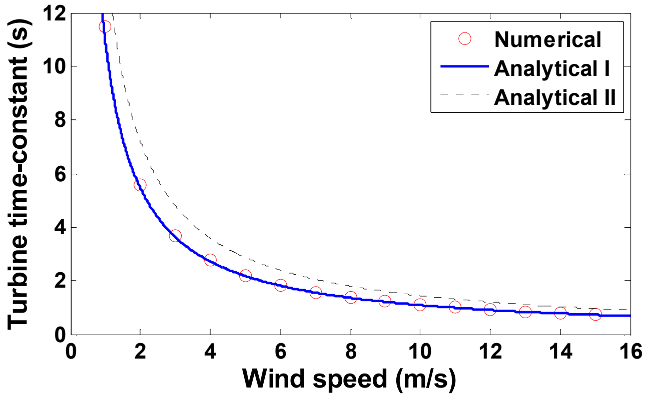

Fig. 3.5 The turbine time-constant versus wind speed based on comparing the analytical and the numerical approaches for the 400 W wind turbine under MPPT.

As illustrated in Fig. 3.5, the turbine time constant is inversely proportional to the wind speed. This is expected as the optimal turbine torque is proportional to the square of wind speed. Therefore, the response of turbines becomes faster when the wind speed increases. It also can be observed in the figure that the *Analytical I* curve perfectly matches the numerical result whilst the *Analytical II* curve is slightly higher than numerical result. This discrepancy is likely to be mainly due to the rated power provided on the turbine specification is the electrical output power which is less than the input mechanical power when the power losses on the generator and power electronics are included. In the calculation of the turbine time-constant using Equation (3.8), the rated torque is obtained from the rated power (rather than the input mechanical power) divided by the rated speed. In addition, the maximum C_p and the optimal *TSR* of the actual C_p characteristic of the example 400 W wind turbine could be different from the maximum C_p and the optimal *TSR* of the modelled C_p characteristic used in the wind system model. Comparing the two analytical results, the *Analytical II* is less accurate but easier to be obtained as the specification of a wind turbine is only needed. Therefore, this method is used in the thesis to calculate of the turbine time-constant and the natural time-constant.

For a variable-pitch wind turbine, the natural time-constant τ_o (the turbine time-constant at the rated wind speed) varies with the pitch angle γ as shown in Fig. 3.6.

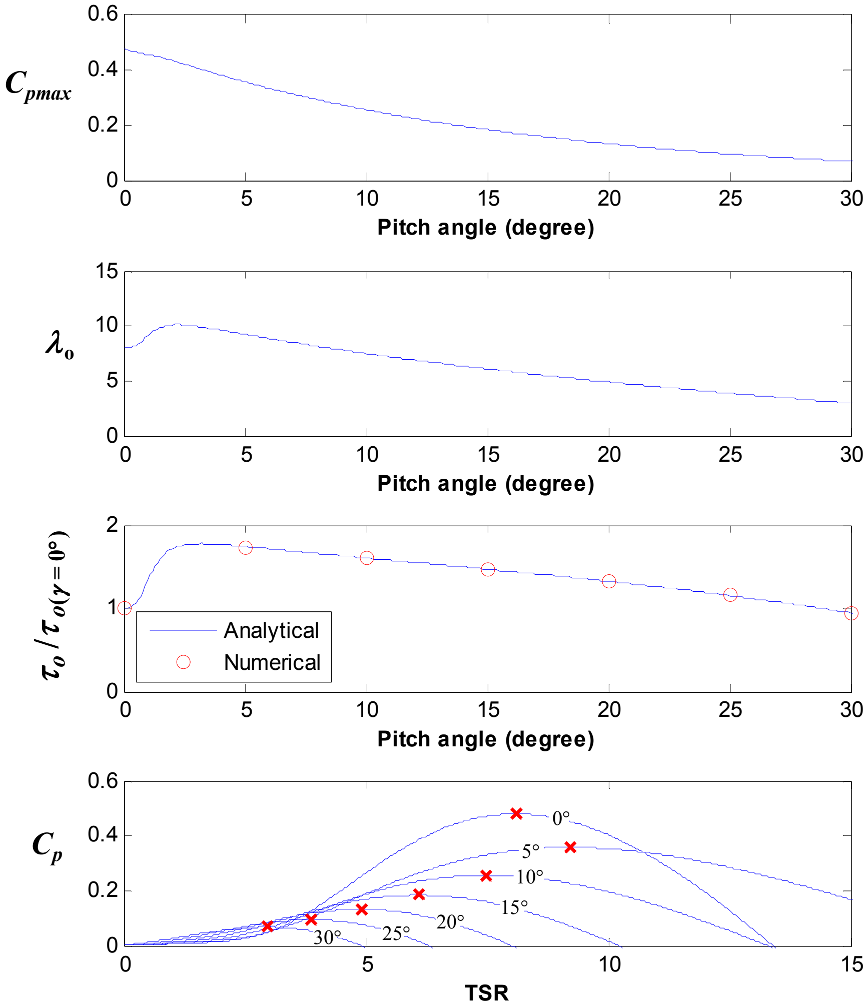

Fig. 3.6 The maximum C_p, the optimal TSR, and the natural time constant versus the pitch angle characteristics for a variable-pitch wind turbine

Fig. 3.6 shows the maximum power coefficient C_{pmax} decreases as the pitch angle increases, with the highest C_{pmax} at zero degree pitch angle. The optimal TSR λ_o increases for small pitch angles from 0° to 3°, which causes the natural time-constant to increase from 0° to 3° pitch angles. For larger values of pitch angle the natural time-constant decreases as the pitch angle increases. For this wind turbine model the natural time-constant at pitch angles of 0° and 30° are comparable. The natural time-constant under zero pitch angle is studied in the following chapters to investigate the dynamic power reduction due to the inertia of a wind turbine.

3.5. Prediction of Natural Time-Constant for Commercial Available Wind Turbines

As it was shown in Fig. 2.1, the effective inertia of a wind turbine includes the turbine inertia J_t and the rotor inertia of the generator J_g, where the former one is normally larger than the latter one. Therefore, the generator inertia J_g can be ignored in the large systems. The turbine inertia J_t is the sum of the inertia of all the blades. Since the shape of a turbine blade can be complex, in the analysis the blades of wind turbines are approximated to a simple triangular or a rectangular shape (see Fig. 3.7). Therefore, the moment of inertia of the blades can be obtained based on the parallel-axis theorem [31].

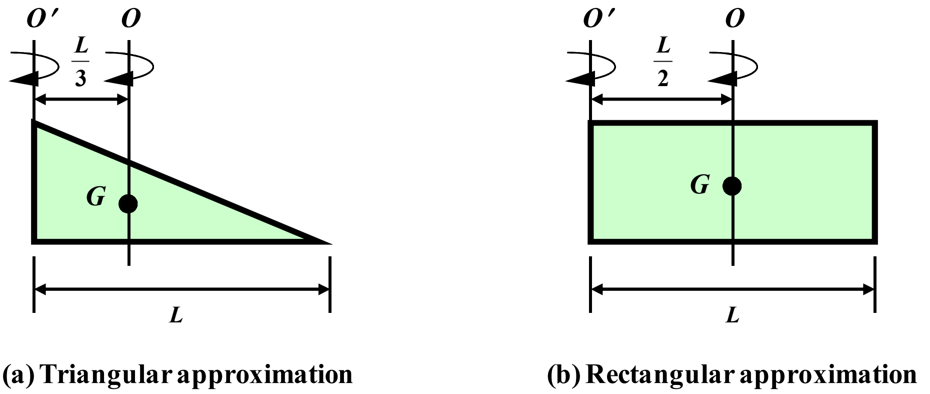

(a) Triangular approximation

(b) Rectangular approximation

Fig. 3.7 The mass movements of inertia of a triangular blade (a) and a rectangular blade (b) based on the parallel-axis theorem

In Fig. 3.7, the relationship between the inertia with respect to the axis O (crossing the centre of gravity G) and the inertia with respect to the axis O' can be given by,

$$J' = J + md^2 \tag{3.11}$$

Where, m is the total mass of the object; J is the moment of inertia with respect to the axis crossing the centre of gravity; J' is the moment of inertia with respect to the axis which is parallel with the axis crossing the centre of gravity; and d is the distance between the two axes. Hence, for the triangular approximation, the referred moment of inertia can be given by,

$$J_T' = J_T + m_T\left(\frac{L}{3}\right)^2 = \frac{1}{18}m_T L^2 + m_T\left(\frac{L}{3}\right)^2 = \frac{1}{6}m_T L^2 \tag{3.12}$$

Where, m_T is the mass of the triangular shape blade, and L is the length of the blade. In comparison, the referred moment of inertia for the rectangular approximation can be given by,

$$J_R' = J_R + m_R\left(\frac{L}{2}\right)^2 = \frac{1}{12}m_R L^2 + m_R\left(\frac{L}{2}\right)^2 = \frac{1}{3}m_R L^2 \tag{3.13}$$

Where, m_R is the mass of the rectangular shape blade, which is double the mass of the triangular shape, assuming that the densities of the blades are same. Therefore, the moment of inertia of the rectangular-shaped blade is four times greater than the moment of inertia of the triangular-shaped blade.

Based on the above analysis, the inertia of a turbine rotor can be given for the two blade shapes as,

$$J_{triangular} = \frac{1}{6}\cdot m_{rotor}\cdot R^2 \tag{3.14}$$

$$J_{rectangular} = \frac{1}{3}\cdot m_{rotor}\cdot R^2 \tag{3.15}$$

where, $J_{\text{triangular}}$ is the inertia of the rotor with triangular blades; $J_{\text{rectangular}}$ is the inertia of the rotor with rectangular blades; R is the radius of turbine rotor, which is equal to the length (L) of each blade; and m_{rotor} is the mass of the rotor blades, which can be defined as $m_{rotor} = 3\times m_R$ or $m_{rotor} = 3\times m_T$ for a three-bladed horizontal-axis wind turbine. For the rotor with triangular blades, the rotor mass can be roughly estimated by [12],

$$m_{rotor} = 2.947R^{2.6} \tag{3.16}$$

and for the rectangular blades, the mass of rotor is obtained as,

$$m_{rotor} = 5.894R^{2.6} \tag{3.17}$$

The natural time-constants of commercially available wind turbines have been calculated from their rotor diameter and rated speed and output power, and summarized in Table 3.2. This is based on the rough approximations in Equations (3.14)-(3.17) and (3.9).

Table 3.2 Calculated natural time-constants of commercially available wind turbines

	Known values			**Estimated values**				
	D m	**n_{rated}** rpm	**P_{rated}** MW	**m_{rotor}** kg	**J** $kg\cdot m^2$	**τ_o** s	**Manufacturer /Model**	**REF**
Fixed-pitch	1.17	1800	0.0004	0.7	0.04	1.2	SWWP Air X	[30]
	3.1	400	0.001	18	14.8	8.6	Enwind 1kW	[32]
	3.7	400	0.002	15	8.3	2.4	Enwind 2kW	[32]
	6.4	200	0.005	61	103	3.0	Enwind 5kW	[32]
	8	200	0.01	108	289	4.2	Enwind 10kW	[32]
	12	160	0.02	311	1865	8.7	Enwind 20kW	[32]
Variable-pitch	33	45	0.33	4.3×10^3	2×10^5	4.4	ENERCON E-33	[34]
	48	32	0.8	1.1×10^4	1.1×10^6	4.9	ENERCON E-48	[34]
	70.5	22.2	1.5	3.1×10^4	6.4×10^6	7.7	GE 1.5s	[33]
	82	19.5	2	4.6×10^4	1.3×10^7	9.0	ENERCON E-82	[34]
	90	16.8	2.3	5.9×10^4	2.0×10^7	8.9	Nordex N90	[35]
	104	15.3	3.6	8.5×10^4	3.8×10^7	9.1	GE 3.6	[33]

Note that the natural time-constant with zero pitch angle is shown for the variable-pitch wind turbines listed in Table 3.2.

According to Equation (2.3), when the wind turbine operates under steady-state at the rated wind speed v_{rated}, the rated angular speed ω_{rated} is inversely proportional to the radius of the rotor,

$$\omega_{rated} = \lambda_0 \, v_{rated} \cdot \frac{1}{R} \tag{3.18}$$

where, λ_0 is the optimal tip-speed ratio and v_{rated} is the rated wind speed of a wind turbine. The rated torque T_{rated} is proportional to the cube of the radius R,

$$T_{rated} = \frac{1}{2} \cdot \rho \cdot \frac{C_p}{\lambda} \cdot \pi \cdot v_{rated}^2 \cdot R^3 \tag{3.19}$$

As the inertia of the turbine rotor J_{rotor} is proportional to $m_{rotor} R^2$, where m_{rotor} can be either $m_{\mathrm{rotor}} \propto R^3$ (assuming a linear scaling of all dimensions), or alternatively $m_{\mathrm{rotor}} \propto R^{2.6}$

according to Equation (3.16) which comes from curve-fitting data from a large set of real wind turbines, hence, $J_{rotor} \propto R^5$ or $J_{rotor} \propto R^{4.6}$. Therefore, the relation between the natural time-constant τ_o and the radius of the wind turbines can be obtained based on Equation (3.13),

$$\tau_o \propto \frac{\frac{1}{R}}{3} \cdot \frac{R^5}{R^3} \propto R \tag{3.20}$$

or

$$\tau_o \propto \frac{\frac{1}{R}}{3} \cdot \frac{R^{4.6}}{R^3} \propto R^{0.6} \tag{3.21}$$

In addition, the relation between the power rating P_{rated} and the radius of the rotor R can be obtained by,

$$P_{rated} \propto T_{rated} \cdot \omega_{rated} \propto R^3 \cdot \frac{1}{R} = R^2 \tag{3.22}$$

Combining Equation (3.20) with (3.22), and (3.21) with (3.22), the relationship between the natural time-constant τ_o and the power rating P_{rated} is obtained as either,

$$\tau_o \propto P_{\text{rated}}^{0.5} \tag{3.23}$$

or

$$\tau_o \propto P_{rated}^{0.3} \tag{3.24}$$

The above analytical results can be used to estimate the trend of the natural time-constant versus power rating characteristics for wind turbines. The calculated natural time-constants of the commercially available wind turbine in Table 3.2 has been used to verify these predictions and model the trend as illustrated in Fig. 3.8.

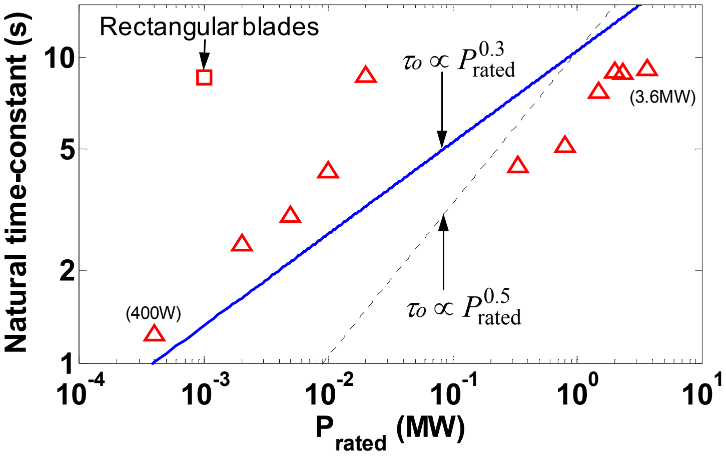

Fig. 3.8 The prediction of the trend of natural time-constant versus power rating for commercial wind turbines

In the above graph, wind turbines with rectangular blades (square) and triangular blades (triangles) have been included. It is clear that rectangular blade turbines have substantially larger natural time-constants. The natural time-constant of a wind turbine increases with its power rating, which can be approximately predicted by $\tau_o \propto P_{\text{rated}}^{0.3}$ for the triangular-blade wind turbines. The natural time-constant typically ranges from 1 s corresponding to small wind turbines (kW) to 10 s corresponding to large wind turbines (MW).

3.6. Turbine Time Constant for Large-Signal Wind Speed Variations

A step change of wind speed is the extreme scenario of the wind speed gusting behaviour. In reality, the wind speed changes continuously, such that the most common wind speed behaviour is the wind speed ramping, such as the sine-wave wind speed variation.

As the wind speed changes continuously, a large wind speed ramp can be seen as consisting of a finite number of the small step changes. From the above analysis, it is known that the small-signal time constant is inversely proportional to the wind speed. The effective time constant for a large wind speed ramp such as sine-wave wind speed can be approximated as the small-signal time constant at the average wind speed v_m as shown in Fig. 3.9.

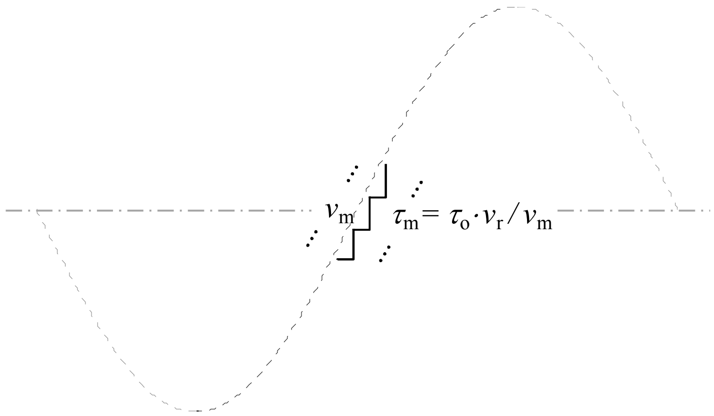

Fig. 3.9 Time constant for a large-signal sine-wave wind speed

Therefore, the time constant for a large wind speed ramp is then obtained by,

$$\tau = \frac{\tau_o \cdot v_r}{\frac{1}{T}\int_0^T v(t)dt} = \frac{\tau_o \cdot v_r}{v_m} \tag{3.25}$$

This time constant model can be applied to the large wind speed ramping but is not accurate for the large wind speed gusting due to the error caused by the approximation of time constant.

3.7. Summary

In this chapter, the dynamic response of wind turbines under MPPT to small step-changes of wind speed is modelled, and the analytical equation for the turbine time constant τ for a wind turbine is derived. The resultant equation shows the turbine time constant is inversely proportional to the wind speed $\tau \propto 1/v$, which demonstrates that a wind turbine will response faster under MPPT as the wind speed increases. The analytical results for the turbine time constant were calculated by using the derived equation, which were then compared with the numerical results for the turbine time-constant obtained from the simulations.

Furthermore, the definition of natural time constant τ_o was introduced in this chapter. The turbine time constant at the rated wind speed is defined as the natural time constant of a wind turbine under the MPPT control. This is approximately in the range from 1 s to 10 s. Finally, the natural time-constants of commercial wind turbines are calculated based on their rotor diameter and rated speed and output power. This is then compared with the predicted trend of $\tau_0 \propto P_{\text{rated}}^{0.3}$. Therefore, it was concluded that the response time for a wind turbine under MPPT at a certain wind speed can be approximately estimated from its ratings.

Chapter 4. Small-Signal Power Reduction: Infinite Inertia Model

4.1. Introduction

Due to the turbine inertia, the larger the amplitude of the wind speed variation, the lower the average output power will be obtained by MPPT. In this section, a sinusoidal wind speed variation is assumed in order to calculate the analytical power reduction with infinite inertia in the wind turbine system model.

The extreme cases of the inertia impact on the power reduction of wind turbines with the MPPT applied are illustrated in Fig. 4.1 with zero inertia ($J = 0$, the dotted lines) and infinite inertia ($J = \infty$, the solid lines). The averages of the variations are shown as the dashed lines (red for the zero inertia case and blue for the infinite inertia case) in Fig. 4.1. The parameters of the sample 400 W wind turbine [30] are used to simulate the variations of the system variables. The input wind speed is modelled as a sinusoidal variation with an average of 8m/s, a frequency of 0.1Hz, and an amplitude of 3m/s. The turbine speed with zero inertia $n_{J=0}$ is a scaled version of the wind speed variation, whilst the turbine speed with the infinite inertia $n_{J=\infty}$ is a constant value equal to the average of the turbine speed with zero inertia.

Note that, the turbine speed with infinite inertia $n_{J=\infty}$ is assumed, under small-signal conditions, to be equal to the optimal turbine speed corresponding to the average wind speed v_m. This is a key assumption in the analysis and is not intuitively obvious. This assumption is discussed further in Appendix C. There it is shown that the average turbine speed with infinite inertia is affected by the shape of the $C_p(\lambda)$ curve. For the representative $C_p(\lambda)$ curve used in this analysis, this assumption is valid, however it is also shown for extreme cases such as a "flat" or "triangular" $C_p(\lambda)$ curve this assumption fails.

It can be seen in Fig. 4.1 that, the turbine torque $T_{t(J=0)}$ is same as the generator torque $T_{g(J=0)}$ with zero inertia. In contrast, the turbine torque $T_{t(J=\infty)}$ with infinite inertia varies with the wind speed whilst the generator torque $T_{g(J=\infty)}$ with infinite inertia is constant and is approximately the average of the generator torque with zero inertia. The figure also indicates that the output power with infinite inertia is constant at 156 W, which is less than the average output power of 189 W with zero inertia. This corresponds to a power reduction of 8.3%.

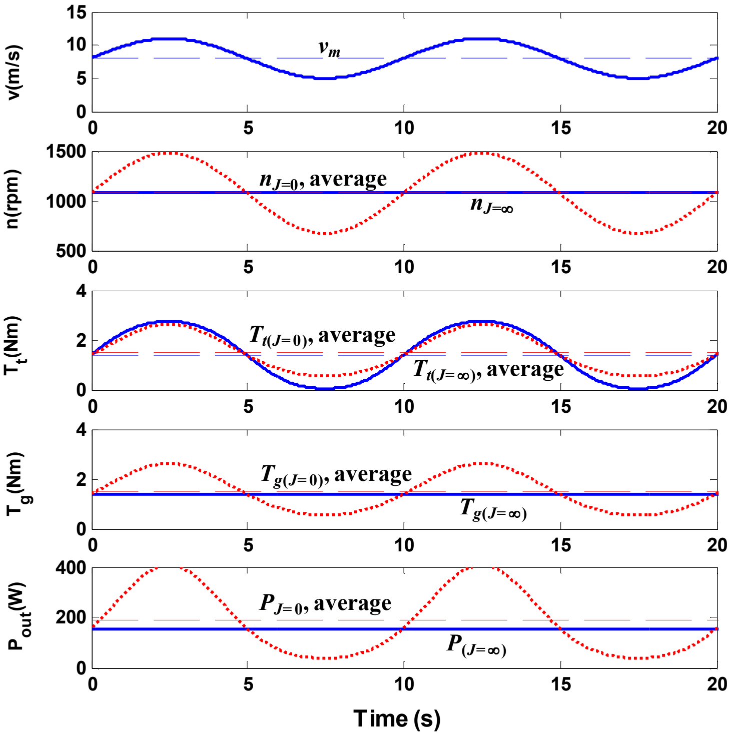

Fig. 4.1 The variations of system variables with zero inertia and infinite inertia for the 400 W wind turbine under the assumed sine-wave wind speed variation.

The inertia delays the response of turbine speed during the accelerations and decelerations as the wind speed changes. This results in the turbine speed with infinite inertia remaining constant at approximately the average of the turbine speed variation with zero inertia, where the occurrences of both the higher turbine speed and the lower turbine speed are reduced. Now as the output power is proportional to the cube of the turbine speed (see Equation (2.7)) thus the power gains from the increase in turbine speed above its mean value more than make up for the power loss from the turbine speed falling below its mean value. Thus the average output power with zero inertia will always be greater or equal to the infinite inertia case.

In this part of the study, square, triangular and sinusoidal variations are used to model the wind speed waveform. The analytical equation of the power reduction with infinite inertia is derived as a function of the parameters of the wind characteristic. The results obtained from the analytical equation have been compared with the numerical results obtained from the simulation in PSIM.

4.2. Analytical Equation of the Power Reduction

In Fig. 4.2, the parameters of the average wind speed v_m, the variance of the wind speed σ^2 and the peak variation of wind speed Δv are introduced and noted on the figure. Note that the optimal turbine speed is proportional to the wind speed. Therefore the concept of the equivalent wind speed v_{eq} is defined as an imaginary wind speed which is computed by dividing the actual turbine speed with the ratio k defined in Equation (2.9). Due to the existence of inertia, the equivalent wind speed v_{eq} is not equal to the real wind speed input unless the inertia equals zero. The equivalent wind speed v_{eq} is used in the following studies. For instance, for the infinite inertia case, the equivalent wind speed is the average wind speed v_m as shown in Fig. 4.2.

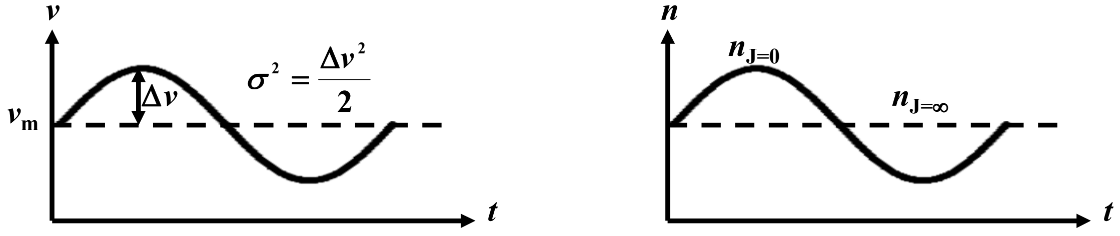

Fig. 4.2 The sinusoidal wind model and the corresponding turbine speeds

The variance σ^2 for a wind speed variation can be defined by,

$$\sigma^2 = \frac{1}{t_2 - t_1}\int_{t_1}^{t_2} (v - v_m)^2 \, dt \tag{4.1}$$

Where, t_1 is the starting time, t_2 is the ending time, v is the instantaneous wind speed and σ is the standard deviation of the wind speed.

For a sinusoidal wind speed variation, the ratio of the output power with infinite inertia $P_{\mathrm{J}=\infty}$ to the output power with the zero inertia $P_{\mathrm{J}=0}$ is obtained as,

$$\frac{P_{J=\infty}}{P_{J=0}} = \frac{v_{\mathrm{m}}^3}{\frac{1}{T}\int_0^T \left(v_{\mathrm{m}} + \Delta v \cdot \sin \omega t\right)^3 \mathrm{d}t} = \frac{1}{1 + \frac{3}{2} \cdot \frac{\Delta v^2}{v_{\mathrm{m}}^2}} \tag{4.2}$$

Where, T is the period of the waveform. Hence, the power reduction with infinite inertia for the sine-wave wind speed variation (J=∞) is obtained as,

$$\frac{\Delta P_{J=\infty}}{P_{J=0}} = 1 - \frac{P_{J=\infty}}{P_{J=0}} = \frac{\frac{3}{2} \cdot \frac{\Delta v^2}{v_{\mathrm{m}}^2}}{1 + \frac{3}{2} \cdot \frac{\Delta v^2}{v_{\mathrm{m}}^2}} \tag{4.3}$$

The variance of the sine-wave wind speed variation is given by,

$$\sigma^2 = \frac{\Delta v^2}{2} \tag{4.4}$$

Therefore, the power reduction with infinite inertia for the sine-wave wind speed variation is obtained as,

$$\frac{\Delta P_{J=\infty}}{P_{J=0}} = \frac{3 \cdot \frac{\sigma^2}{v_{\mathrm{m}}^2}}{1 + 3 \cdot \frac{\sigma^2}{v_{\mathrm{m}}^2}} \tag{4.5}$$

where the ratio σ/v_{m} is commonly defined as the turbulence intensity (TI) [36]. Equation (4.5) shows that the power reduction with infinite inertia is a function of the turbulence intensity. This equation also applies to the square and the triangular wind speed variation profiles which are shown in Fig. 4.3. As was indicated above, the square-wave variation is used to model wind speed gusting, and the sinusoidal and triangular variations are used to model wind speed ramps.

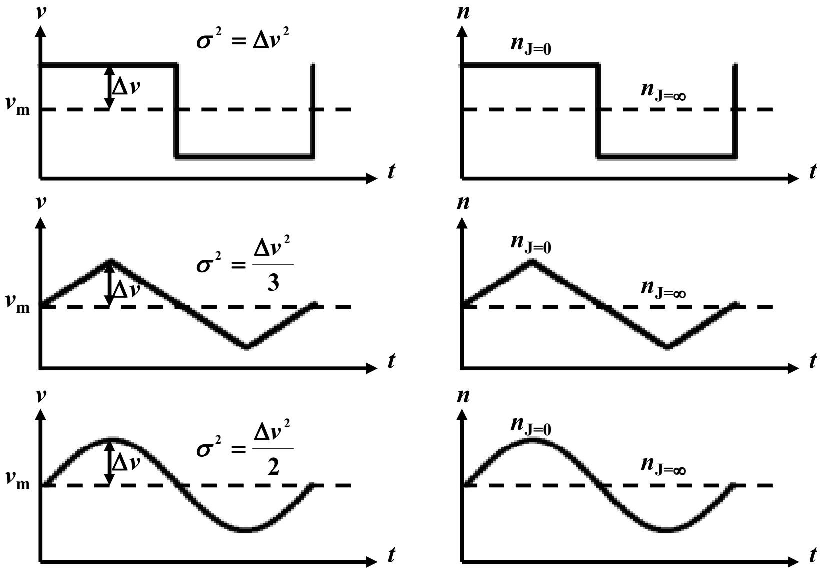

Fig. 4.3 The square, triangle and sinusoidal wind models and the corresponding turbine speeds with zero inertia and infinite inertia

For a square-wave wind speed variation, the power reduction with infinite inertia is,

$$\frac{\Delta P_{J=\infty}}{P_{J=0}} = 1 - \frac{v_m^3}{\frac{1}{2}[(v_m + \Delta v)^3 + (v_m - \Delta v)^3]} = \frac{3 \cdot \frac{\Delta v^2}{v_m^2}}{1 + 3 \cdot \frac{\Delta v^2}{v_m^2}} \tag{4.6}$$

Due to the variance of square-wave wind speed variation is given by,

$$\sigma^2 = \Delta v^2 \tag{4.7}$$

Combining Equations (4.6) and (4.7), the power reduction with infinite inertia for the square wind speed variation is obtained the same as Equation (4.5).

For a triangle-wave wind speed variation, the power reduction with infinite inertia is,

$$\frac{\Delta P_{J=\infty}}{P_{J=0}} = 1 - \frac{v_m^3}{\frac{1}{2\Delta v}\int_{v_m - \Delta v}^{v_m + \Delta v} v^3 \mathrm{d}v} = \frac{\frac{\Delta v^2}{v_m^2}}{1 + \frac{\Delta v^2}{v_m^2}} \tag{4.8}$$

Due to the variance of triangular wind speed is given by,

$$\sigma^2 = \frac{\Delta v^2}{3} \tag{4.9}$$

Combining Equations (4.8) and (4.9), the power reduction with infinite inertia for the triangle-wave wind speed variation is again obtained the same as Equation (4.5).

4.3. Numerical Simulation

The power reduction with infinite inertia calculated by the analytical equation given above is verified by the numerical simulation using the dynamic model of the wind turbine system. The parameters used in the numerical simulation were shown in Table 3.1. Similar to the previous assumptions, the square, triangular, and sinusoidal wind speed variations are studied in the numerical simulation.

Fig. 4.4 shows the power reduction with infinite inertia versus the ratio σ^2/v_m^2 (squared TI) for the numerical results compared with the analytical results.

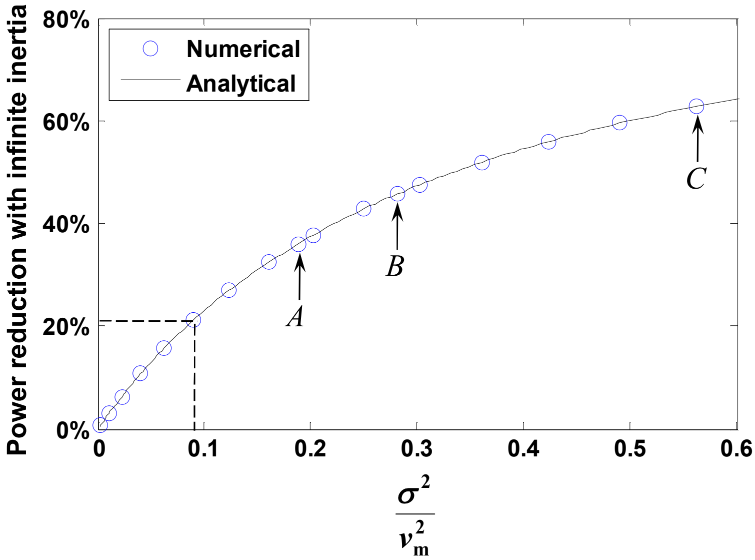

Fig. 4.4 The power reduction with infinite inertia versus σ^2/v_m^2. The analytical results (solid line) and the numerical simulation results (circles)

As it is shown in Fig. 4.4, the numerical simulation results match the analytical results. Moreover, for small values of the ratio σ^2/v_m^2 (squared TI) from 0 to 0.1, the power reduction is approximately twice the ratio σ^2/v_m^2 (squared TI), so that $\sigma^2/v_\mathrm{m}^2 = 0.1$

corresponds to a 20% power reduction. In addition, the frequency of the wind speed variation does not affect the power reduction with infinite inertia.

In Fig. 4.5, a sinusoidal variation of wind speed is given with an average value of 8 m/s, an amplitude of 6 m/s and a frequency of 0.1 Hz. The ratio σ^2/v_m^2 (squared TI) is calculated as 0.28 that corresponds to a 46% power reduction which is shown as point *B* in Fig. 4.4.

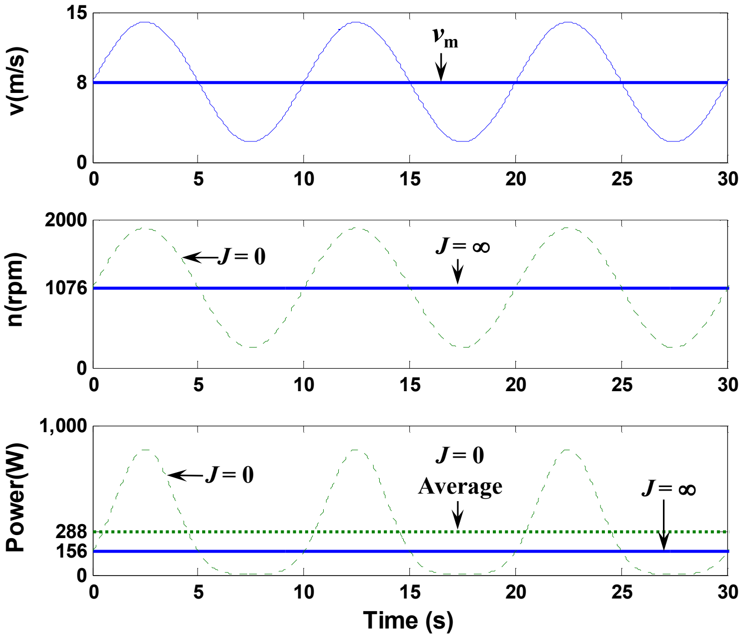

Fig. 4.5 The variations of system variables with the sinusoidal wind speed variation at Point *B* as highlighted in Fig. 4.4.

The variation of the output power with zero inertia is a distorted sine wave with a steep peak and a broad trough. This is due to the fact that the power is proportional to the cube of wind speed (see Equation (2.1)), and so the higher wind speeds generate much greater output power than the lower wind speeds.

In Fig. 4.6, the variations of the system variables under the triangular wind speed variation are shown. In this figure, a triangular variation of wind speed is given for an average of 8 m/s, an amplitude of 6 m/s and a frequency of 0.1 Hz. The ratio σ^2/v_m^2 (squared TI) is calculated as 0.19 that corresponds to 36% of the power reduction at point *A* in Fig. 4.4.

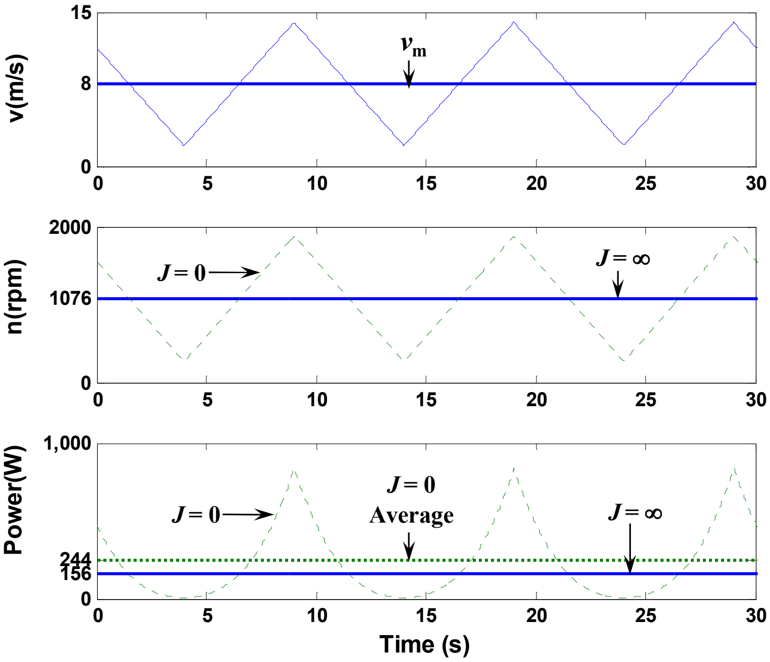

Fig. 4.6 The variations of system variables with the triangular wind speed variation at Point *A* highlighted in Fig. 4.4.

As was seen with the sinusoidal case, there is a steep peak and broad trough on the output power variation since the power is proportional to the cube of wind speed. This again demonstrates that the higher wind speeds generate greater output power than the lower wind speeds.

In Fig. 4.7, a square-wave variation of wind speed is given with an average value of 8 m/s, an amplitude of 6 m/s and a frequency of 0.1 Hz. The ratio σ^2/v_m^2 (squared TI) is calculated as 0.56 that corresponds to 63% of the power reduction at Point *C* in Fig. 4.4.

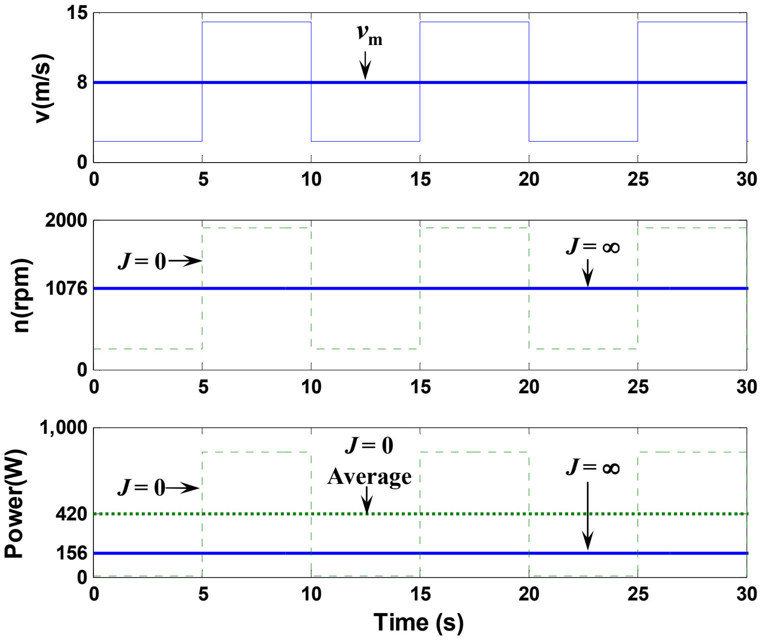

Fig. 4.7 The variations of system variables with the square wind speed variation at Point *C* highlighted in Fig. 4.4.

The output power waveform is still a square wave whilst the output power variations for the sinusoidal and triangular wind speed variations were distorted. The output power obtained at the higher wind speed is much greater than that obtained at the lower wind speed.

From the simulations shown above, it can be seen that the calculated results of the power reduction with infinite inertia from the analytical equation matches the numerical results obtained from the simulation using the dynamic model of the wind turbine. The parameters of the three wind speed variations and the power reduction with infinite inertia are summarised below in Table 4.1.

Table 4.1 The parameters of the wind speed variations used in the simulations

Variations	**v_m (m/s)**	**Δv (m/s)**	**σ^2/v_m^2**	***TI***	**$\Delta P_{(J=\infty)}$**
Sinusoidal	8	6	0.28	0.53	46%
Triangular	8	6	0.19	0.44	36%
Square	8	6	0.56	0.75	63%

In Table 4.1, although the average value and the amplitude are the same for all the three wind speed variations, the square wind speed variation has the maximum ratio σ^2/v_m^2 (squared TI), and hence the maximum turbulence intensity and the highest power reduction ($J = \infty$). Comparably, the triangular wind speed variation has the minimum turbulence intensity which then results the lowest power reduction.

4.4. Summary

Infinite inertia is an extreme condition that causes the maximum power reduction for the wind turbines in comparison to the zero-inertia condition. In this chapter, square, triangular and sinusoidal variations are used as the wind speed models, which represent typical wind behaviours (wind gusting and wind ramps). An analytical equation for the power reduction with infinite inertia was obtained as a function of the turbulence intensity of wind speed, which is identical for all three wind-speed variations. Moreover, the analytical results from the derived equation were compared with the numerical results from the simulation in PSIM®, and demonstrate a close match.

Chapter 5. Small-Signal Power Reduction: Finite Inertia Model

5.1. Introduction

The power reduction with infinite inertia has been found in the previous investigations. However, when the inertia of the wind turbine is not equal to zero or infinity, the analysis is more complex. The output power with finite inertia lies between the output power with zero inertia (the zero power reduction baseline case) and the output power with infinite inertia (the maximum power reduction case). Therefore, in this chapter a parameter β ($0< \beta <1$) is introduced to represent the effects of the finite inertia of wind turbines on the power reduction. This is a function of the product between the frequency of the wind speed variation and the time-constant of the wind turbine. Also, the equivalent frequency is a parameter defined to represent the wind speed variations. Furthermore, the numerical results obtained from simulation are compared with the analytical results calculated by the equation.

5.2. Analytical Equation of the Power Reduction

Due to the linear relationship between the wind speed and the optimal turbine speed, the equivalent wind speed v_2 with the given inertia J ($0<J<+\infty$) can be obtained as shown in Fig. 5.1 and Fig. 5.2,

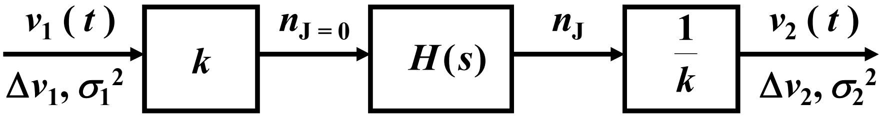

Fig. 5.1 The calculation of the equivalent wind speed

where v_1 is the given sine-wave wind speed and is also the equivalent wind speed with zero inertia; and v_2 is the equivalent wind speed of $n_{J,\ (0<J<+\infty)}$. The equivalent wind speed represents the actual turbine speed which is delayed due to the turbine inertia.

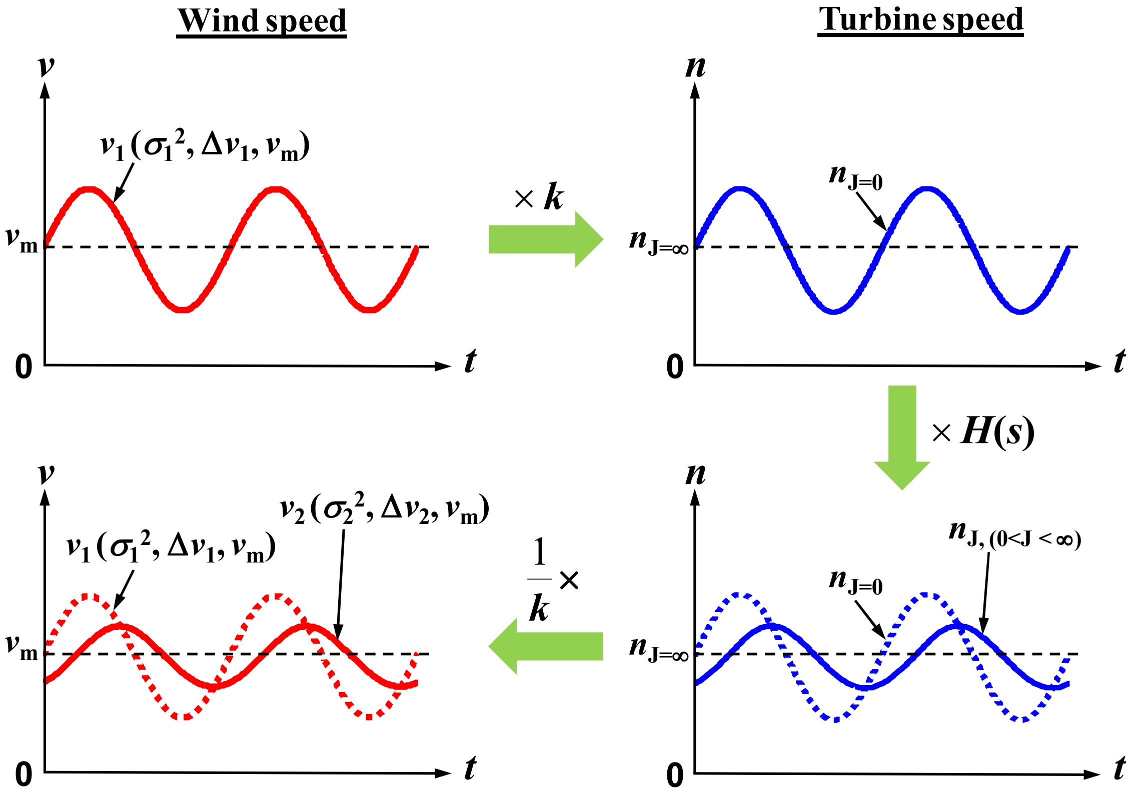

Fig. 5.2 The turbine speed responses for the zero inertia and finite inertia cases with a sinusoidal wind speed variation

Assuming small-signal conditions, the wind turbine is a first-order system, and so the transfer function $H(s)$ between the turbine speed with zero inertia and the turbine speed with finite inertia is given by,

$$H(s) = \frac{1}{1+s\tau} \tag{5.1}$$

where, τ is the time constant of the first-order system. Therefore, the ratio of the peak variations of the input (J=0) and the output (finite inertia) turbine speed is obtained as,

$$\frac{\Delta n_J}{\Delta n_{J=0}} = \frac{\Delta v_2}{\Delta v_1} = \left| \frac{1}{1+s\tau} \right| \tag{5.2}$$

where Δv_1 is the amplitude of v_1 and Δv_2 is the amplitude of v_2. The ratio of the variances of the input (J=0) and the output (finite inertia) turbine speeds is then obtained as,

$$\frac{\sigma_2^2}{\sigma_1^2} = \left(\frac{\Delta v_2}{\Delta v_1} \right)^2 = \left| \frac{1}{1+s\tau} \right|^2 = \left| \frac{1}{1+\mathrm{j}\omega\tau} \right|^2 = \frac{1}{1+\omega^2\tau^2} \tag{5.3}$$

where ω is the angular frequency, given by $\omega = 2\pi f$.

According to Equation (4.5), the power reduction with infinite inertia is only a function of the ratio σ^2/v_m^2 (squared TI). Therefore, the ratio of the output power with infinite inertia to the output power with zero inertia is obtained as,

$$\frac{P_{J=\infty}}{P_{J=0}} = \frac{1}{1+3\cdot\dfrac{\sigma^2}{v_\mathrm{m}^2}} \tag{5.4}$$

For any value of inertia, the output power P has the following relationship with σ^2/v_m^2,

$$P \propto 1+3\cdot\frac{\sigma^2}{v_\mathrm{m}^2} \tag{5.5}$$

Based on Equation (5.5), the ratio of the output power for the given inertia to the output power for zero inertia is obtained as,

$$\frac{P_J}{P_{J=0}}=\frac{1+3\cdot\frac{\sigma_2^2}{v_\mathrm{m}^2}}{1+3\cdot\frac{\sigma_1^2}{v_\mathrm{m}^2}} \tag{5.6}$$

Combining Equations (5.6) and (5.3) gives,

$$\frac{P_J}{P_{J=0}}=\frac{P_{\sigma_2}}{P_{\sigma_1}}=\frac{1+3\cdot\frac{\sigma_2^2}{v_\mathrm{m}^2}}{1+3\cdot\frac{\sigma_1^2}{v_\mathrm{m}^2}}=\frac{1+3\cdot\frac{\sigma_1^2}{v_\mathrm{m}^2}\cdot\frac{1}{1+\omega^2\tau^2}}{1+3\cdot\frac{\sigma_1^2}{v_\mathrm{m}^2}} \tag{5.7}$$

and the normalised power reduction for any turbine time-constant with the sine-wave wind speed variation is obtained as,

$$\frac{\Delta P_J}{P_{J=0}}=1-\frac{P_J}{P_{J=0}}=\left(\frac{3\cdot\frac{\sigma_1^2}{v_\mathrm{m}^2}}{1+3\cdot\frac{\sigma_1^2}{v_\mathrm{m}^2}}\right)\cdot\left(\frac{\omega^2\tau^2}{1+\omega^2\tau^2}\right) \tag{5.8}$$

where, τ is the turbine time constant for the small change of wind speed at v_m. The first term in Equation (5.8) denotes the power reduction with infinite inertia (see Equation (4.5)) whilst the second term is the scaling factor β ranging from 0 to 1, which represents the impact of the finite inertia,

$$\beta=\frac{\omega^2\tau^2}{1+\omega^2\tau^2} \tag{5.9}$$

5.3. Equivalent Frequency

Real wind speed versus time profiles are not sinusoidal. To analyse real wind speed data using (5.6), an equivalent frequency is defined. For the given sine-wave wind speed profile in Fig. 5.3, the equations for the wind speed $v(t)$ and rate of change of wind speed $\mathrm{d}v(t)/\mathrm{d}t$ are given by,

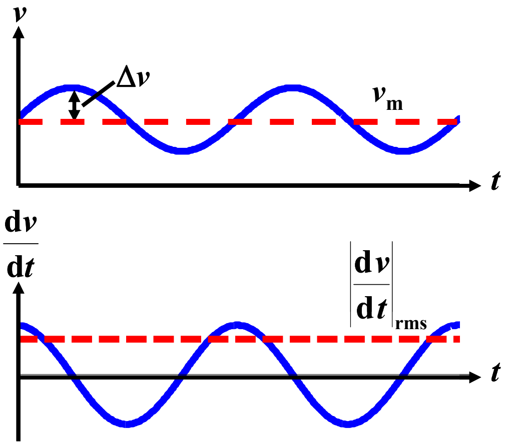

Fig. 5.3 The sinusoidal wind speed variation $v(t)$ and rate of change of wind speed $\mathrm{d}v(t)/\mathrm{d}t$

$$v(t) = v_\mathrm{m} + \Delta v \cdot \sin \omega t \tag{5.10}$$

$$\frac{\mathrm{d}v(t)}{\mathrm{d}t} = \Delta v \cdot \omega \cdot \cos \omega t \tag{5.11}$$

As the peak value of the sine wave is √2 larger than its rms value, the rms value of the rate of change of wind speed is given by,

$$\left|\frac{\mathrm{d}v(t)}{\mathrm{d}t}\right|_\mathrm{rms} = \frac{\Delta v}{\sqrt{2}} \cdot \omega_\mathrm{eq} = \sigma \cdot \omega_\mathrm{eq} \tag{5.12}$$

Hence, the equivalent frequency ω_eq can be defined as,

$$\omega_\mathrm{eq} \equiv \frac{\left|\frac{\mathrm{d}v(t)}{\mathrm{d}t}\right|_\mathrm{rms}}{\sigma} \tag{5.13}$$

The concept of equivalent frequency is used to evaluate the variation of real wind speed which is random in reality. As it is shown in Fig. 5.4, firstly the standard deviation and the rms value of the rate of change of wind speed are calculated for the given period of the real wind data. The two values calculated are then used to compute the equivalent frequency ω_eq according to Equation (5.13). In Fig. 5.4, two sample wind speed variations $v(t)$ and their rate of change of wind speed $\mathrm{d}v(t)/\mathrm{d}t$ are compared. The wind speed variation on the left has the lower standard deviation and also the lower rms value of the rate of change of wind speed whilst the one on the right has the higher standard deviation and also the higher rms value of the rate of change of wind speed. It was also observed that the equivalent frequency of the right one is higher than the one on the left, which is due to the fact that the increase of the rms value of the rate of change is larger than the increase of the standard deviation.

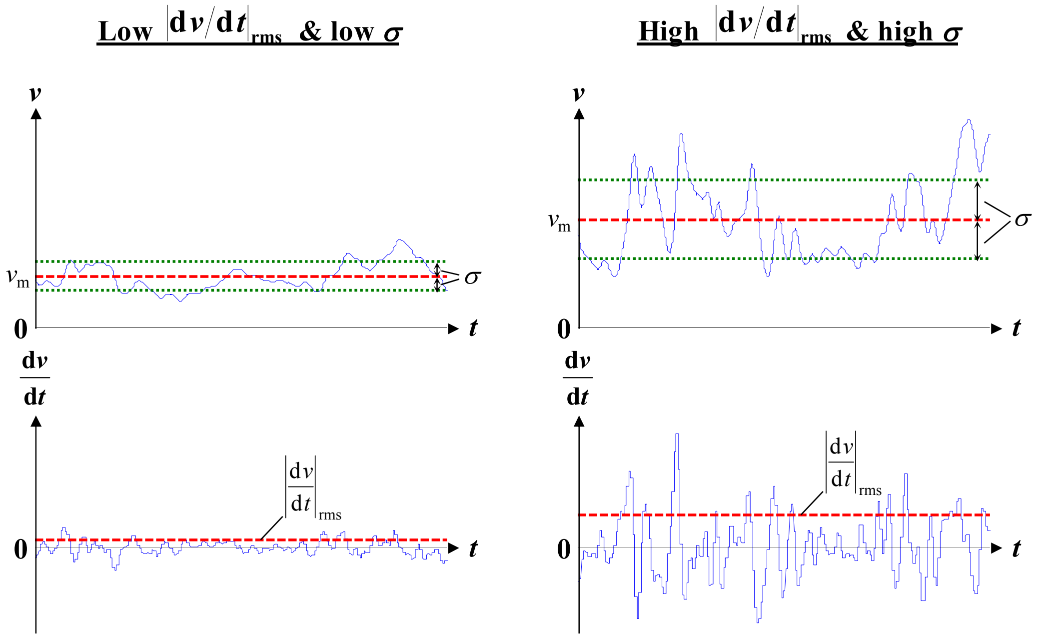

Fig. 5.4 The real wind speed variation $v(t)$ and rate of change of wind speed $\mathrm{d}v(t)/\mathrm{d}t$

5.4. Numerical Simulation

In this section, the numerical results of the power reduction with finite inertia obtained from the simulation using the dynamic model of the wind turbine are compared with the calculated results obtained from the analytical equation derived in the last section. The sinusoidal wind speed variations will be utilised in this investigation.

For the sinusoidal wind speed variation with an average value of 8 m/s and a frequency of 0.1 Hz, the power reduction versus the ratio of the variance to the square of the average wind speed is shown in Fig. 5.5. The calculated power reduction (solid lines) is compared with the numerical simulation (circles) for two sizes of wind turbine with the natural time constants of 4.9 s (800 kW) and 1.2 s (400 W) respectively. It can be seen that the power reduction with the natural time constant of 1.2 s is generally lower than that with the natural time constant of 4.9 s, and also both are less than the power reduction with infinite inertia (dotted line).

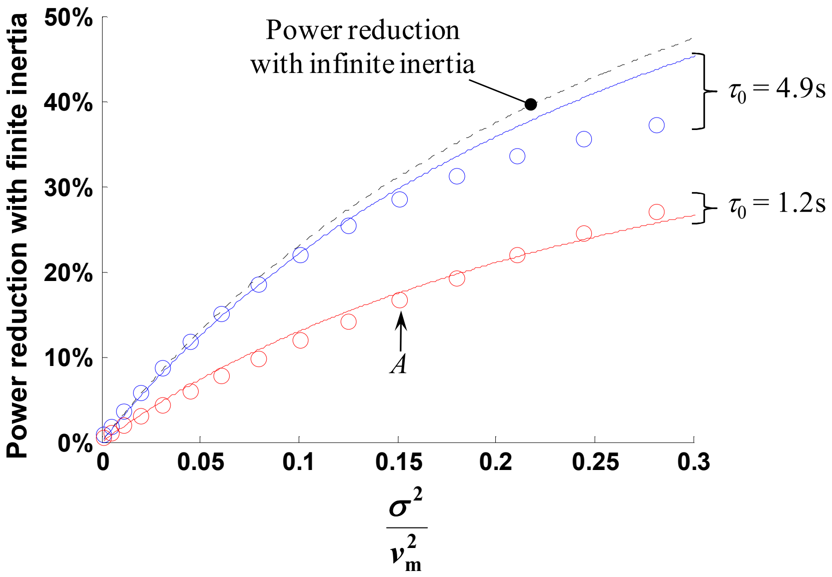

Fig. 5.5 The power reduction with finite inertia versus the ratio of variance to the squared average wind speed with a sinusoidal wind speed variation. Calculated results (solid lines), numerical results (circles) and the power reduction with infinite inertia (dotted line).

Note that, the numerical power reduction for the 800 kW wind turbine is calculated using the 400 W wind turbine model by changing the natural time constant to 4.9 s. In Fig. 5.5, the power reduction is approximately proportional to σ^2/v_m^2 (squared TI) at low variances when σ^2/v_m^2 increases from 0 to 0.1. Moreover, increasing inertia (natural time constant) increases the power reduction, which is limited by the power reduction curve with infinite inertia. This demonstrates that the larger wind turbine has a higher power reduction under MPPT.

It also can be seen in Fig. 5.5 that discrepancies exist between the analytical results and the numerical results at larger values of σ^2/v_m^2 (squared TI) for the two inertia cases. This is mainly due to the analytical equation being derived based on the small-signal response of the wind turbine without nonlinear effects being considered. In fact, for large wind speed variations the wind turbine system is a highly non-linear. The time constants for step increases in wind speed are slightly from the time constants for step decreases in the simulation with the dynamic model while the two are identical in a first-order linear system. In addition, the non-linear effects become increasingly significant as the variance of wind speed increases.

An example of the variation of system variables corresponding to Point *A* in Fig. 5.5 are depicted in Fig. 5.6. This shows the average values of the wind speed, the ideal output power with zero inertia, and the actual output power with the finite inertia corresponding to the natural time-constant of 1.2s. It can be seen that the turbine speed with zero inertia is a scaled version of the wind speed variation. In contrast, the turbine speed with the natural time constant of 1.2 s is an approximate sinusoidal variation with the same frequency as the wind speed, but lags the wind speed variation and is reduced in amplitude in comparison with the zero inertia case. This causes the variation of output power with the natural time constant of 1.2 s to become smoother compared with the zero inertia case. However, the average output power with zero inertia is 227 W whilst the average output power with the natural time constant of 1.2 s was reduced to 190 W which corresponds to a 16.3% power reduction.

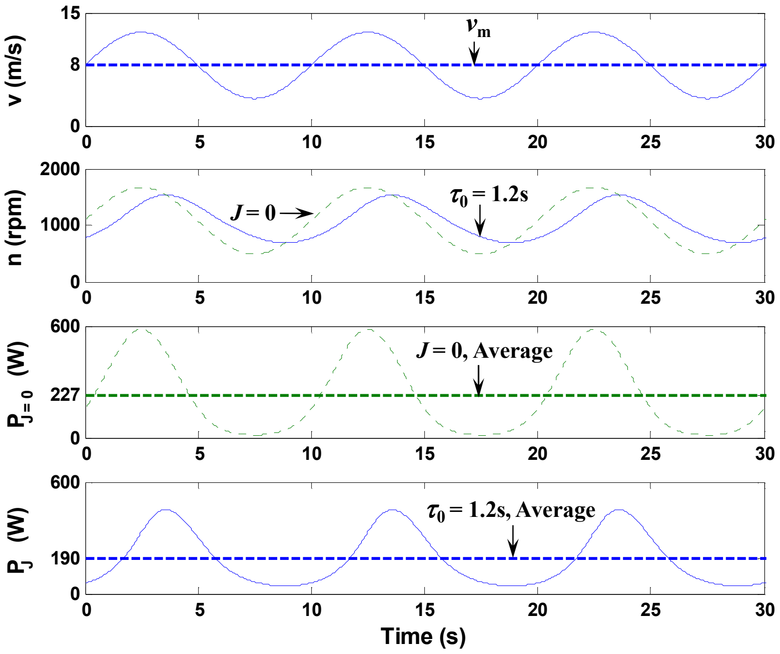

Fig. 5.6 The variation of system variables with the sinusoidal wind speed variation at Point *A* highlighted in Fig. 5.5.

In Fig. 5.7, the power reduction changes with the ratio of the natural time constant to the period of wind speed for different values of the ratio σ^2/v_m^2 are shown. Again, when σ^2/v_m^2 is larger, the analytical results of power reduction are higher than the actual values. In general, the analytical results match the numerical results when the ratio σ^2/v_m^2 is small where the non-linear effects of the wind turbine system are not significant.

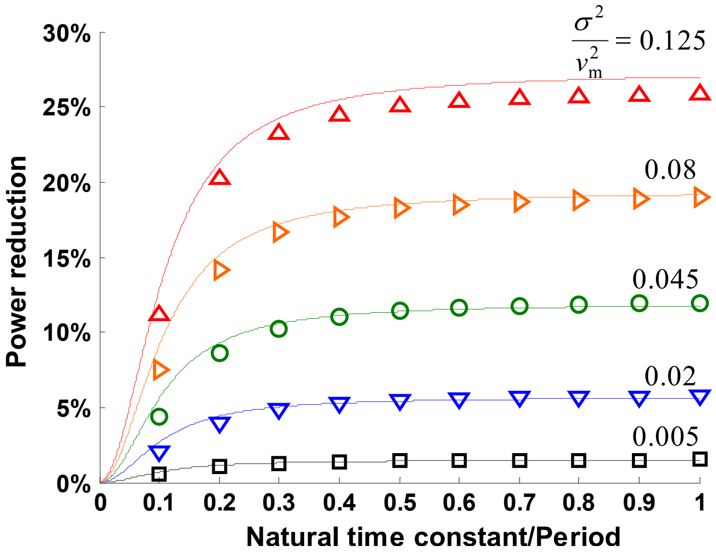

Fig. 5.7 The power reduction vs. natural time-constant/period with sine-wave wind speed variation for the analytical results (line) and simulated results (symbols).

5.5. Summary

In this chapter, the power reduction with finite wind turbine inertia is investigated by assuming a sinusoidal wind speed variation. The analytical equation of the power reduction with finite inertia consists of two components. The first component shows the power reduction with infinite inertia which is the extreme situation producing the maximum power reduction. The second component is the scaling factor β which represents the effects of finite inertia on the power reduction of wind turbines. The factor β is a function of the time constant at the average wind speed and the equivalent frequency of the wind speed which is defined based on the sinusoidal wind speed variation.

The simulations show that the results calculated by the analytical equation of power reduction with finite inertia basically matches the numerical results yielded by the dynamic model of wind turbine system at low ratios of σ^2/v_m^2 (squared TI) where the non-linear effects are not significant. In addition, larger inertia (natural time constant) of a wind turbine causes a higher power reduction under MPPT control, and a wind turbine with infinite inertia theoretically has the maximum power reduction.

Chapter 6. Simulation Study Using Real Wind Data

6.1. Introduction

Based on the analysis about the time constant in Chapter 2, the power reduction with infinite inertia in Chapter 3 and the power reduction with finite inertia in Chapter 4, the power reduction under real wind speed conditions is analysed in this chapter. The relationship between the power reduction and the natural time-constant is examined using eight sets of one-hour wind speed data which were recorded with an anemometer. Firstly, the parameters of the eight sets of wind speed data are calculated. Then, the power reduction versus the different parameters of the wind speed data is plotted to investigate their correlation.

6.2. Wind Data

Real wind data was used in the wind modelling. The wind data was recorded by Dr. Peter Freere during the period of December 1998 to February 1999 on the roof of building 36, at

Monash University, Australia. It was measured using a RIMCO rotating cup anemometer with a Picologger [37] attached to a PC to record the data. The recording time step was 0.5 s with a total period of 15 days, resulting in a total of 2.6×10^6 data points. Fig. 6.1 shows a histogram of the wind speeds in the wind data, and also the energy percentage that is generated by a wind turbine with the power characteristics in Fig. 6.1.

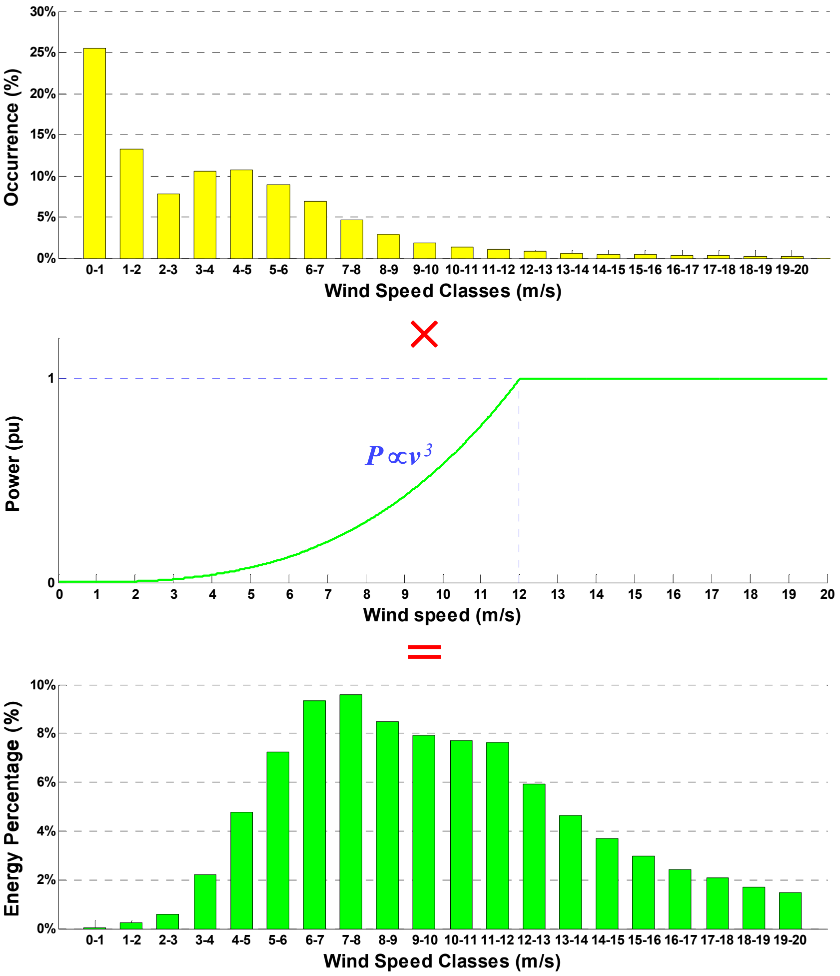

Fig. 6.1 The frequency of occurrence of the different wind-speed classes (a), the assumed wind turbine power versus wind speed characteristics (b), and the resulting energy of each wind-speed class (c) of the wind data

Note that, the rated wind speed of a wind turbine is commonly within the range from 12 m/s to 14 m/s. Here, the rated wind speed is chosen as 12 m/s in Fig. 6.1 in order to keep it consistent with the sample 400 W wind turbine. As shown in Fig. 6.1, the occurrence of the wind speeds less than 12 m/s takes a significant part (around 95% of the total occurrences) whilst the occurrence of the wind speeds above 12 m/s is pretty low (less than 5% of the total occurrence). This demonstrates that the wind turbine operates below the rated wind speed most of the time where MPPT control is used to maximise the output power. The power versus wind speed characteristics in Fig. 6.1 shows the wind turbine operates under MPPT control for the wind speeds below 12 m/s where the output power increase with the cube of wind speed, and operates with the constant power for the wind speeds above 12 m/s where the output power is kept constant as the wind speed increases. It should be noted that the energy percentage is obtained by multiplying the wind-speed class probability with the power characteristics. The result is then normalized with respect to the total energy. It can be seen that a wind turbine generates around 66% of the total energy for wind speeds below 12 m/s while around 34% of the total energy can be obtained for wind speeds above 12 m/s.

Eight sets of one-hour wind data were chosen from the above wind data record, which were used in the simulation studies. The wind data sets were chosen to illustrate a wide range of wind conditions (eight different wind conditions). The eight sets of wind data are presented in Fig. 6.2, and the parameters of the wind speeds and the analytical results of power reduction are listed in Table 6.1.

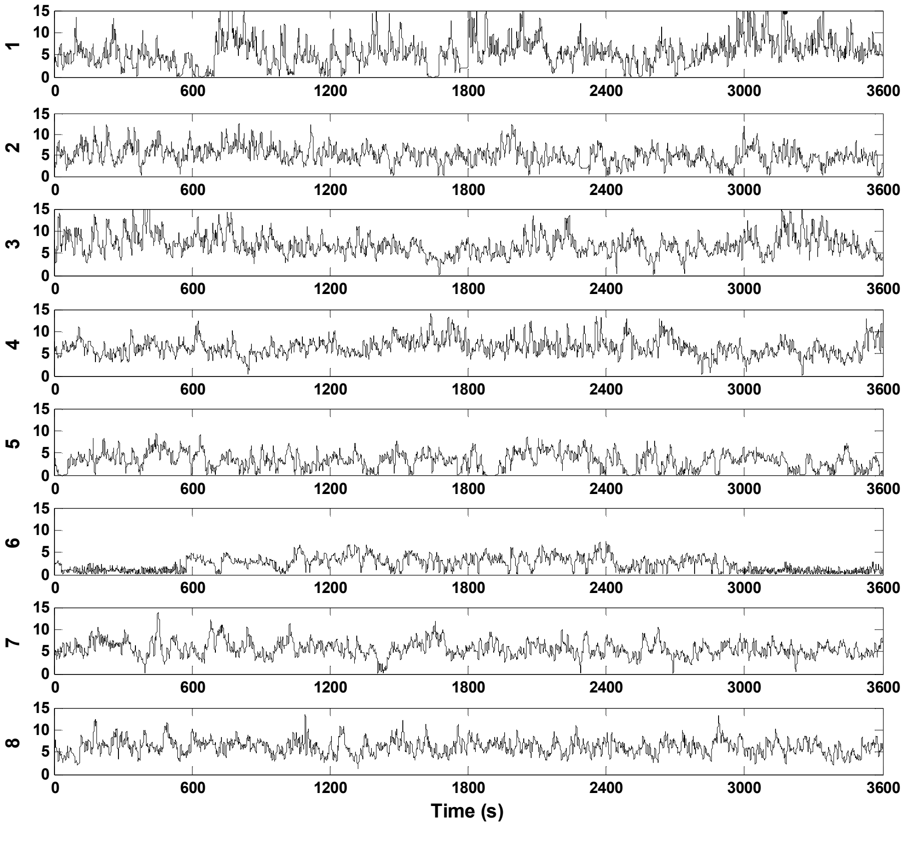

Fig. 6.2 The eight sets of one-hour wind speed data. The y-axis in each graph is wind speed in m/s.

Table 6.1 The analytical power reduction calculated from the parameters of the eight sets of one-hour wind data

Data set	Wind characteristics					Predicted power reduction				
	v_{m} (m/s)	v_{CMC} (m/s)	σ (m/s)	$\left\lvert\frac{\mathrm{d}v}{\mathrm{d}t}\right\rvert_{\mathrm{rms}}$	ω_{eq}	ΔP ($J=\infty$)	β ($\tau_o=1.2\mathrm{s}$)	β ($\tau_o=4.9\mathrm{s}$)	ΔP ($\tau_o=1.2\mathrm{s}$)	ΔP ($\tau_o=4.9\mathrm{s}$)
1	5.6	7.19	3.18	1.23	0.39	49%	50%	94%	25%	46%
2	5.04	5.81	2.08	1.08	0.52	34%	69%	97%	23%	33%
3	6.92	7.75	2.41	1.53	0.63	27%	63%	97%	17%	26%
4	6.45	7.01	1.93	1.41	0.73	21%	73%	98%	15%	21%
5	3.3	4.18	1.92	0.75	0.39	50%	74%	98%	38%	49%
6	2.33	3.19	1.60	0.62	0.38	59%	85%	99%	50%	58%
7	5.64	6.17	1.78	0.87	0.49	23%	61%	96%	14%	22%
8	6.14	6.59	1.70	1.14	0.67	19%	71%	98%	13%	18%

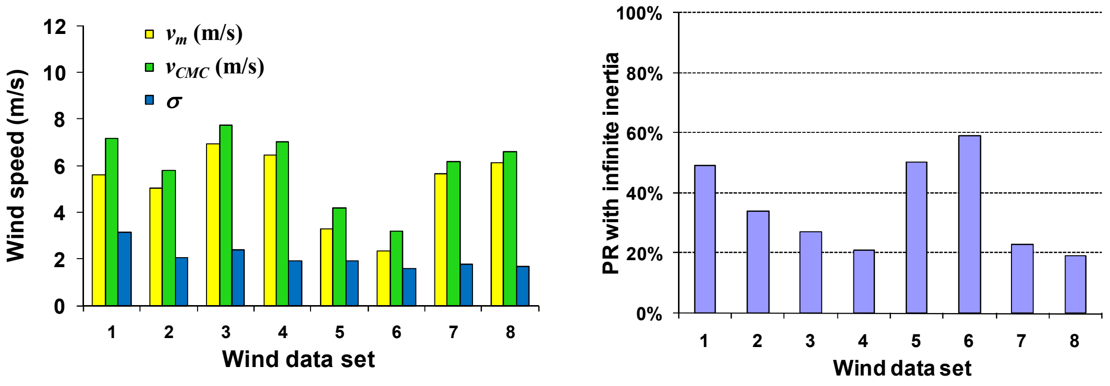

(a) Parameters of the wind speed characteristics (b) Power reduction (PR) with infinite inertia

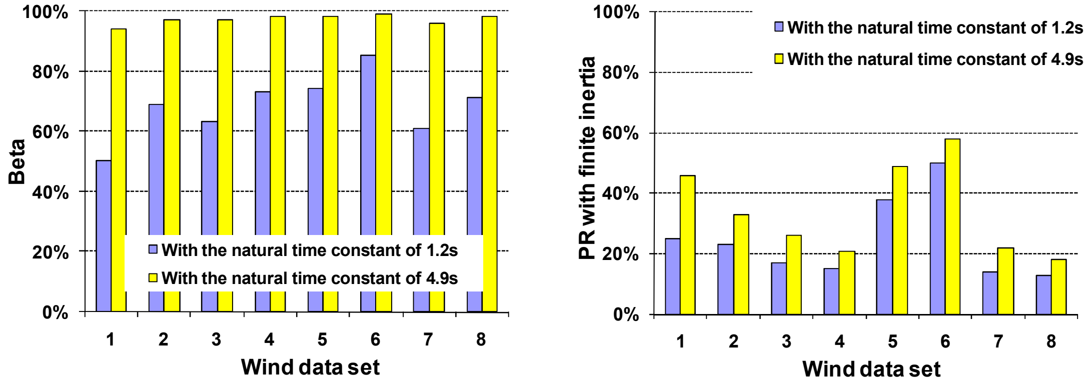

(c) The factor of inertia effects β (d) Power reduction (PR) with finite inertia

Fig. 6.3 Bar charts showing the parameters of the wind data and the calculated power reduction based on the analytical equation

Based on the values in Table 6.1 and bar charts in Fig. 6.3, it can be seen that, due to the relationship between the power extracted and the wind speed, $P \propto v^3$, the cube-root-mean-cube of wind speed v_{CMC} theoretically predicts the power available in the wind.

Therefore, data sets 1, 3 and 4 contain relatively high energy. Due to the highest variance of data set 1 and the relatively low average wind speed of data sets 5 and 6, the power reduction with infinite inertia of these data sets are the highest.

It was shown in Table 3.2 that a 400 W wind turbine corresponds to the natural time constant of 1.2 s while an 800 kW wind turbine corresponds to the natural time constant of 4.9 s. It was also shown in Equations (5.8) and (5.9) that the inertia impact on the power reduction can be analysed based on the factor β which is the ratio between the power reduction with infinite inertia ΔP (J=∞) and the actual power reductions of ΔP (τ_o=1.2 s) and ΔP (τ_o=4.9 s). It can be seen in Fig. 6.3 (c) that, even for a small wind turbine (e.g. 400 W, τ_o=1.2 s), the factor β is substantial and significant changes in β exist with different wind data sets. For large wind turbines (e.g. 800 kW, τ_o=4.9 s), the values of β are close to 100% and little change in β occurs with different wind data sets. The increased factor β for large wind turbines results in a larger power reduction in comparison to small wind turbines as shown in Fig. 6.3 (d).

6.3. Simulation of Power Reduction without Constant Power Operation

The power reduction of the wind turbines based on MPPT under varying wind speed conditions depends on both of the wind characteristics and turbine characteristics according to the previous analysis. The parameters of wind characteristics are the average wind speed v_m, the standard deviation of wind speed σ and the equivalent frequency of the wind speed ω_{eq}, whilst the parameters of the turbine characteristics are the natural time constant τ_o and rated wind speed. In this section, simulation results will be provided by using the real wind data in order to compare the numerical results with the calculated results using the analytical equation.

The power reduction with infinite inertia is a function of the ratio σ^2/v_m^2 (squared TI), which is mainly dependent on the wind characteristics according to the analytical equation derived. In the previous chapters, the validation of the analytical equation with infinite inertia was proved by the simulation using square, triangular, and sinusoidal wind speed variations. In Fig. 6.4, the analytical equation of the power reduction with infinite inertia (see Equation (4.5)) is verified with the numerical power reduction generated from the dynamic model of the wind turbine system by using the eight wind data sets.

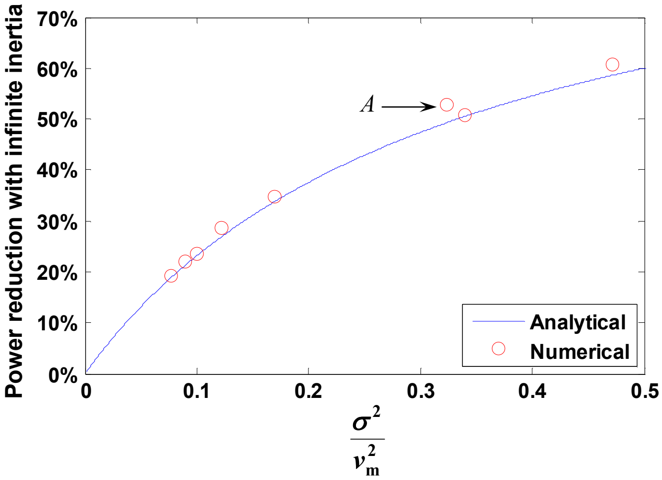

Fig. 6.4 The power reduction with infinite inertia versus the ratio of σ^2/v_m^2 for the eight sets of wind data sets: Analytical results (line) and numerical results (circles)

Point A highlighted in Fig. 6.4 corresponds to the wind data set 1. Note that the average wind speed v_m is the equivalent wind speed for the infinite inertia case. It can be seen from Fig. 6.4 that the analytical results generally match the simulation results apart from small, probably numerical, discrepancies at two points. The variation of the output powers with zero inertia and infinite inertia for wind data set 1 is given in Fig. 6.5 along with their average values. The simulations were done with the parameters of the sample 400 W wind turbine which were shown in Table 3.1.

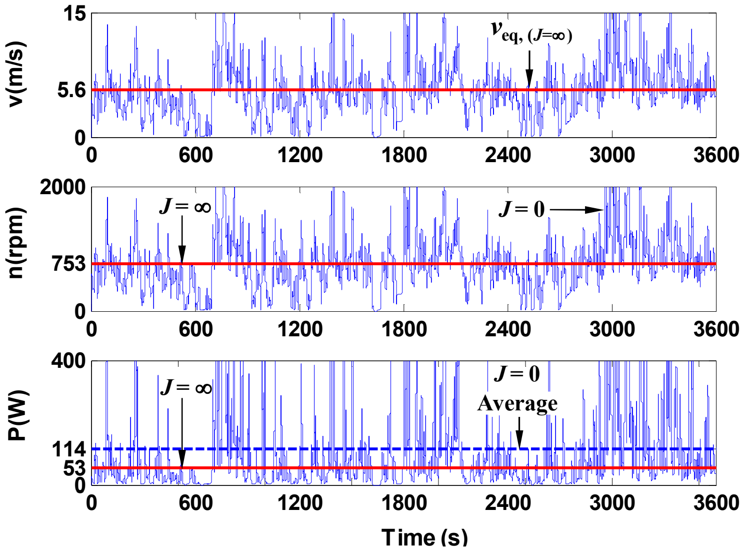

Fig. 6.5 The wind speed, turbine speed and output power for wind data set 1 corresponding to Point A in Fig. 6.4; two cases are shown: zero and infinite inertia.

In the following, the power reduction with finite inertia is investigated by using both the analytical equation and the numerical simulation of the wind data sets. With the wind data set 1 listed in Fig. 6.2, the variation of turbine speeds based on three different natural time-constants are shown in Fig. 6.6,

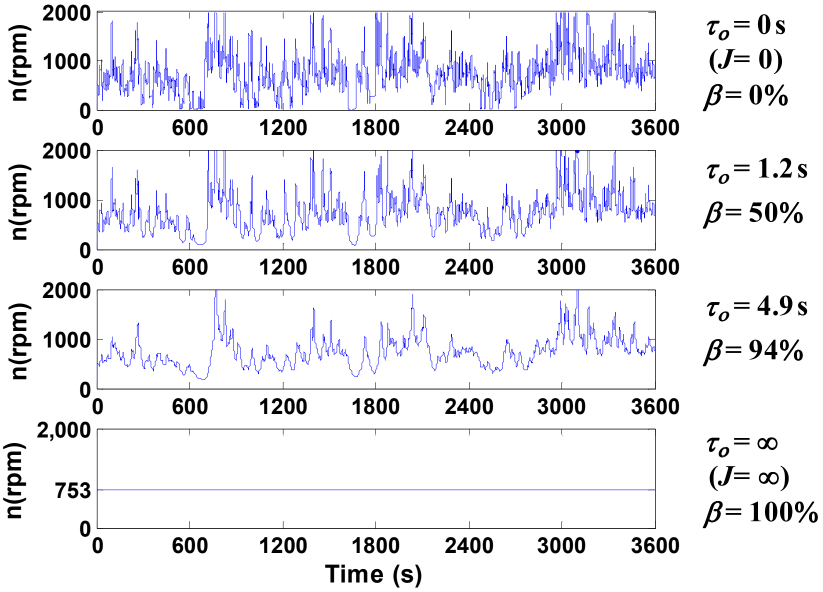

Fig. 6.6 The turbine speed variations for three different natural time-constants for the first wind data set

Fig. 6.6 shows that the turbine speed varies less as the natural time-constant increases, which corresponds to an increasing size of the wind turbine. This demonstrates that the capability of tracking the dynamically varying maximum power point is reduced in large wind turbines. In Fig. 6.6, the variation of turbine speed becomes much smoother as the natural time-constant increases since that the larger inertia (or natural time constant) results a greater first-order delay. The turbine speed with infinite inertia is assumed as the average value of the turbine speed with zero inertia ($\tau_o = 0$), which stays constant at 753rpm in Fig. 6.6.

In Fig. 6.7, the simulations have been done using the dynamic model with a natural time constant $\tau_o = 4.9$ s for the eight sets of one-hour wind data. The numerical results of power reduction are then compared with the analytical results shown in Table 6.1.

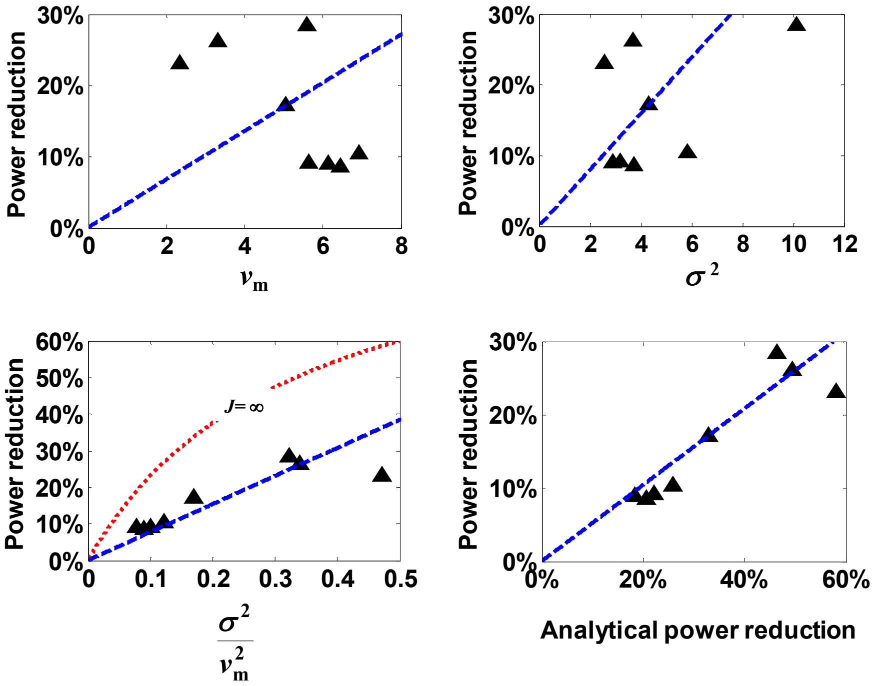

Fig. 6.7 Plots of power reduction versus four parameters: mean wind speed v_m, wind speed variance σ^2, σ^2/v_m^2 and analytical power reduction with τ_o=4.9 s.

In Fig. 6.7, no relationship was observed in the power reduction versus the mean wind speed v_m and the power reduction versus the wind speed variance σ^2 graphs. However, it can be seen that the power reduction versus σ^2/v_m^2 (squared TI) is close to a linear trend when σ^2/v_m^2 is relatively small and is limited by the analytical power reduction with infinite inertia (see Equation (4.5)). The linear trend of power reduction versus σ^2/v_m^2 (squared TI) is expected as the inertia-effect factor β for the eight sets of wind speed data is similar (see Table 6.1, τ_o=4.9 s). The simulated power reduction shows a good correlation with the analytical prediction but is approximately half of the analytical power reduction. This discrepancy could be due to the assumption in the calculation of inertia-effect factor β, as the real turbine time constant varies with wind speed instantaneously while the time constant corresponding to the average wind speed of one-hour wind data is used to calculate the inertia-effect factor β (see Equation (5.9)). Theoretically, the average wind speed for a shorter period of wind data produces a more accurate value of inertia-effect factor β, as the average wind speed is closer to the instantaneous wind speed.

As indicated earlier, the analytical model of the turbine time constant is derived based on small-signal changes in wind speed. Besides, the analytical model of power reduction was derived based on sinusoidal wind speed variations using a linearised model.

The analytical results were validated with simulations of significant wind speed variations (e.g. varying from 5 to 11m/s) and have demonstrated a good correspondence. However since the real wind data is clearly neither small-signal nor periodic variation, the analytical methods would not be expected to give accurate power reduction estimates. Despite this, they still predict the same trends as the simulation results (see Fig. 6.7). They also provide valuable physical insights into why one wind profile has higher power reduction than another wind profile by comparing their variance, equivalent frequency and average wind speed.

The output power using the wind data set 1 is shown in Fig. 6.8, which corresponds to the turbine speeds in Fig. 6.6. As the natural time constant (or inertia) increases, the average output power is reduced. The maximum average output power in per unit (0.28 pu) for the wind turbine under MPPT is obtained with zero inertia ($\tau_o = 0$ s). The output power with two different natural time-constant 1.2 s and 4.9 s is compared, and the average power is indicated with a dashed line in Fig. 6.8. The average power with the natural time-constant of 1.2 s which corresponds roughly to a 400 W wind turbine is 0.25 pu, hence the power reduction is 11%, and it is 0.20 pu with the natural time-constant of 4.9 s, which corresponds roughly to an 800 kW wind turbine, hence the power reduction is around 29%. Moreover, the wind turbine with infinite inertia ($\tau_o = \infty$) produces 0.13 pu output power with a maximum power reduction of 54%. These results clearly demonstrate that an increase in the natural time-constant, hence the power ratings, causes significant reduction in the output power under dynamic wind conditions.

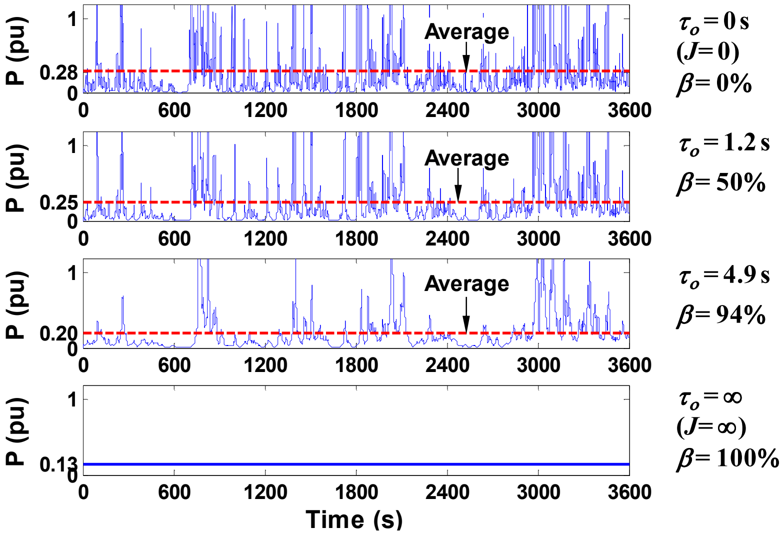

Fig. 6.8 The output power without constant power operation.

In Fig. 6.9, the calculated power reduction versus power rating of the wind turbine using the eight sets of wind data (labelled with the numbers 1-8) is given. Firstly, the natural time constant τ_o versus power rating P_{rated} characteristics in Fig. 6.9 is assumed the same as the predicted trend in Fig. 3.8. Next, the dynamic model was used to calculate the power reduction as a function of time constant and hence turbine power rating for each of the eight data sets. It can be seen that, the power reduction increases relatively fast with the power rating when the power rating is small (≤ 0.1 MW) but increases relatively slowly when the power rating becomes large (≥ 0.1 MW). The power reduction is strongly affected by the wind characteristics and so significant differences exist in the power reductions with different wind data sets. Also, the power reductions for wind data set 2 are simulated in the dotted lines by scaling the calculated natural time constant with the factor 2 and 0.5 respectively as shown in Fig. 6.9 to gain some perspective on the sensitivity of the results. The power reduction increases or decreases by around 5% with the scaling of the natural time-constant.

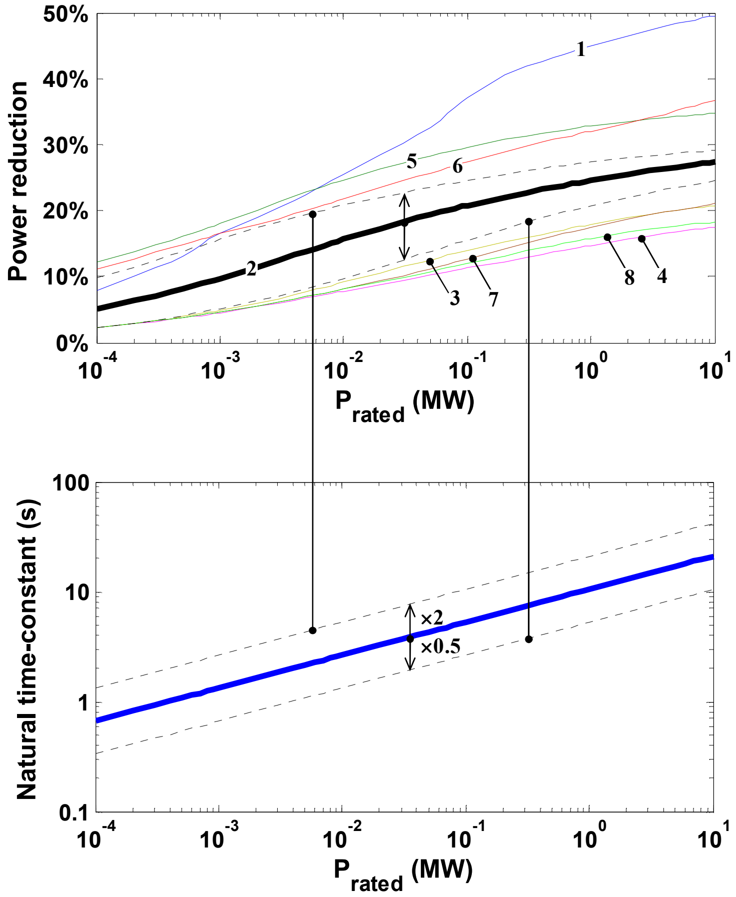

Fig. 6.9 Calculated power reduction and natural time-constant versus power rating for the eight sets of one-hour wind speed data; the power reduction of the 2nd set wind data by scaling the natural time-constant with the factors of 2 and 0.5 presented in the dotted lines.

6.4. Simulation of Power Reduction with Constant Power Operation

In Section 6.3, the simulation study of power reduction without constant power operation (see Fig. 6.10 (a)) was presented as the wind turbine system operates under the MPPT at all wind speeds. Therefore, the output power increases with the cube of turbine speed, $P \propto n^3$. In this section, the effect of constant power operation is included into the investigation of power reduction due to inertia as shown in Fig. 6.10 (b). The constant power operation limits the output power at wind speeds above the rated wind speed for protection purposes (see details in Appendix B). Therefore, the wind turbine operates under the MPPT control when wind speed is below the rated wind speed v_{rated}, and when wind speed is above the rated wind speed v_{rated} the wind turbine operates with a constant power of 1pu.

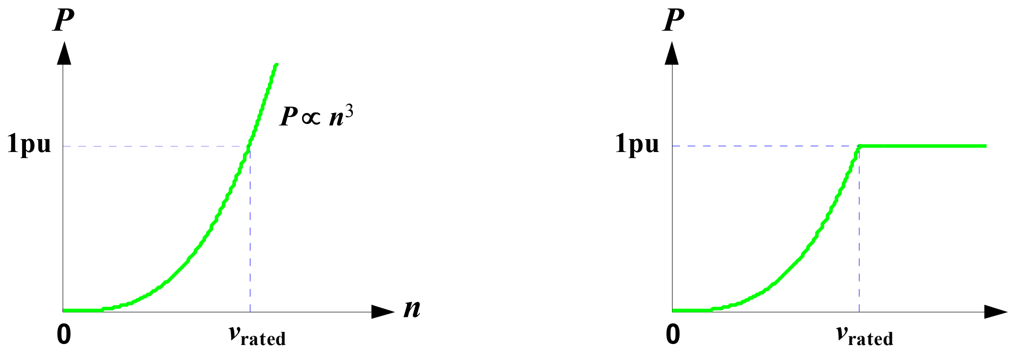

(a) Without constant power operation **(b) With constant power operation**

Fig. 6.10 The power versus turbine speed characteristics without constant power operation (a) and with constant power operation (b).

Based on the principle in Fig. 6.10 (b), the output power using the turbine speed in Fig. 6.6 is shown in Fig. 6.11 with constant power operation above the rated wind speed. This is to be compared with Fig. 6.8 which shows the results without constant power operation.

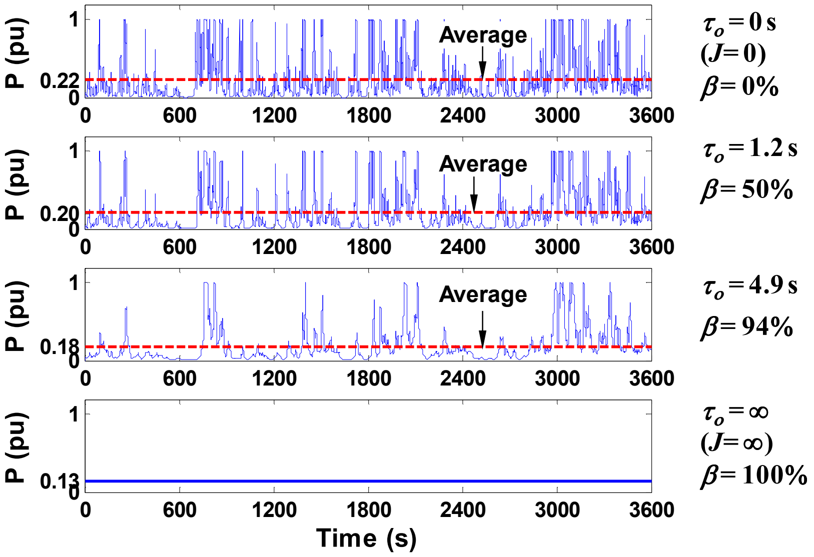

Fig. 6.11 The output power with constant power operation.

In Fig. 6.12, the average output power and the power reduction as a function of natural time constant are shown for the cases with and without constant power operation using the wind data set 1. The average output power and the power reduction with natural time constants of 1.2 s and 4.9 s are highlighted with the dots. The average output power with zero inertia ($\tau_o = 0$ s) obtained with constant power operation is 0.22 pu which is less than that obtained without constant power operation (0.28 pu). Moreover, a wind turbine with the natural time constants of 1.2 s and 4.9 s generates an average power of 0.25 pu and 0.20 pu respectively without the constant power operation whilst it generates 0.20 pu and 0.18 pu respectively with constant power operation. Furthermore, a wind turbine with the natural time constants of 1.2 s and 4.9 s produces a power reduction of 11% and 29% without constant power operation whilst it produces a power reduction of 9% and 18% with the constant power operation. The analytical power reduction is generally two times larger than the power reduction with constant power operation, and the reduction without constant power operation is obtained in between of them in Fig. 6.12.

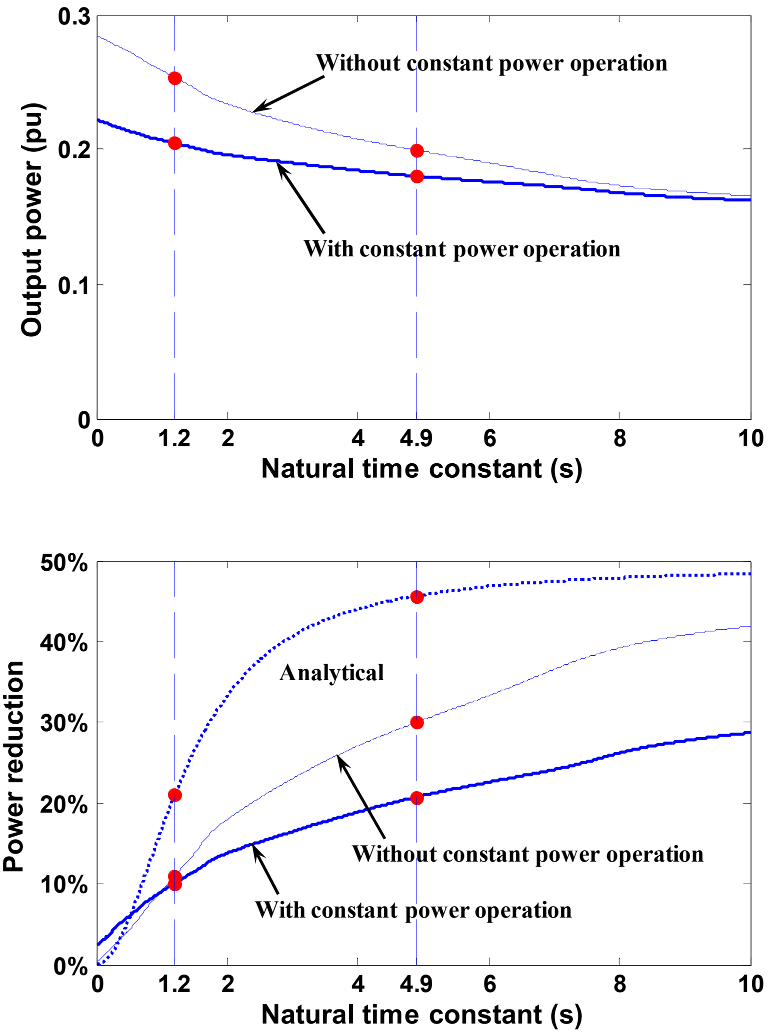

Fig. 6.12 The average output power versus natural time constant (upper) and the power reduction versus natural time constant (lower) based on wind data set 1.

It can be concluded that, a wind turbine with the constant power operation above the rated wind speed generates lower average output power but also produces a less power reduction in comparison with the case without the constant power operation.

6.5. Summary

In this chapter, real wind data is used to verify the analytical equations of the wind turbine power reduction with infinite and finite turbine inertia. Eight one-hour wind data sets are selected from the real wind data. The parameters of the eight data sets and the analytical power reduction are also provided in the chapter.

It was shown that the analytical power reduction with infinite turbine inertia calculated by the equation basically matches the simulation results. Furthermore, the simulations with finite turbine inertia show that no relationship exists in the graphs of the power reduction versus mean wind speed v_m and the power reduction versus wind speed variance σ^2. The numerical power reduction generated by the simulations is limited by the analytical power reduction with infinite inertia, and the power reduction versus σ^2/v_m^2 (squared TI) is close to a linear trend when σ^2/v_m^2 is relatively small, which matches the analysis based on the equation of the power reduction with infinite inertia. The simulated power reduction shows a good correlation with the analytical prediction but it is approximately half of the value. This is likely to be due to the non-linear effects of the wind turbine system. In addition, the power reduction versus power rating of the wind turbine shows the effects of wind speed characteristics on the power reduction for different sizes of wind turbines.

Finally, the effect of constant power operation on the average output power is analysed in this chapter. It was found that a wind turbine generates a less average output power but also produces a less dynamic power reduction with constant power operation compared to the case without constant power operation.

Chapter 7. Experimental Validation

7.1. Introduction

In this chapter, experimental hardware is used to provide some limited validation of the dynamic model of the wind turbine system which was used in the analysis of inertia effects on the dynamic performance of wind turbines in the previous few chapters. A vane anemometer and a cup anemometer are used to experimentally simulate a wind turbine operation under the no-load condition. The C_p characteristics of the rotor of the vane anemometer and the cup anemometer are assumed to be the same as the C_p characteristics of the American and the Savonius wind turbines respectively due to the physical similarity. The inertia of the rotors of the anemometers is calculated. Based on the estimated C_p characteristics and the calculated inertia, computer simulations are performed in the dynamic model of a wind turbine system under the no-load condition. The turbine speed response and the time constant which are predicted by the simulation in the wind turbine system model are compared with the measured results obtained from the tests.

7.2. Experimental Hardware

The experimental hardware is shown in Fig. 7.1, which consists of a fan to provide the wind, anemometers to simulate the turbine rotor, wind speed readouts to measure the wind speed, an oscilloscope to detect the sensor signals, and a data logger to record the frequency of the signal which is then scaled into the wind speed.

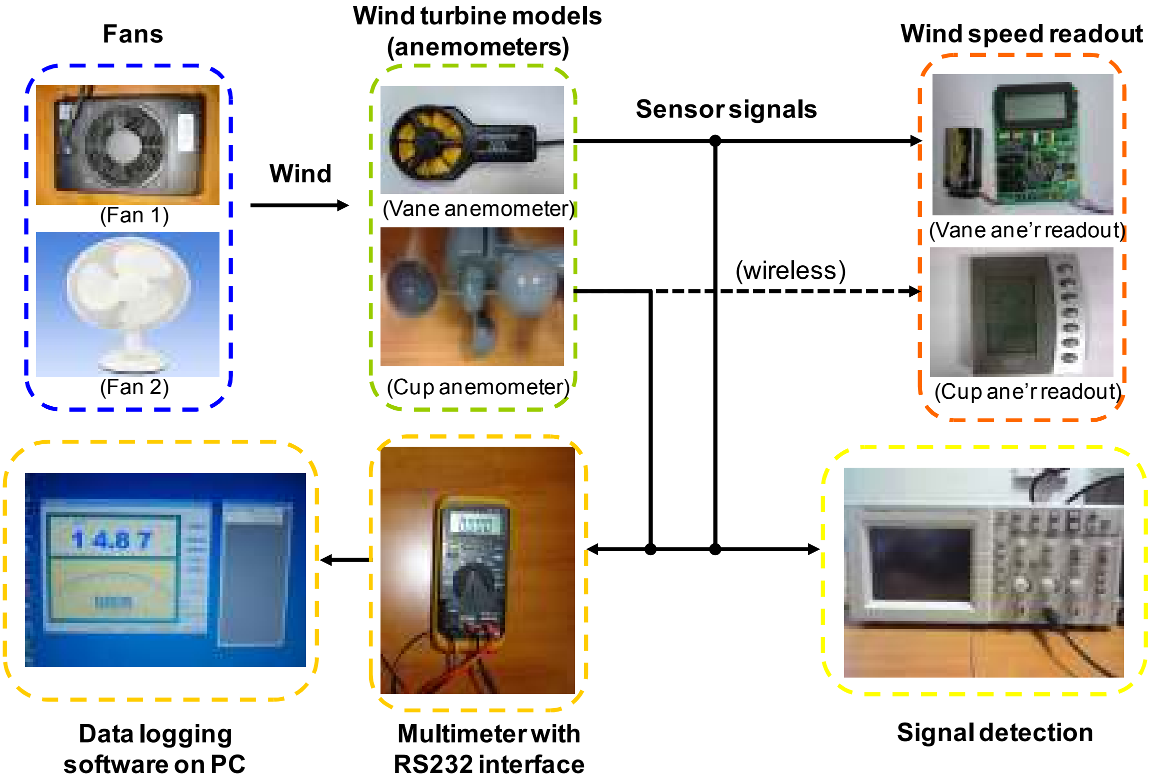

Fig. 7.1 The experimental hardware used to validate the dynamic model of the wind turbine system under the no-load condition

The two fans in Fig. 7.1 provide the wind speed ranges as shown in Table 7.1. Fan 1 rotates with a single speed and provides wind speeds ranging up to 2.8 m/s dependent on the distance between the fan and the sampling position. Fan 2 is able to provide the three different wind speeds with a maximum wind speed of 3.8 m/s.

Table 7.1 The wind speed ranges of the fans used in the experiments

Equipment	Wind Speed Range
Fan 1	0 - 2.8 m/s
Fan 2	0 - 3.8 m/s

A vane anemometer (TENMA 72-6638) with a horizontal-axis rotor which is physically similar to the American wind turbine in Fig. 7.5, and a cup anemometer (Bios wireless weather station CE1177) with a vertical-axis rotor which has a similar operation with the Savonius wind turbine in Fig. 7.1 are used in the tests. The specifications of the two anemometers are shown in Table 7.2.

Table 7.2 The parameters of the vane and cup anemometers

Anemometer	**Display Update Time**	**Range**	**Accuracy**
Vane	0.4 s	0.8 - 30.0 m/s	± (3%+2d)
Cup	128 s	1.3 - 27.8 m/s	± 4%

As given in Table 7.2, the display update time for the cup anemometer is significant longer than that of the vane anemometer. The long display interval of the cup anemometer aims to conserve the battery power, and is not adjustable.

A photo of the vane anemometer is given in Fig. 7.2 to show its construction, which consists of a sensor head with an eight-bladed rotor (Fig. 7.2 a) and data-acquisition board (Fig. 7.2 b). The principle is, when the wind flows through the sensor head, the rotor will rotate with a speed proportional to the wind speed ideally (the effect of the small rotor inertia on the wind speed reading is neglected). The vane anemometer also includes an optical sensor which generates a pulse signal with its frequency proportionally to the rotational speed. The frequency is read by the wind speed readout and is displayed on the LCD.

(a) The sensor head with an eight-bladed rotor (b) The wind speed readout

Fig. 7.2 Vane anemometer (TENMA 72-6638)

Note that, the acquisition board in Fig. 7.2 (b) was included in the vane anemometer originally, which physically connects with the sensor head in Fig. 7.2 (a).

The photo of the Bios wireless weather station and the dismantled three-cup anemometer is shown in Fig. 7.3 (a) and (b) respectively. The output signals from the cup anemometer are used for data logging.

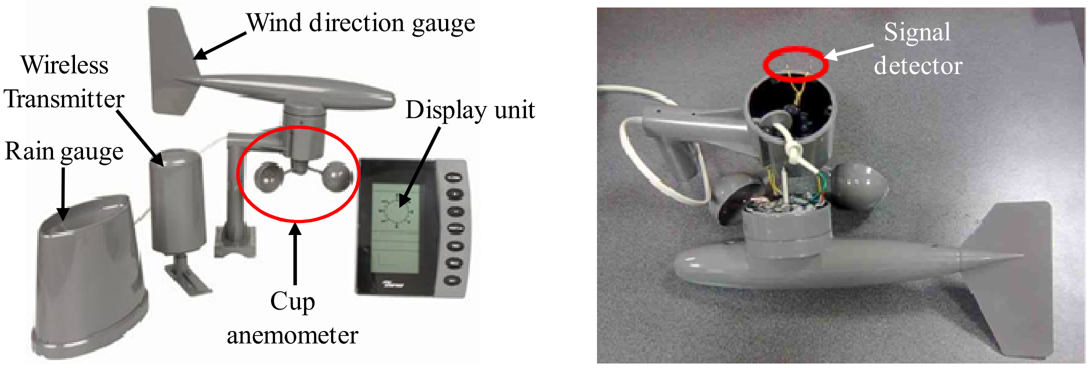

(a) Bios wireless weather station

(b) The dismantled cup anemometer

Fig. 7.3 Bios wireless weather station (a) and the dismantled cup anemometer (b)

The multimeter (QM1538 DIGITECH) is connected to the PC by a RS232 interface and is used to record the frequency of the sensor signal. This is proportional to the wind speed. The measurements are transferred to the PC and recorded by the software at time intervals of 1 second as shown in the data logging module in Fig. 7.1.

Moreover, the oscilloscope (Tektronix TDS1012) shown in the signal detection module in Fig. 7.1 is used to detect the waveform of the signal coming out of the sensors.

7.3. Vane Anemometer Test

7.3.1. Modelling of C_p Curve

The C_p characteristic of the rotor of the vane anemometer was modelled, which will be included in the dynamic model of the wind turbine system in Fig. 2.2. Firstly, the no-load TSR (at $C_p = 0$), is obtained from a test. In the test, Fan 1 was used to generate a wind speed which was assumed to be constant at each position in front of Fan 1. The vane anemometer was placed at two different positions and acquired two constant wind speeds of 0.5 m/s and 1 m/s. Since the vane anemometer was connected to an oscilloscope (see

Fig. 7.1), the signals from the vane anemometer are observed by two channels: Channels 1 and 2 as shown in Fig. 7.4.

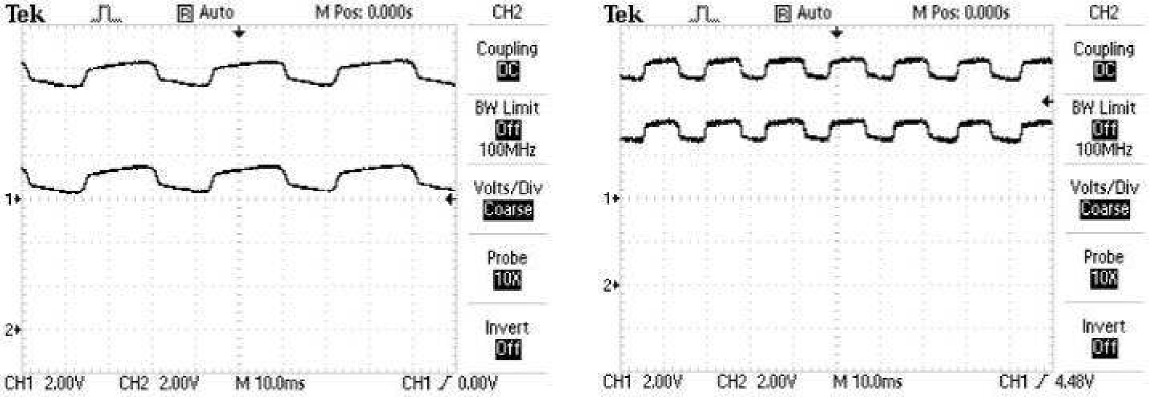

(a) wind speed of 0.5 m/s (b) wind speed of 1 m/s

Fig. 7.4 The vane anemometer pulse wave forms for two given wind speeds

Although it may be inaccurate to measure the wind speed under 0.8 m/s using the vane anemometer, the amplitude of the pulses is found to be constant under the two different wind speeds (0.5 m/s and 1 m/s), which corresponds to the frequencies 34 Hz and 68 Hz.

The frequency of the pulse signals detected by the optical sensor is expected to be eight times of the frequency of the rotor rotating due to its eight-blade construction. Therefore, the rotational speed in rad/s can be obtained as,

$$\omega = \frac{f}{8} \cdot 2\pi \tag{7.1}$$

The tip-speed ratio is constant when the rotor operates under the no-load condition (C_p=0). Therefore, the no-load TSR is found as,

$$\lambda_{Cp=0} = \frac{\omega R}{v} \tag{7.2}$$

The no-load TSR for the rotor of the vane anemometer is obtained as 1.923. Due to the presence of the bearing loss, the measured no-load TSR of the vane anemometer can not be obtained accurately under a zero power coefficient, which resulted in a small positive value.

Due to the physical similarity of the rotors of the vane anemometer under test and the American wind turbine in Fig. 7.5, it is assumed that the vane anemometer has a similar C_p characteristic as the eight-bladed design highlighted in the figure.

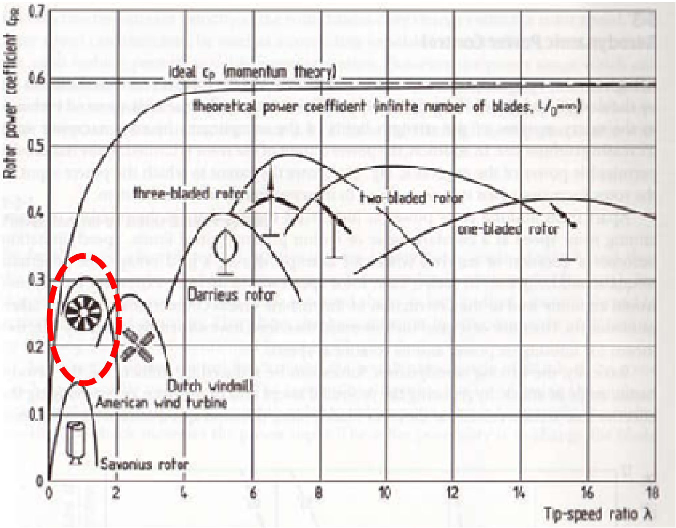

Fig. 7.5 The C_p characteristics of different wind turbine rotors [28]

In Fig. 7.5, the C_p curve of the eight-bladed design is approximately a parabola with a maximum power coefficient of 0.3 at the optimal TSR of 1. Moreover, the TSR at $C_p = 0$ is found to be approximately 2 which matches the test result. Therefore, the C_p curve of the vane anemometer is modelled by a quadratic equation given below,

$$C_p = (-0.3314)\times\lambda^2 + 0.6373\times\lambda \tag{7.3}$$

The Fig. 7.6 shows the C_p curve generated using Equation (7.3),

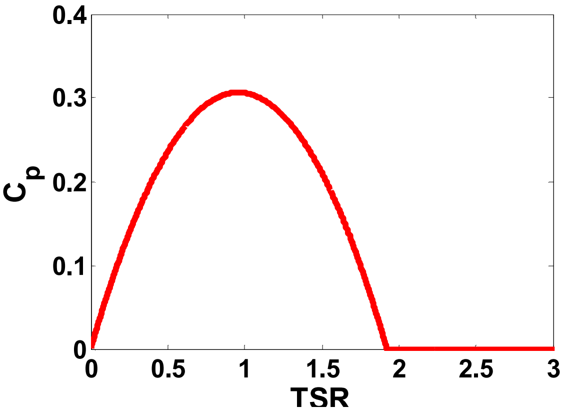

Fig. 7.6 The C_p characteristic of the rotor of the vane anemometer used in the modelling study

7.3.2. Modelling of Rotor Inertia

It was observed that the rotor blades of the vane anemometer under test has a small fixed pitch angle which can make the calculation of rotor inertia difficult. In order to reduce the complexity of calculation, the rotor blades are assumed to be straight. Then, the rotor of the vane anemometer can be approximated as a disk as shown in Fig. 7.7.

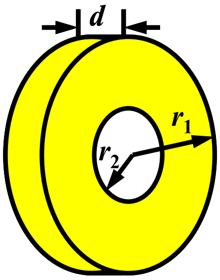

Fig. 7.7 Approximated profile of the rotor of the vane anemometer used in the inertia calculation

Where, the outer radius r_1 is 36 mm; the inner radius r_2 is 18 mm; the disk thickness d is 2 mm, which is the thickness of the real blades. Therefore, the inertia of the rotor can be obtained as,

$$J = \frac{1}{2}m\left(r_1^2 + r_2^2\right) = \frac{1}{2}\rho V\left(r_1^2 + r_2^2\right) \tag{7.4}$$

Note that, m in Equation (7.4) is the mass of disk. The densities of the plastic materials has been listed in the [38], with that most common plastics have a density between 0.97 and 1.25 g/cm^3. In the calculation of the plastic rotor, a density ρ of 1.11 g/cm^3 was used, which is the average value of this scale. The inertia J calculated by Equation (7.4) is 5.5×10^{-6} kg·m^2.

7.3.3. Simulation and Testing of Time Constant

Based on the estimated C_p characteristic and inertia of the rotor of the vane anemometer, the dynamic response of its speed is predicted by simulation using the dynamic model of a wind turbine system (see Fig. 2.2) under the no-load condition. It should be noted that the wind speed changes given in the simulation are from the measured values in the test. The simulated turbine speed responses are compared with the test results which are obtained in the experiment setup shown in Fig. 7.1.

In the test, Fan 2 is used to generate the wind speeds. A step increase in wind speed is obtained by quickly sliding the vane anemometer into the wind (see Fig. 7.8). In this test, the wind speed steps are obtained as 0-2.7 m/s and 0-1.3 m/s which were measured by the acquisition board in Fig. 7.2 (b). The frequency of the signals by the sensor head is recorded by the data logging module shown in Fig. 7.1, which is then used to calculate the rotational speed of the rotor by using Equation (7.1).

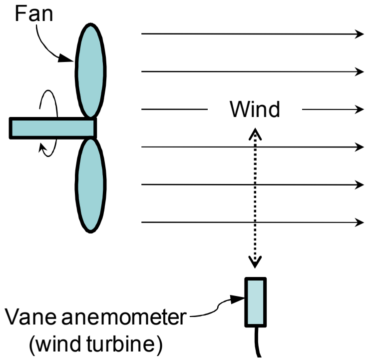

Fig. 7.8 Testing the step response of the vane anemometer

In Fig. 7.9, the turbine speed responses obtained from the simulations and the tests are compared, and the time constants obtained under the two different wind speed changes are also shown. It can be seen that the measured turbine speed responses match the simulation results obtained from the dynamic model of a wind turbine system under the no-load condition. Moreover, it was observed that when the wind speed is increased from 1.3 m/s to 2.7 m/s, the time constant is halved from 3.9 s to 1.9 s as expected. This result proves that the wind speed is inversely proportional to the turbine time constant.

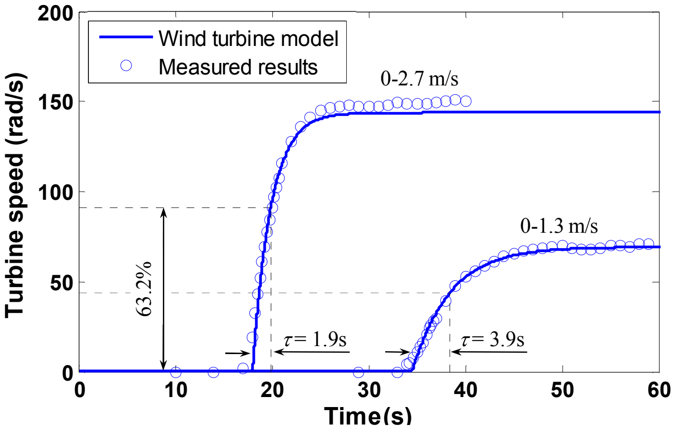

Fig. 7.9 Comparison of the measured and the simulated turbine speed responses for the vane anemometer indicating the simulated time constants only

In addition, the simulated time constant of the vane anemometer is shown in Fig. 7.10 for a step-change of 0 to *v* m/s.

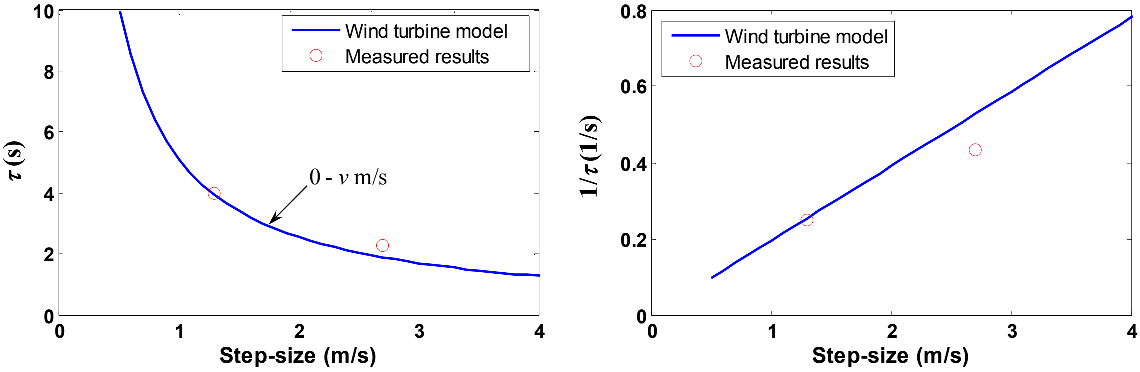

Fig. 7.10 The comparison of the predicted and the measured time constants for the vane anemometer

Fig. 7.10 shows the time constant predicted by the simulation basically matches the measurements from the tests. Furthermore, the simulation also shows that the time constant is inversely proportional to the wind speed step-size under the no-load condition.

7.4. Cup Anemometer Tests

7.4.1. Modelling of C_p Curve

In this section, the cup anemometer of the weather station is used to further verify the results obtained in the vane anemometer test. The C_p characteristic of the cup anemometer was modelled using the method described above for the anemometer test. The voltage signals generated by the cup anemometer sensor were obtained with and without the original readout circuit connected and are given in Fig. 7.11.

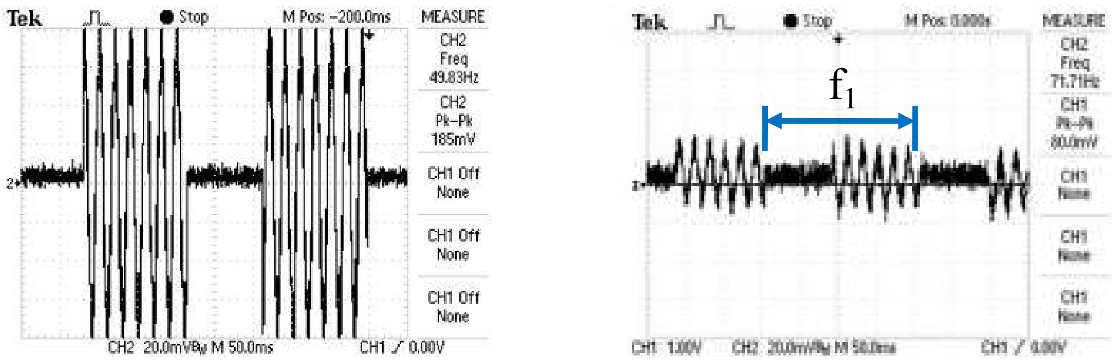

(a) Without the original circuit connected (b) With the original circuit connected

Fig. 7.11 The cup anemometer output signal without (a) and with (b) the original circuit connected

When the voltage signal is detected with the circuit connected Fig. 7.11 (b), the amplitude of voltage is reduced in comparison with the open-circuit voltage in Fig. 7.11 (a). The profile of the voltage signals in Fig. 7.11 are expected as due to the requirement of wireless transmission, such that the pulse signal generated by the cup anemometer is multiplied with a constant 50 Hz sinusoidal waveform as shown in Fig. 7.12.

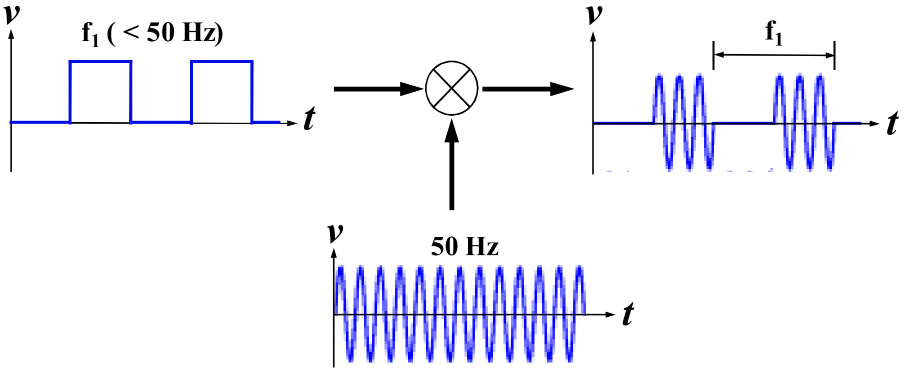

Fig. 7.12 The scheme of the derivation for the signal generated by the cup anemometer

As illustrated in Fig. 7.12, the pulse signal generated by the optical encoder has a frequency of f_1 that is directly proportional with the wind speed. The sinusoidal carrier signal maintains a constant frequency of 50 Hz. The measured signal is the product of the two waveforms as shown in Fig. 7.11. For a given wind speed, the no-load TSR is obtained by using Equation (7.2) where the rotational speed ω in rad/s can be calculated by,

$$\omega = 2\pi f_1 \tag{7.5}$$

where, f_1 is the frequency of the pulse signal generated by the cup anemometer. For example, using the signal Fig. 7.11 b measured at a wind speed of 3.5 m/s, the frequency f_1 is found 5 Hz. The no-load TSR for the cup anemometer is calculated as 0.65 that is about the one third of the no-load TSR for the vane anemometer which is 1.92.

The rotor of the cup anemometer is assumed to have a similar C_p characteristic as a vertical-axis wind turbine. In addition, the no-load TSR of the anemometer is approximated to the maximum power coefficient of the Savonius wind turbine which is 0.15 in Fig. 7.5. Similar to the vane anemometer, the C_p curve of the rotor of the cup anemometer is also modelled by a quadratic equation,

$$C_p = (-1.44)\times\lambda^2 + 0.929\times\lambda \tag{7.6}$$

Fig. 7.13 shows the C_p curves of the cup and vane anemometers which are generated using the corresponding quadratic equations, where the cup anemometer shows a much smaller maximum power coefficient and no-load TSR.

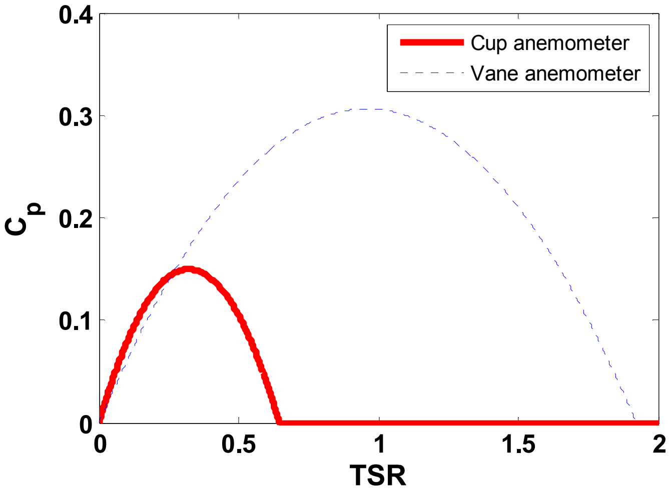

Fig. 7.13 The modelling of the C_p characteristic of the cup and vane anemometer

7.4.2. Modelling of Rotor Inertia

The top view of the rotor of the cup anemometer is shown in Fig. 7.14 (a). As illustrated, the rotor consists of three plastic hemispherical cups, which rotates anticlockwise with respect to the central axis *o*. The side view of a cup is shown in Fig. 7.14 (b).

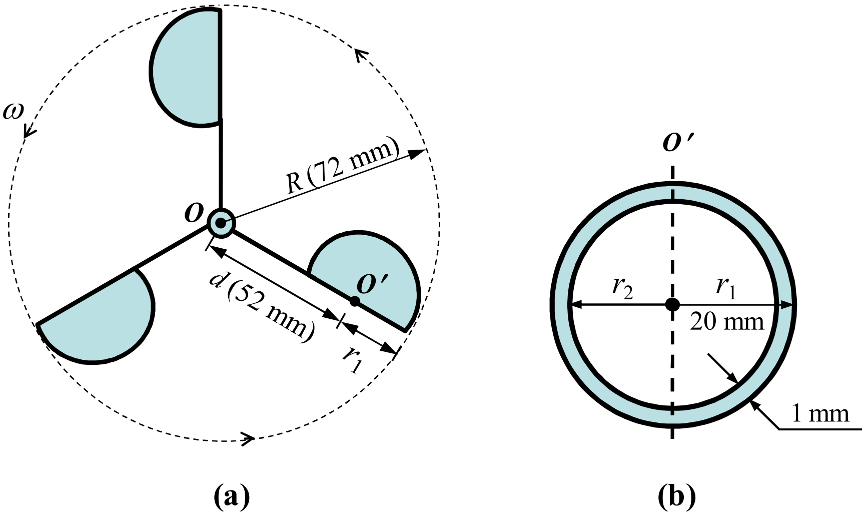

Fig. 7.14 The top view of the cup anemometer (a) and the front view of a cup (b)

The volume of a sphere is given by,

$$V_{sphere} = \frac{4}{3}\pi r^3 \tag{7.7}$$

where, r is the radius of the sphere. Therefore, the volume of each cup can be obtained by,

$$V_{cup} = \frac{2}{3}\pi(r_1^3 - r_2^3) \tag{7.8}$$

where, r_1 and r_2 are the outside and the inside radius of each cup. Then, the mass of each cup m_{cup} is given by,

$$m_{cup} = V_{cup} \cdot \rho \tag{7.9}$$

where, ρ is the density of the material (assumed to be 1.11 g/cm^3 for plastic). The inertia of a cup with respect to the axis o' in Fig. 7.14 (b) is given by,

$$J_{cup} = \frac{1}{2} \cdot \left(\frac{2}{5} m_1 r_1^2 - \frac{2}{5} m_2 r_2^2 \right) \tag{7.10}$$

where, m_1 is the mass of a solid plastic sphere with the radius r_1; m_2 is the mass of a solid plastic sphere with the radius r_2. Due to the fact that the inside radius r_2 of the cup is very close to the outside radius r_1, an approximation can be made as $r_1 = r_2$. Therefore, Equation (7.10) can be simplified as,

$$J_{cup} = \frac{1}{5} \cdot (m_1 - m_2) \cdot r_1^2 = \frac{2}{5} \cdot m_{cup} \cdot r_1^2 \tag{7.11}$$

The cup inertia with respect to the axis o' is then calculated as 4.24×10^{-7} kg·m^2. The cup inertia with respect to the central axis o of the rotor is then obtained by using the parallel-axis theorem (see Equation (3.11)), and hence the total inertia of the rotor is obtained as,

$$J_{rotor} = \frac{2}{5} \cdot m_{cup} \cdot r_1^2 + m_{cup} \cdot d^2 \tag{7.12}$$

where, d is the distance between the two axes o' and o. For the device under test, the inertia of a cup with respect to the axis o is calculated as 7.6×10^{-6} kg·m^2, and the total inertia is obtained as 2.28×10^{-5} kg·m^2 (J_{rotor} ×3). It can be seen that the inertia of the rotor of the cup anemometer is approximately four times larger than that of the vane anemometer which was 5.5×10^{-6} kg·m^2.

7.4.3. Simulation of Time Constant

Based on the estimated C_p characteristic and the inertia of the rotor of the cup anemometer, the turbine speed responses are simulated in the wind turbine system model under the no-load condition and two different step wind changes (Fig. 7.15). Note that the wind speed changes given in the figure are same as those presented in Fig. 7.9.

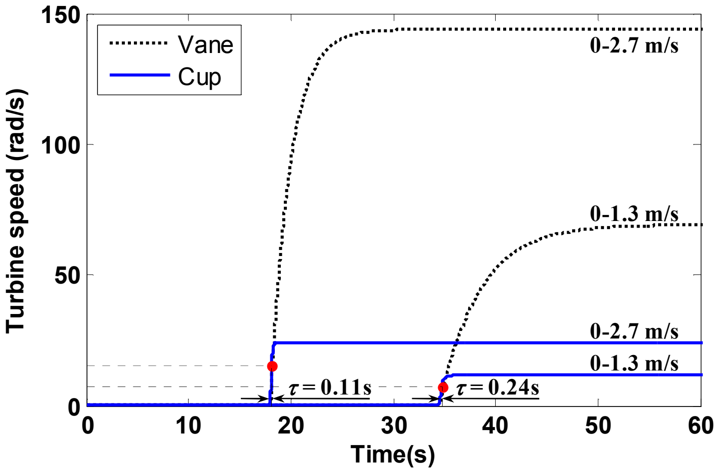

Fig. 7.15 The turbine speed responses predicted by the simulation for the cup anemometer

Fig. 7.15 shows that when the wind speed is increased from 1.3 m/s from 2.7 m/s (almost doubled), the time constant of the cup anemometer is halved from 0.24 s to 0.11 s. This also proves that wind speed is inversely proportional to the turbine time constant. Moreover, the cup anemometer has a much lower steady-state rotational speed (or turbine speed) which is due to the fact that it has a smaller no-load TSR (TSR at C_p= 0, see Fig. 7.13) and a larger rotor radius in comparison to the vane anemometer. The time constants of both anemometers are shown in Table 7.3.

Table 7.3 Comparison of the calculated time constants of the vane and cup anemometers

Rotor type	**Wind speed changes**	
	0-1.3 m/s	0-2.7 m/s
Vane	$\tau = 3.9$ s	$\tau = 1.9$ s
Cup	$\tau = 0.24$ s	$\tau = 0.11$ s

As given previously, the inertia of the cup anemometer is four times larger than the vane anemometer. However, since the rotor radius of the cup anemometer is two times larger than that of the vane anemometer, and as the turbine torque is proportional to the cube of the rotor radius according to Equation (2.2), then the turbine torque is an eight times larger. The increase in the turbine torque and the reduction in the turbine speed is much larger than the increase in the inertia, so that the time constant for the cup anemometer is much smaller than the vane anemometer.

Since the frequency of the voltage signal generated by the cup anemometer can not be directly detected by the multimeter of the data logging module (see Fig. 7.1), a circuit to do this will be constructed in a future study.

7.5. Summary

In this chapter, experimental tests are performed and provide limited validation of the dynamic model of a wind turbine system. An eight-bladed vane anemometer was used to simulate a horizontal-axis wind turbine operating under the no-load condition and a cup anemometer to simulate a vertical-axis wind turbine. The C_p characteristics of the rotors of the anemometers are modelled using the typical C_p characteristic of a physically similar wind turbine. The inertia of the turbine is calculated by using a simplified profile of the actual rotating parts.

Step increases in wind speed were used in the experiments, and the speed response of the vane anemometer was compared with the simulation results predicted by the dynamic model of the wind turbine system under the no-load condition, and showed a good match. This helps confirm the validity of the dynamic model which was used to investigate the power reduction due to the inertia effect in the previous chapters. Moreover, the turbine time constant being inversely proportional to the wind speed step sizes under the no-load condition was shown. From the comparison of the time constant for the vane and cup anemometers, it can be concluded that the turbine time constant is not only dependent on the inertia but also affected by the rotor radius and the turbine characteristics.

Chapter 8. Steady-State Parameter Sensitivity on MPPT

8.1. Introduction

For those MPPT control algorithms which are based on knowledge of the turbine characteristics, the turbine's characteristic curves can be obtained through experiments or modelling. Commonly, there is a discrepancy between the estimated curve which the MPPT controller uses and the actual turbine's characteristic curve. This generally causes the wind turbine to generate less power than if the MPPT controller used the actual turbine's characteristic curve, which has been indicated in the previous studies [40] [43].

Reference [40] demonstrates the error between the assumed optimal operating point and the actual operation point (see Fig. 8.1) based on optimal torque control, but the power reduction due to this error has not been further analysed or quantified.

NOTE:
This figure is included on page 94 of the print copy of
the thesis held in the University of Adelaide Library.

Fig. 8.1 Sub-optimal operation due to an inaccurate C_p-TSR Curve [40]

Reference [43] presents the calculated energy loss due to errors in the optimal TSR (λ_o) and maximum power coefficient (C_{pmax}) (see Fig. 8.2). The $C_p(\lambda)$ curve used in this reference paper is an idealised $C_p(\lambda)$ curve of the NREL variable-speed test-bed turbine. However, physical insight into how this power loss occurs has not been presented in [43].

NOTE:
This figure is included on page 94 of the print copy of
the thesis held in the University of Adelaide Library.

Fig. 8.2 The calculated power loss due to the errors in the C_{pmax} and λ_o values [43]

This chapter will present the physical understanding of how the parameter errors affect the output power under MPPT control. Also, the power reduction due to parameter errors is quantified for two different MPPT control strategies: constant TSR control and optimal torque control.

A computer simulation study has been done in MATLAB to investigate the power reduction utilizing two different MPPT control algorithms. In this steady-state study of the parameter sensitivity, the dynamic response due to the turbine inertia was neglected and the generator torque (T_g) was assumed to be equal to the turbine torque, T_t (see Fig. 8.3 for the optimal torque control strategy).

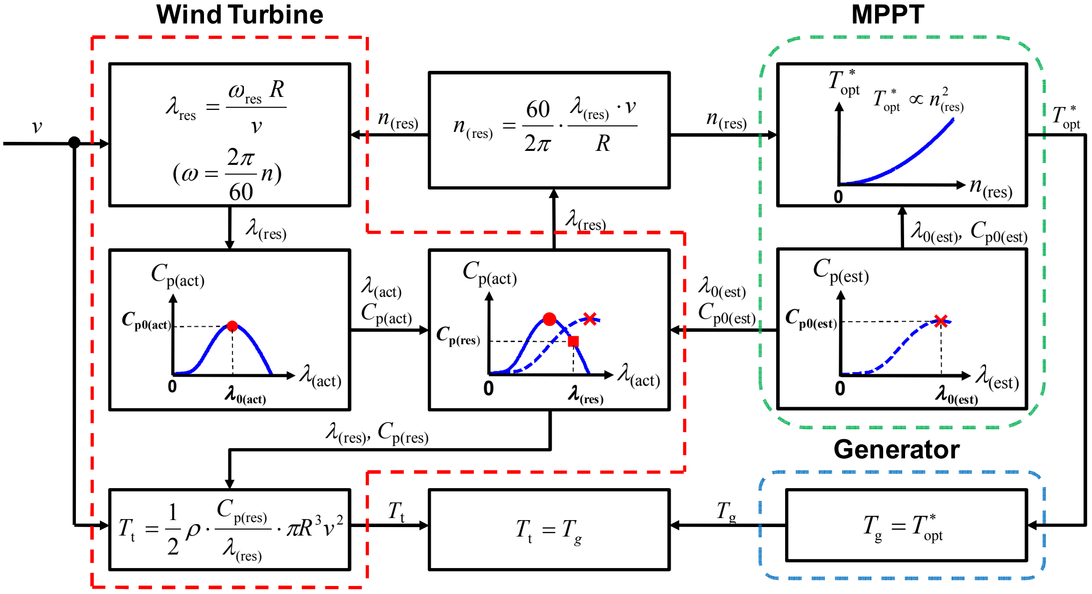

Fig. 8.3 A steady-state model of a wind turbine system for the analysis of the parameter sensitivity on the performance of the optimal torque control

In Fig. 8.3, the estimated C_p curve ($C_{p(est)}$ versus $\lambda_{(est)}$ curve) used in the MPPT algorithm is usually obtained from experiments and generally shows some discrepancy in comparison to the actual C_p curve ($C_{p(act)}$ versus $\lambda_{(act)}$ curve) of the wind turbine. For instance when using optimal torque control (OTC), due to the presence of this discrepancy, the torque signal T^*_{opt} generated by the controller is not equal to the actual optimal torque (the value of turbine torque corresponding to the actual maximum power point), which causes the resultant tip-speed ratio $\lambda_{(res)}$ to be different than the actual optimal *TSR* $\lambda_{0(act)}$ of the wind turbine. Therefore, the corresponding resultant power coefficient $C_{p(res)}$ is smaller than the actual maximum power coefficient $C_{p0(act)}$, which results in the output power reduction. In this chapter, a physical understanding and estimation of the power reduction caused by the discrepancy of the estimated turbine characteristics will be provided by simulation which is based on the two MPPT control algorithms, constant TSR control (CTC) and optimal torque control.

8.2. Constant TSR Control (CTC) Strategy

Due to the fact that the shape of the actual C_p curve affects the power reduction caused by the parameter errors (detailed explanations will be provided in the following subsections), an important assumption was made in this analysis. This assumption is that the actual C_p curve used in this chapter is the same as the one used previously in Equation (2.5). The shape of the example actual C_p curve is shown below in Fig. 8.4.

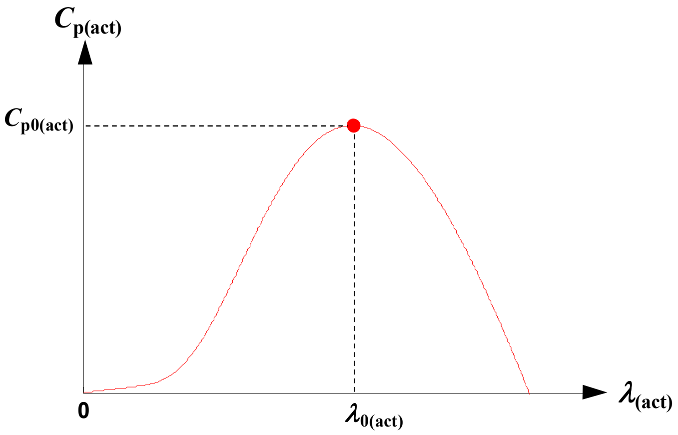

Fig. 8.4 The example actual C_p curve

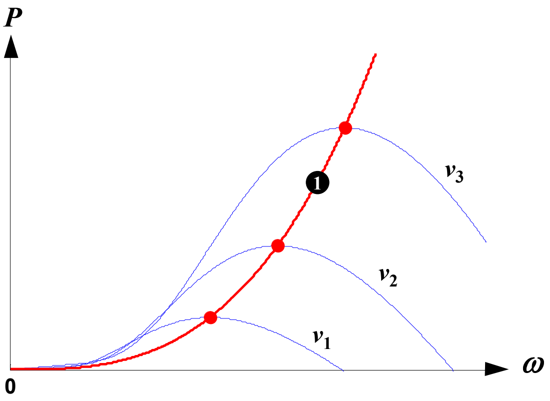

Fig. 8.5 Power versus angular speed based on the example actual C_p characteristic. Curve 1: the actual maximum power locus

In order to achieve the maximum output power, the MPPT should be used to maintain the tip-speed ratio at the actual optimal value $\lambda_{0(act)}$ which corresponds to the actual maximum power coefficient $C_{p0(act)}$ in Fig. 8.4. Therefore, the output power of the wind turbine will follow the actual maximum power locus - Curve 1 in Fig. 8.5. However, the wind turbine does not operate along the actual maximum power locus if there are errors in the estimated C_p curve. In this section, the CTC strategy is utilised to analyse the sensitivity of errors in the estimated optimal values of the turbine characteristic ($\lambda_{0(est)}$ and $C_{p0(est)}$) on the power output.

For the CTC strategy, the controller computes the optimal turbine speed according to the wind speed measured by an anemometer and knowledge of the estimated optimal TSR ($\lambda_{0(est)}$). It is assumed that the shape of the actual C_p curve is known as that in Fig. 8.4 (the same curve is also shown as Curve 3 in Fig. 8.6). Two cases are considered: an error in $\lambda_{0(est)}$ while assuming $C_{p0(est)}$ is correct ($C_{p0(est)}=C_{p0(act)}$), and an error in $C_{p0(est)}$ while assuming $\lambda_{0(est)}$ correct ($\lambda_{0(est)}=\lambda_{0(act)}$). The first case is shown in Fig. 8.6, where the actual C_p curve is noted as Curve 3 and two estimated C_p curves with the errors in $\lambda_{0(est)}$ are noted as Curve 1 and 2.

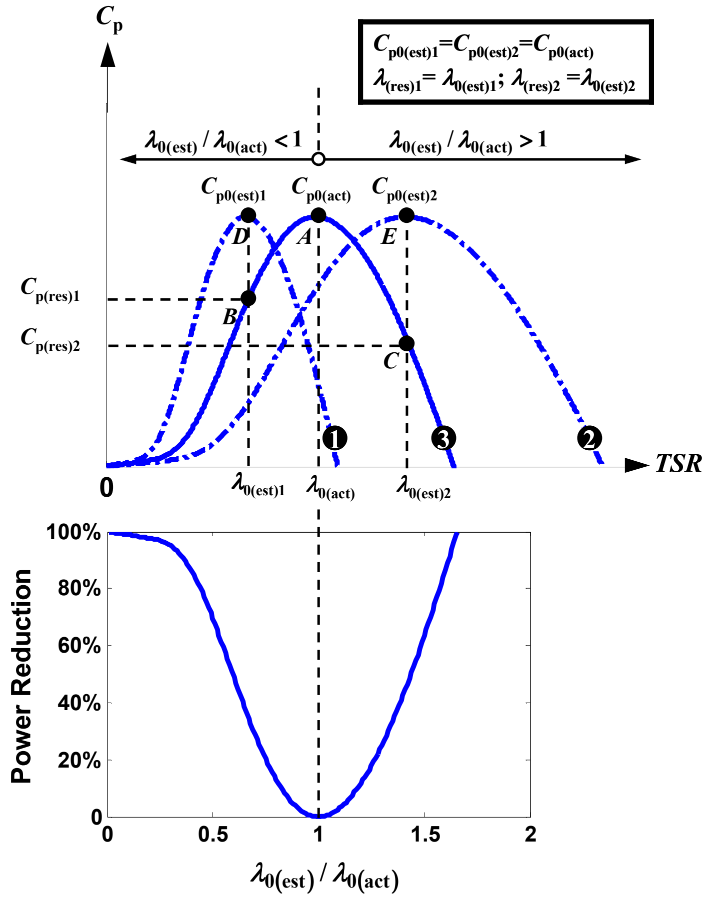

Fig. 8.6 The power reduction versus the ratio $\lambda_{0(est)}/\lambda_{0(act)}$ based on the example C_p curves: Curves 1 and 2: estimated C_p curves; Curve 3: actual C_p curve

Note that, $\lambda_{0(est)}/\lambda_{0(act)}$ in Fig. 8.6 is the estimated optimal TSR as a ratio of the actual optimal TSR rather than an ratio of "error" in $\lambda_{0(est)}$. When the estimated optimal TSR

$\lambda_{0(\mathrm{est})1}$ is smaller than the actual optimal TSR $\lambda_{0(\mathrm{act})}$, the wind turbine operates with the resultant TSR $\lambda_{(\mathrm{res})1}$ ($\lambda_{(\mathrm{res})1}=\lambda_{0(\mathrm{est})1}$) at point *B* with a power coefficient $C_{\mathrm{p(res)1}}$ rather than the actual maximum power coefficient $C_{\mathrm{p0(act)}}$ of point *A*. It is similar when the estimated optimal TSR $\lambda_{0(\mathrm{est})2}$ is greater than the actual optimal TSR $\lambda_{0(\mathrm{act})}$, where the wind turbine actually operates with the resultant power coefficient $C_{\mathrm{p(res)2}}$ and TSR $\lambda_{(\mathrm{res})2}$ ($\lambda_{(\mathrm{res})2}=\lambda_{0(\mathrm{est})2}$) at point *C*, and again $C_{\mathrm{p(res)2}} < C_{\mathrm{p0(act)}}$. The power reduction is caused by the difference between the actual maximum power coefficient $C_{\mathrm{p0(act)}}$ and the resultant power coefficients ($C_{\mathrm{p(res)1}}$ and $C_{\mathrm{p(res)2}}$). The power reduction can be calculated by Equation (8.1).

$$
\begin{aligned}
P_{\mathrm{reduction}} &= \frac{P_{0(\mathrm{act})} - P_{(\mathrm{res})}}{P_{0(\mathrm{act})}} \\
&= \frac{\frac{1}{2}\cdot C_{\mathrm{p0(act)}}\cdot\rho\cdot\pi\cdot R^2\cdot v^3 - \frac{1}{2}\cdot C_{\mathrm{p(res)}}\cdot\rho\cdot\pi\cdot R^2\cdot v^3}{\frac{1}{2}\cdot C_{\mathrm{p0(act)}}\cdot\rho\cdot\pi\cdot R^2\cdot v^3} \\
&= \frac{C_{\mathrm{p0(act)}} - C_{\mathrm{p(res)}}}{C_{\mathrm{p0(act)}}}
\end{aligned}
\tag{8.1}
$$

In Equation (8.1), the power reduction linearly correlates to the resultant power coefficient $C_{\mathrm{p(res)}}$ which corresponds to moving on the actual C_{p} curve according to the estimated optimal TSR $\lambda_{0(\mathrm{est})}$. Thus the shape of the power reduction versus the ratio $\lambda_{0(\mathrm{est})}/\lambda_{0(\mathrm{act})}$ is the same as the actual C_{p} curve as shown in Fig. 8.6. When the estimated optimal TSR exactly matches the actual optimal TSR at point *A*, the power reduction is zero.

If the error in $\lambda_{0(\mathrm{est})}$ is given as $(\lambda_{0(\mathrm{act})}-\lambda_{0(\mathrm{est})})/\lambda_{0(\mathrm{act})}$, it can be seen from Fig. 8.6 that the power reduction is not sensitive to small errors in $\lambda_{0(\mathrm{est})}$ for instance, ±10% of the errors in $\lambda_{0(\mathrm{est})}$ result in up to 4% power reduction in Fig. 8.6. This is due to the fact that the top of the example actual C_{p} curve is relatively flat as shown in Fig. 8.6. In comparison, larger errors in $\lambda_{0(\mathrm{est})}$ (±40%) can cause a significant power reduction (> 50%).

The second case is considered as the errors occur in $C_{\mathrm{p0(est)}}$ with an assumption that $\lambda_{0(\mathrm{est})}$ is correct ($\lambda_{0(\mathrm{est})}=\lambda_{0(\mathrm{act})}$). In Fig. 8.7, the actual C_{p} curve is noted as Curve 3 and two estimated C_{p} curves with the errors in $C_{\mathrm{p0(est)}}$ are noted as Curves 1 and 2 respectively.

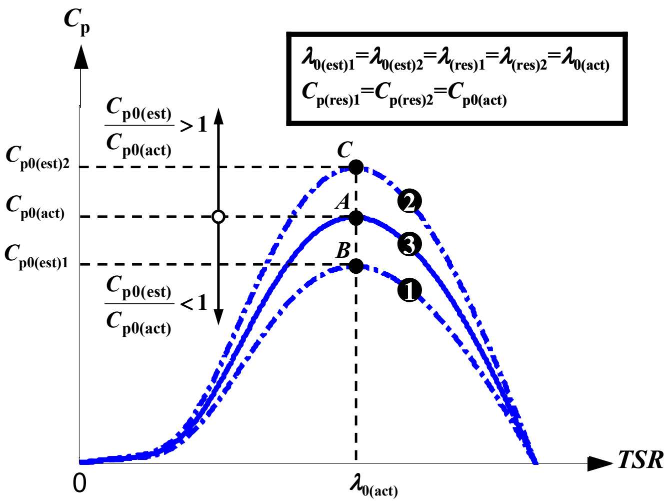

Fig. 8.7 The C_p versus TSR characteristics. Curves 1 and 2: estimated C_p curves; Curve 3: actual C_p curve

Due to the fact that the estimated optimal TSR $\lambda_{0(est)}$ is only used in the CTC control, no power reduction occurs ($P_{reduction}= 0$) assuming that there is no errors in the estimated optimal TSR $\lambda_{0(est)}$ ($\lambda_{0(est)1}=\lambda_{0(est)2}=\lambda_{0(act)}$) as shown in Fig. 8.7. Therefore, the wind turbine operates at a resultant power coefficient which is equal to the actual maximum power coefficient, that is $C_{p(res)1}= C_{p(res)2}=C_{p0(act)}$ at point A in Fig. 8.7.

The power reduction is a function of the ratio of estimated to actual optimal TSR ($\lambda_{0(est)}/\lambda_{0(act)}$) and the ratio of estimated to actual maximum C_p ($C_{p0(est)}/C_{p0(act)}$). A contour plot of power reduction versus the two ratios is shown in Fig. 8.8, which is then normalized to show the parameter sensitivity on power reduction in Fig. 9.

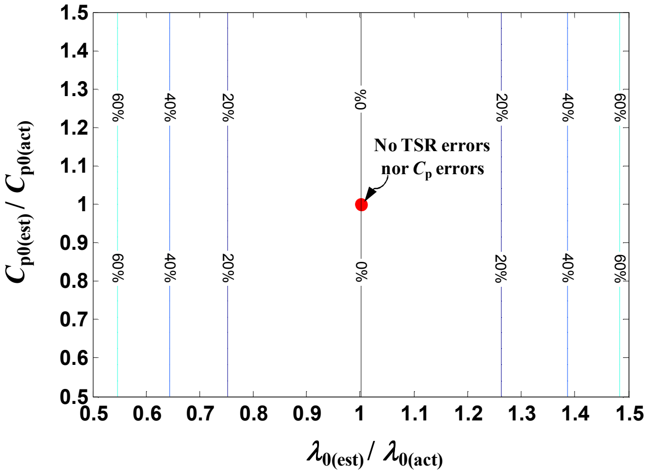

Fig. 8.8 The contour plot of the power reduction with the changes of $C_{p0(est)}/C_{p0(act)}$ vs. $\lambda_{0(est)}/\lambda_{0(act)}$ for the CTC strategy

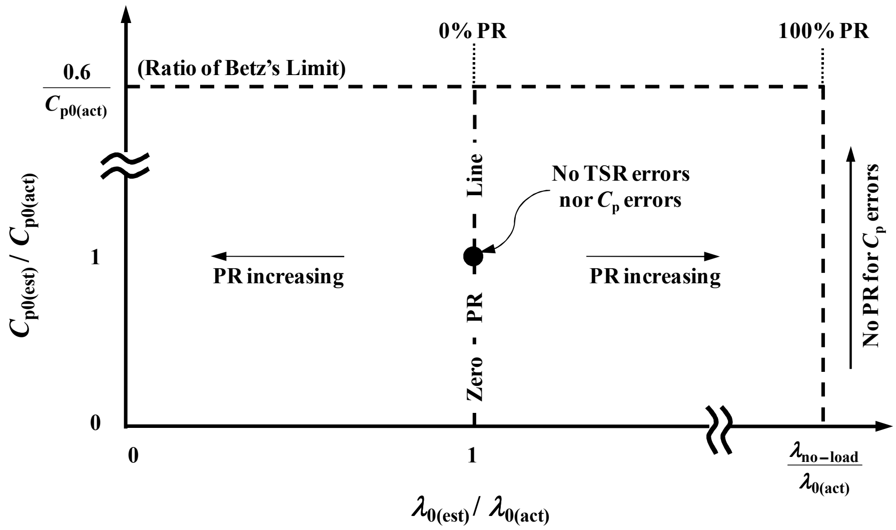

Fig. 8.9 The parameter sensitivity on power reduction for the CTC strategy

As shown in Fig. 8.8 and Fig. 8.9, the power reduction changes with the ratio of $\lambda_{0(\mathrm{est})}/\lambda_{0(\mathrm{act})}$ only but it is independent of the ratio of $C_{\mathrm{p0(est)}}/C_{\mathrm{p0(act)}}$ for the CTC strategy. The zero-power-reduction line is where the $\lambda_{0(\mathrm{est})}/\lambda_{0(\mathrm{act})}$ ratio is equal to 1. Moreover, the $C_{\mathrm{p0(est)}}$ / $C_{\mathrm{p0(act)}}$ ratio is limited by the ratio of Betz's limit, 0.6/ $C_{\mathrm{p0(act)}}$. A 100% power reduction occurs when the $\lambda_{0(\mathrm{est})}/\lambda_{0(\mathrm{act})}$ ratio is equal to $\lambda_{\text{no-load}}/\lambda_{0(\mathrm{act})}$ ($\lambda_{\text{no-load}}$ is the TSR at zero C_{p}).

In summary, for the CTC strategy, the power reduction due to the error of the estimated C_{p} curve depends on the ratio $\lambda_{0(\mathrm{est})}$ / $\lambda_{0(\mathrm{act})}$, which denotes the accuracy of the estimated optimal TSR. The sensitivity of the ratio $\lambda_{0(\mathrm{est})}$ / $\lambda_{0(\mathrm{act})}$ to the power reduction depends on the shape of the actual C_{p} curve. Errors in the knowledge of the maximum C_{p} value have no effect on the power reduction.

8.3. Optimal Torque Control (OTC) Strategy

In the OTC strategy, the generator torque is controlled to an optimal value T_{opt} according to the turbine speed ω using Equation (8.2),

$$T_{opt} = k_0 \cdot \omega^2 \tag{8.2}$$

The constant k_0 in this equation is computed based on the knowledge of the optimal TSR λ_0 and the maximum power coefficient C_{p0}, and is given by

$$k_0 = \frac{1}{2}\rho A R^3 \cdot \frac{C_{p0}}{\lambda_0^3} \tag{8.3}$$

Hence, the maximum output power P_0 of the turbine and thus the generator is obtained as

$$P_0 = k_0 \cdot \omega^3 \tag{8.4}$$

According to Equations (8.3) and (8.4), the OTC strategy depends on the knowledge of the two turbine parameters, C_{p0} and λ_0, and the turbine speed ω. The CTC strategy only requires the knowledge of the optimal TSR λ_0 but does require wind speed information which is much more difficult to obtain than turbine speed.

Due to experimental discrepancies, the estimated C_p curve is usually different from the actual C_p curve as is shown in Fig. 8.10 (a) and (b), where the circle denotes the actual optimal TSR and the actual maximum C_p, the cross denotes the estimated optimal TSR and the estimated maximum C_p, and the square represents the resultant TSR and the resultant C_p. Here, TSR and C_p errors have been introduced, which are shown in (a) and (b) in Fig. 8.10 respectively.

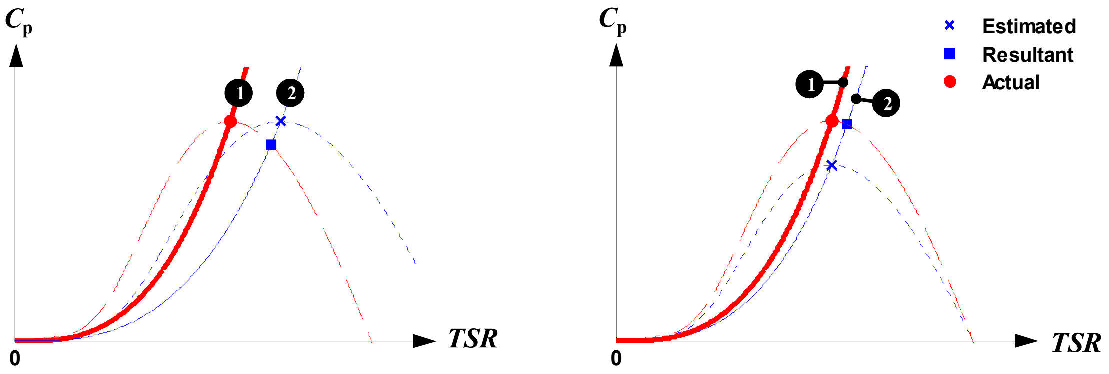

(a) With *TSR* error

(b) With C_p error

Fig. 8.10 An example discrepancy in the C_p vs. *TSR* characteristic with the dashed lines: the actual C_p characteristic; the dotted lines: the estimated C_p characteristic; Curve 1: the actual optimal C_p locus; Curve 2: the estimated equivalent optimal C_p locus.

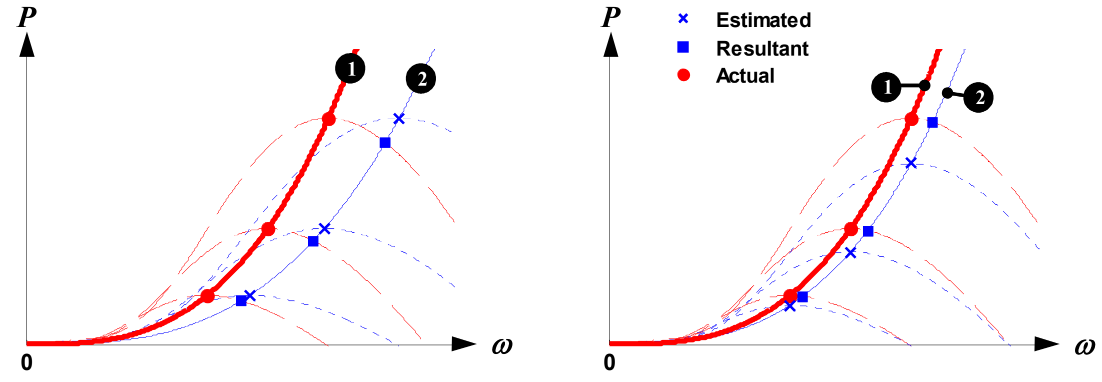

(a) With *TSR* error

(b) With C_p error

Fig. 8.11 Power versus turbine speed. Curve 1: the actual maximum power locus; Curve 2: the estimated maximum power locus; the dashed lines: the actual P versus ω correlating to the actual C_p; the dotted lines: the estimated P versus ω correlating to the estimated C_p.

The error of TSR and C_p in Fig. 8.10 then causes the difference between the actual, estimated and resultant operating points in Fig. 8.11 (a) and (b). The actual maximum power points are on the actual optimal power locus (Curve 1), while the estimated maximum power points and the resultant power points are both on the estimated optimal power locus (Curve 2). The latter two points correspond to the intercepts with the different P versus ω curves - the actual (dashed lines) and the estimated (dotted lines) respectively. The resultant power points are always lower than the actual maximum power point.

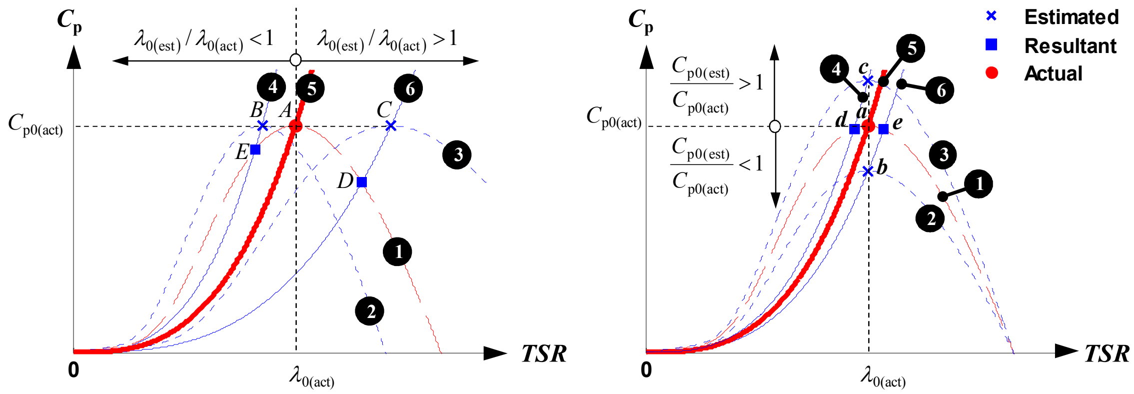

(a) With TSR error

(b) With C_p error

Fig. 8.12 The example actual C_p curve and estimated C_p curves: Curve 1: the actual C_p curve; Curve 2 and 3: the estimated C_p Curves; Curve 4 and 6: the estimated equivalent optimal C_p loci; Curve 5: the actual equivalent optimal C_p locus.

Fig. 8.12 is an extended version of Fig. 8.10 showing the actual C_p curve (Curve 1) and two estimated curves (Curves 2 and 3) for the TSR error case (a) and the C_p error case (b). The points A and a are the actual maximum power coefficient points ($\lambda_{0(act)}$, $C_{p0(act)}$), while the points B, C, b and c are the estimated maximum power coefficient points, ($\lambda_{0(est)1}$, $C_{p0(est)1}$) and ($\lambda_{0(est)2}$, $C_{p0(est)2}$). The points D, E, d and e are the resultant power coefficient points, ($\lambda_{(res)1}$, $C_{p(res)1}$) and ($\lambda_{(res)2}$, $C_{p(res)2}$). The errors in $\lambda_{0(est)}$ (shown in Fig. 8.12 a) and the errors in $C_{p0(est)}$ (shown in Fig. 8.12 b) cause the difference between the actual maximum power points and the resultant output power points, which are shown in Fig. 8.13 (a) and (b) respectively.

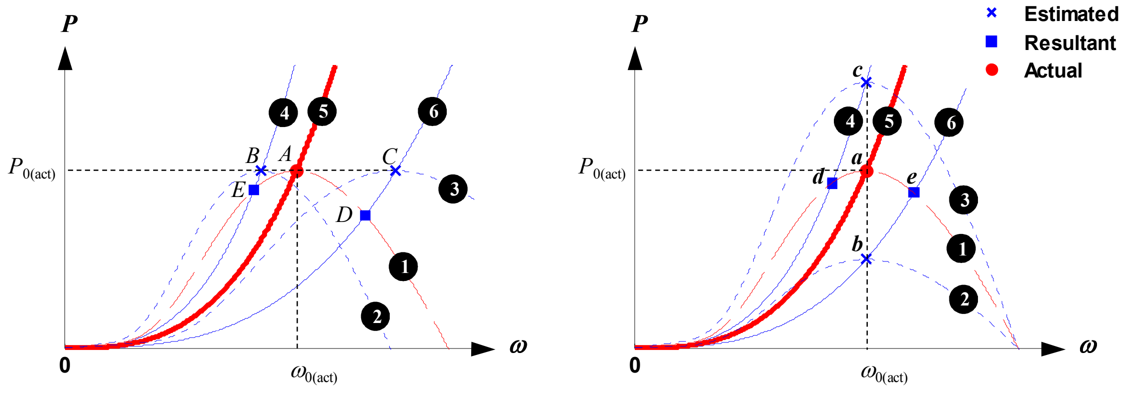

(a) With TSR error

(b) With C_p error

Fig. 8.13 Power versus turbine speed with: Curve 1: the actual P vs. ω based on the actual C_p curve. Curve 2 and 3: the estimated P vs. ω based on the estimated C_p curves. Curve 5: the actual maximum power locus; Curve 4 and 6: the estimated maximum power loci;

In Fig. 8.13 (a), the intercepts of the estimated maximum power loci and the estimated P versus ω (Curves 2 and 3) refers to the estimated optimal turbine speed $\omega_{0(est)}$ ($\omega_{0(est)1}$ for point B and $\omega_{0(est)2}$ for point C) and the estimated maximum output power $P_{0(est)}$ ($P_{0(est)1}$ for point B and $P_{0(est)2}$ for point C) while the intercepts of the actual maximum power locus and the actual P versus ω refers to the actual optimal turbine speed $\omega_{0(act)}$ and the actual maximum output power $P_{0(act)}$ at the point A. In comparison, the intercepts of the estimated maximum power loci (Curves 4 and 6) and the actual P versus ω (Curve 5) refers to the resultant turbine speed $\omega_{(res)}$ ($\omega_{(res)1}$ for point E and $\omega_{(res)2}$ for point D) and the resultant output power $P_{(res)}$ ($P_{(res)1}$ for point E and $P_{(res)2}$ for point D) in Fig. 8.13 (a). The situation is similar for the case with the C_p error in Fig. 8.13 (b).

When a wind turbine is controlled by the OTC strategy, both the estimated and the resultant operating points are located on the estimated maximum power locus (see Fig. 8.13). Therefore, the constant k_0 (see Equation (8.3)) is the same for the estimated and the resultant cases, that is,

$$\frac{C_{\mathrm{p0(est)}}}{\lambda^3_{\mathrm{0(est)}}} = \frac{C_{\mathrm{p(res)}}}{\lambda^3_{\mathrm{(res)}}} \tag{8.5}$$

Hence, the estimated equivalent optimal C_p loci in Fig. 8.12 (Curves 4 and 6) are given by,

$$C_\mathrm{p}(\lambda) = \frac{C_{\mathrm{p0(est)}}}{\lambda^3_{\mathrm{0(est)}}} \cdot \lambda^3 \tag{8.6}$$

When the estimated equivalent optimal C_p locus intercepts the actual C_p curve, λ is equal to $\lambda_{\mathrm{(res)}}$ and C_p is equal to $C_{\mathrm{p(res)}}$. The estimated equivalent optimal C_p loci correspond to the estimated maximum power loci in Fig. 8.13 (Curves 4 and 6) with the resultant power coefficient $C_{\mathrm{p(res)}}$ equivalent to the resultant output power $P_{\mathrm{(res)}}$ and the resultant TSR $\lambda_{\mathrm{(res)}}$ equivalent to the resultant turbine speed $\omega_{\mathrm{(res)}}$.

Combining Equations (8.6) and (8.1), the power reduction due to the TSR error can be given by

$$P_{\mathrm{reduction}} = 1 - \frac{C_{\mathrm{p0(est)}}}{C_{\mathrm{p0(act)}}} \cdot \frac{\lambda^3_{\mathrm{(res)}}}{\lambda^3_{\mathrm{0(est)}}} \tag{8.7}$$

For the case with “TSR error only”, where $C_{\mathrm{p0(est)}} = C_{\mathrm{p0(act)}}$, the power reduction can be simplified as,

$$P_{\mathrm{reduction}} = 1 - \frac{\lambda^3_{\mathrm{(res)}}}{\lambda^3_{\mathrm{0(est)}}} \tag{8.8}$$

As illustrated in Equations (8.7) and (8.8), the power reduction is caused by the difference in the estimated and the actual parameter k_0 (see Equation (8.3)). Zero power reduction occurs when the following relationship is satisfied,

$$\frac{C_{\mathrm{p0(est)}}}{\lambda^3_{\mathrm{0(est)}}} = \frac{C_{\mathrm{p0(act)}}}{\lambda^3_{\mathrm{0(act)}}} \tag{8.9}$$

Fig. 8.14 shows similar C_p versus TSR graphs to those shown in Fig. 8.10 except for a range of C_{p0} and λ_0 errors.

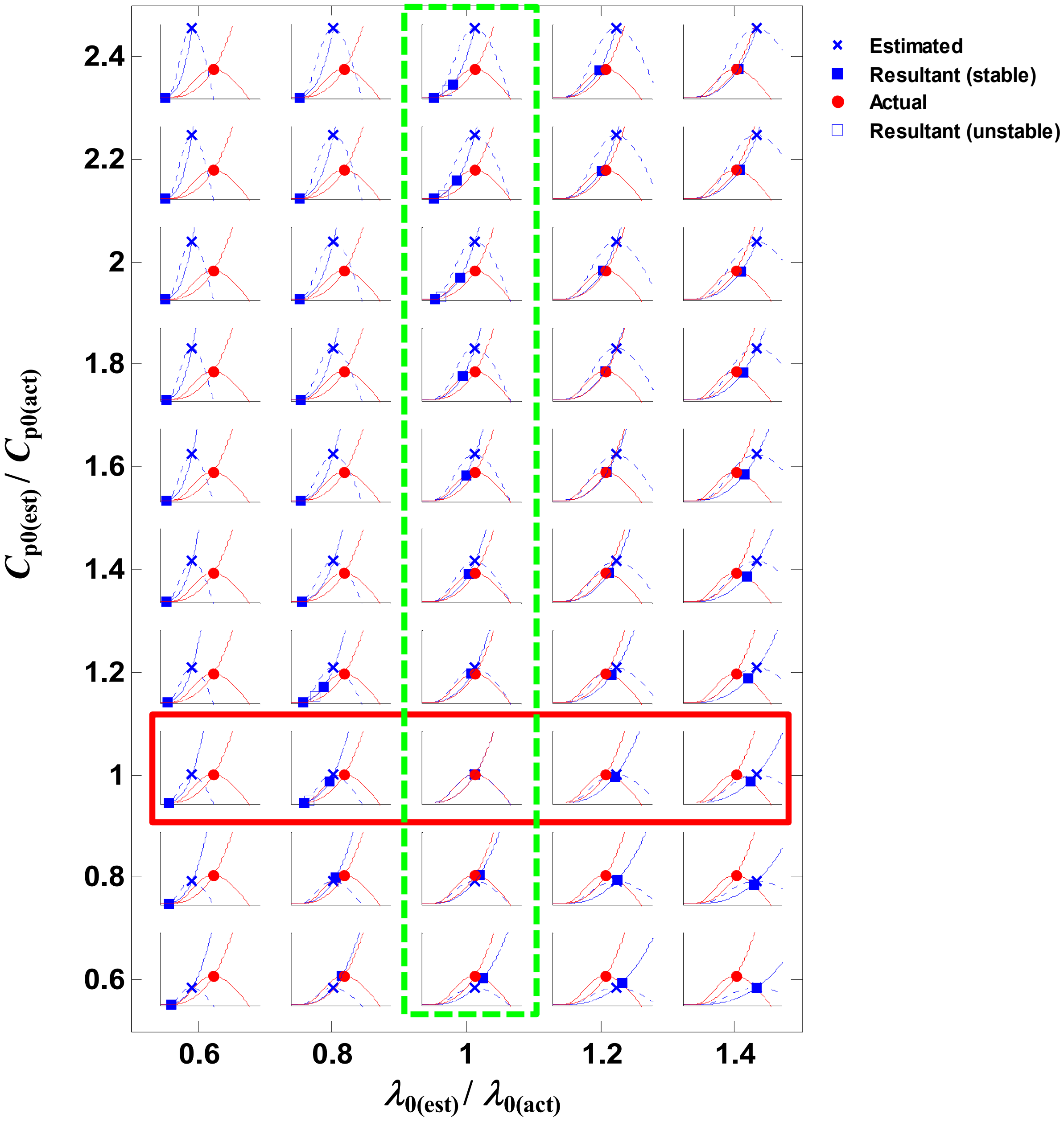

Fig. 8.14 C_p versus TSR curves as a function of $C_{p0(est)}/C_{p0(act)}$ and $\lambda_{0(est)}/\lambda_{o0(act)}$. Each graph shows the C_p curves: actual (solid line) and estimated (dashed line) along with the equivalent optimal C_p loci and maximum power points: actual (circles) and estimated (crosses) maximum power coefficient points and the resultant operating point (squares).

As can be seen in Fig. 8.14, there are some cases with three intercepts between the actual C_p characteristic and the estimated equivalent optimal C_p locus. Two intercepts are stable operation points (solid squares) and the one in between is an unstable operation point (empty squares). The actual maximum power point is denoted with circles in Fig. 8.14.

The variation of $\lambda_{(res)}$ and $C_{p(res)}$ with $\lambda_{0(est)}$ for the case with "TSR error only" can be seen in Fig. 8.15, and the changes of $C_{p(res)}$ with $C_{p0(est)}$ for the case with "C_p error only" in Fig. 8.16.

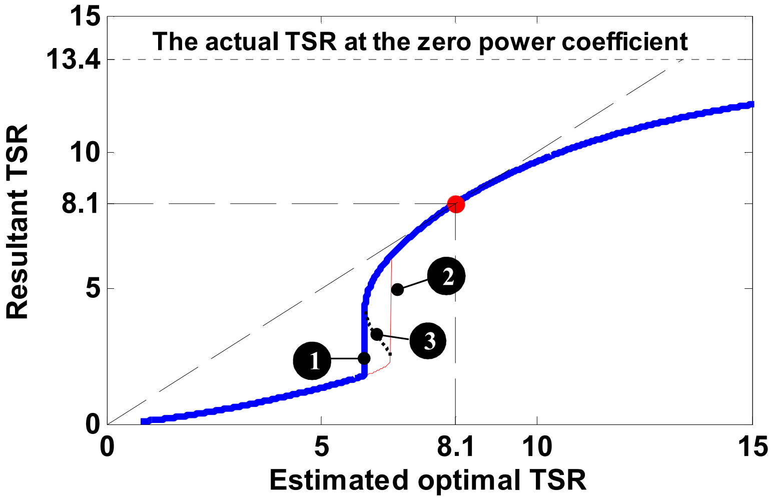

(a) $\lambda_{(res)}$ versus $\lambda_{0(est)}$

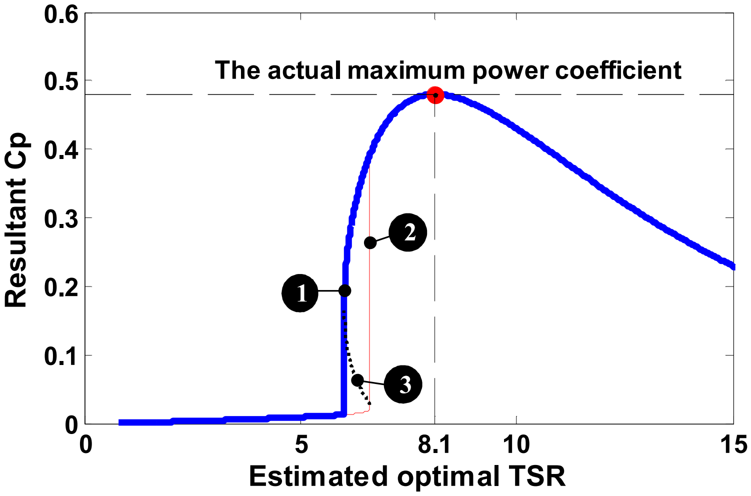

(a) $C_{p(res)}$ versus $\lambda_{0(est)}$

Fig. 8.15 The $\lambda_{(res)}$ versus $\lambda_{0(est)}$ (a) and the $C_{p(res)}$ versus $\lambda_{0(est)}$ (b) characteristics in the case with "TSR error only".

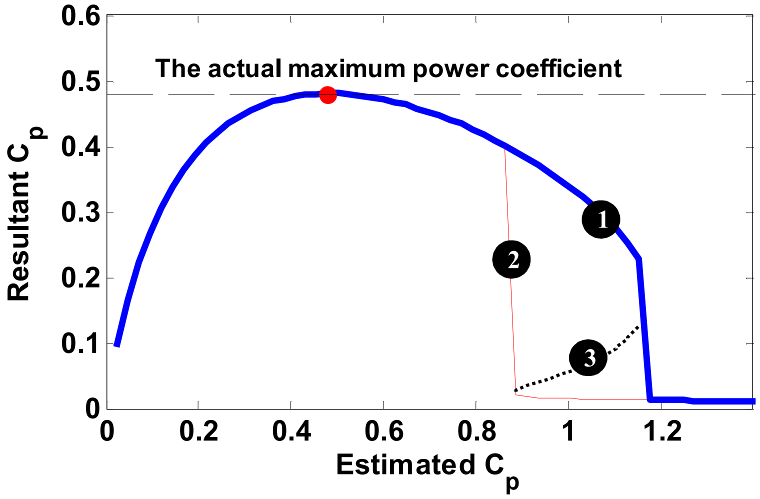

Fig. 8.16 The $C_{p(res)}$ versus $C_{p0(est)}$ characteristic in the case with "C_p errors only".

Note that the case with "TSR error only" in Fig. 8.15 corresponds to the set of curves highlighted with a solid-line box in Fig. 8.14 with the $C_{p0(est)}/C_{p0(act)}$ ratio equal to 1, whilst the case with "C_p error only" in Fig. 8.16 corresponds to the curves marked with a dashed-line box in Fig. 8.14 with the ratio of $\lambda_{0(est)}/\lambda_{o0(act)}$ equal to 1. In both Fig. 8.15 and Fig. 8.16, Curve 1 corresponds to the stable operation points with the higher resultant C_p in the cases with two stable operation points in Fig. 8.14, while Curve 2 corresponds to the stable operation point with the lower resultant C_p and Curve 3 corresponds to the unstable operation point.

For the sample actual C_p characteristic, the actual optimal *TSR* is 8.1 and the no-load *TSR* is 13.4. In Fig. 8.15 it can be seen that the estimated optimal *TSR* which the control algorithm uses is different from the resultant *TSR*, except the case where the estimated optimal *TSR* is identical to the actual optimal *TSR*. When the estimated optimal *TSR* is different from the actual optimal *TSR*, the resultant *TSR* is also different from the actual optimal *TSR* and the corresponding resultant C_p is reduced. Note that the change of the resultant TSR becomes much larger and more sensitive in the region where the estimated optimal *TSR* varies between 6 and 7, where the bifurcation produces two stable and one unstable operation points.

In the case with "C_p error only", the resultant C_p versus the estimated C_p is plotted in Fig. 8.16. The estimated maximum C_p is different from the resultant C_p, except when the estimated maximum C_p is identical with the actual maximum C_p of 0.48. When the estimated maximum C_p is different from the actual maximum C_p, the resultant C_p becomes lower than the actual maximum C_p. The most sensitive region is where the $C_{p0(est)}/C_{p0(est)}$ ratio is between 1.8 and 2.4, and the curve is bifurcated into the cases of two stable and one unstable operation points as noted in Fig. 8.14.

The power reduction for "TSR error only" is shown in Fig. 8.17, and the power reduction with "C_p error only" is shown in Fig. 8.18.

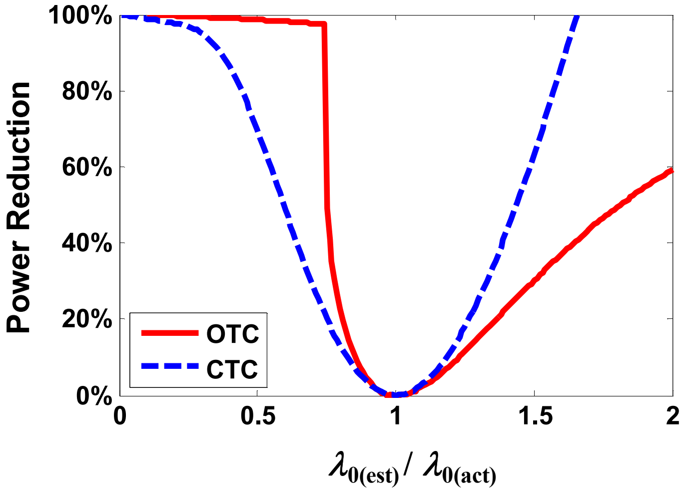

Fig. 8.17 Comparison of power reduction (%) vs. $\lambda_{0(est)}/\lambda_{o0(act)}$ in the case with "TSR error only" for the CTC and the OTC strategies

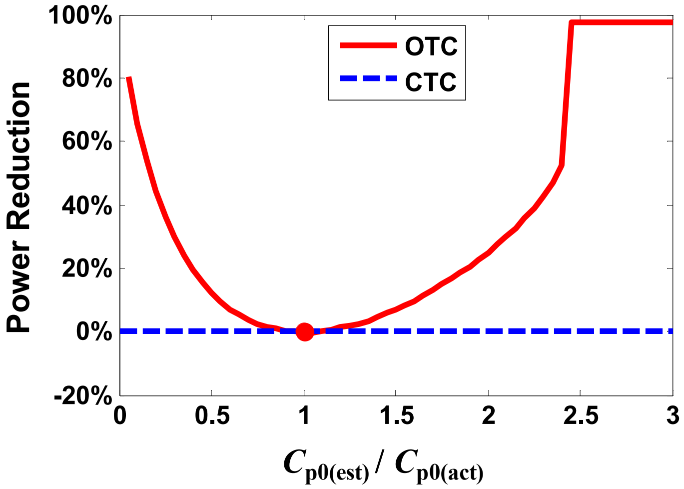

Fig. 8.18 Comparison of power reduction (%) vs. $C_{p0(est)}/C_{p0(est)}$ in the case with "C_p error only" for the CTC and the OTC strategies

In Fig. 8.17, the power reduction is zero at $\lambda_{0(est)}/\lambda_{o0(act)}= 1$ (no TSR error) and it increases with the TSR error for the two control strategies. For small errors, (±10%), where the ratio of $\lambda_{0(est)}/\lambda_{o0(act)}$ varies from 0.9 to 1.1, the power reduction varies from 0 up to 4%

for the control strategies. This is the region with the lowest sensitivity on the power reduction due to the TSR error. It should be noted that the power reduction of the OTC strategy changes faster and is generally greater than that of the CTC strategy when the ratio of $\lambda_{0(\mathrm{est})}/\lambda_{\mathrm{o}0(\mathrm{act})}$ varies from 0 to 1. However, this situation is reversed when the ratio of $\lambda_{0(\mathrm{est})}/\lambda_{\mathrm{o}0(\mathrm{act})}$ is above 1, where the power reduction of the OTC strategy becomes less sensitive than that of the CTC strategy.

In Fig. 8.18, the power reduction remains at zero for all C_p errors for the CTC strategy. For the OTC strategy, the power reduction is zero when $C_{\mathrm{p}0(\mathrm{est})}/C_{\mathrm{p}0(\mathrm{est})} = 1$ (no C_p error), and then increases with the C_p error. For small errors (the ratio of $\lambda_{0(\mathrm{est})}/\lambda_{\mathrm{o}0(\mathrm{act})}$ varying between 0.9 to 1.1), the power reduction varies from 0 up to 0.15% for the OTC strategy.

In addition, by comparing Fig. 8.17 and Fig. 8.18, it can be seen that: for the OTC strategy, the power reduction is affected by the TSR error, the C_p error and the shape of the actual C_p curve; while for the CTC strategy, the power reduction is only due to the TSR error and the shape of the actual C_p curve. Generally, the TSR error is more sensitive on the power reduction for both strategies.

The contour plots of the power reduction with the changes of $C_{\mathrm{p}0(\mathrm{est})}/C_{\mathrm{p}0(\mathrm{act})}$ and $\lambda_{0(\mathrm{est})}/\ \lambda_{0(\mathrm{act})}$ for the OTC strategy are provided in Fig. 8.19 for the two stable operating points in Fig. 8.14.

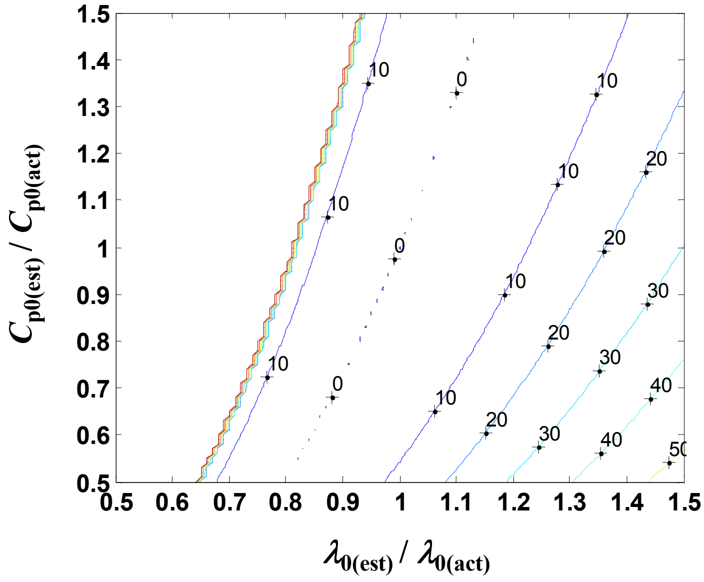

(a) Contour of the power reduction using the lower output power operating point in Fig. 8.14.

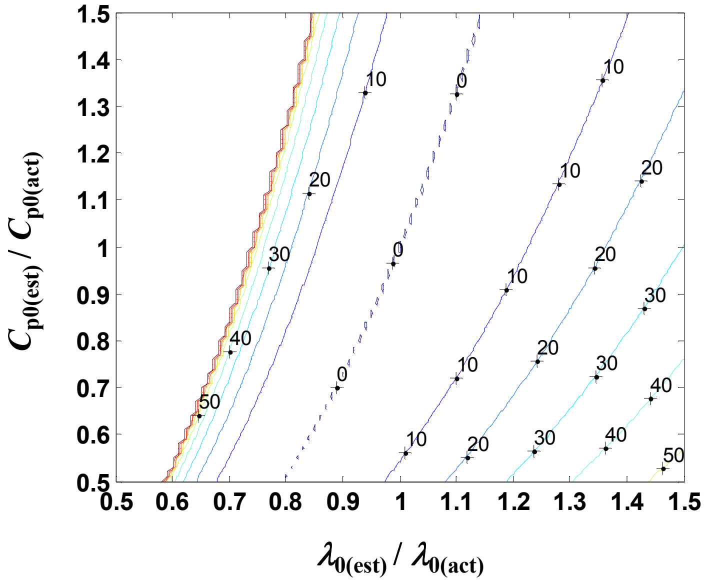

(b) Contour of the power reduction using the higher output power operating point in Fig. 8.14.

Fig. 8.19 The contour plot of power reduction (%) as a function of $C_{p0(est)}/C_{p0(act)}$ versus $\lambda_{0(est)}/\lambda_{0(act)}$ for the OTC strategy

The parameter sensitivity of the power reduction (PR) for the OTC strategy is summarised in Fig. 8.20 based on the control plots in Fig. 8.19. This shows the "power reduction sensitive", the "power reduction less sensitive" regions and the zero-power-reduction line.

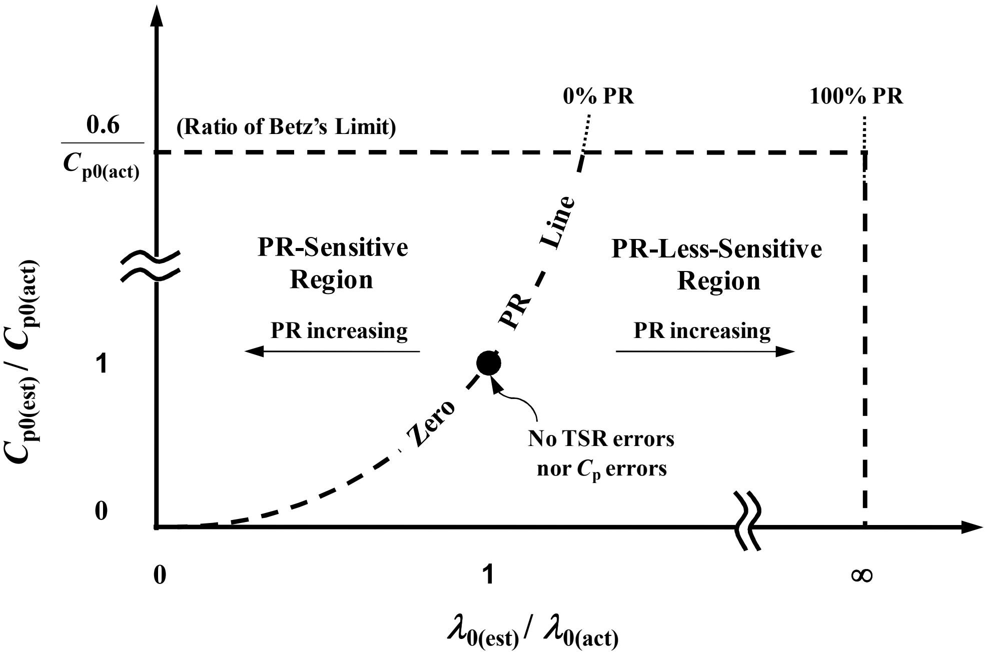

Fig. 8.20 The parameter sensitivity of power reduction for the OTC strategy.

8.4. Summary

In this chapter, the steady-state parameter sensitivity of two MPPT control strategies are analysed based on a typical turbine C_p curve. It is assumed that the shape of the turbine C_p curve is known accurately but not the values of the optimal TSR and the maximum C_p. An investigation of the relationships between the output power of a wind turbine and the error of the estimated optimal TSR $\lambda_{0(est)}$ and the estimated optimal maximum power coefficient $C_{p0(est)}$ is provided based on the constant TSR control (CTC) and the optimal torque control (OTC) strategies.

For the CTC strategy (see Fig. 8.9), the power reduction depends on the error of the estimated optimal TSR $\lambda_{0(est)}$. The error of the estimated optimal maximum power coefficient $C_{p0(est)}$ does not affect the output power for this control strategy. The zero-power-reduction line for the CTC strategy appears when the estimated optimal TSR $\lambda_{0(est)}$ equals to the actual optimal TSR $\lambda_{0(act)}$ (or when $\lambda_{0(est)} / \lambda_{0(act)}=1$).

For the OTC strategy (see Fig. 8.20), the power reduction is decided by the error of the estimated optimal TSR $\lambda_{0(est)}$, as well as the error of the estimated maximum C_p, $C_{p0(est)}$. The zero-power-reduction line for the OTC strategy is a line of constant ratio of C_p / λ_o^3.

Chapter 9. Conclusions and Suggestions

9.1. Dynamic Studies of the Inertia Effects on MPPT

In the first part of the thesis, a physical understanding of the effects of inertia on the average output power of wind turbines subjected to varying wind speed conditions is provided. It was assumed that the optimal torque control form of maximum power point tracking is used in a wind turbine. An analytical equation of the small-signal power reduction due to the inertia of wind turbine is derived and verified by the computer simulations. It was shown that the analytical equation can be used to quickly estimate the power reduction of a given wind turbine under varying wind conditions.

Firstly, a dynamic model of a wind turbine system was developed and used to verify the analytical results. An empirical turbine coefficient of performance curve was utilised in this study.

The concept of the small-signal turbine time constant is introduced to denote the response time of a wind turbine system with inertia under a small step change in wind speed and an analytical equation for it is derived under the optimal load condition. The equation has shown that the turbine time constant is inversely proportional to the wind speed. The turbine time constant at rated wind speed is defined as the natural time-constant τ_o. It is shown that the natural time constant varies with turbine power rating as roughly $\tau_o \propto P_{\text{rated}}^{0.3}$. The natural time constant has a value of about 1s for small wind turbines and up to about 10s for large wind turbines.

The analytical equation of the small-signal power reduction with infinite turbine inertia is then derived as a function of the ratio of the variance to the squared average wind speed, and verified by the simulation using square, triangular and sinusoidal wind speed variations. The analytical equation of the small-signal power reduction for finite values of inertia is then derived as the product of the power reduction with infinite inertia and a scaling factor which is a function of the product of the turbine time constant at the average wind speed and the equivalent frequency of wind speed. Real wind data recorded by an anemometer was utilised to verify the analytical equation of the power reduction for both the cases with infinite inertia and finite inertia, and the relationship of the power reduction with the wind and turbine characteristics was further analysed. Finally, some limited experimental validation of the model used in the above simulation was described.

9.2. Steady-State Studies of the Parameter Sensitivity on MPPT

The second part of the work investigated the effect of parameter errors on the steady-state output power of a wind turbine for two maximum power point tracking control strategies: constant tip-speed ratio control (CTC) and optimal torque control (OTC). The power reduction with errors in the estimated maximum power coefficient and the estimated optimal tip-speed ratio is simulated based on an empirical power coefficient curve, and is shown graphically.

9.3. Suggestions for Future Research

A key assumption in this study is that steady-state operating speed of an infinite-inertia wind turbine is equal to the average speed of a zero-inertia wind turbine. This assumption was examined in Appendix C and shown to be valid for the modelled Cp versus TSR curve under small to medium sinusoidal wind speed variations. Given the importance of this assumption to the results in this thesis, it is recommended that further research be done into the validity of this assumption under a wider range of wind speed profiles.

In the dynamic study of the inertia effects on MPPT, the analytical equation of the power reduction under varying wind speeds was derived without considering that above rated wind speed the output power is no longer proportional to the cube of the wind speed, but instead is constant. Further study is needed to develop a more accurate dynamic model of a wind turbine system including the high-speed constant power operating region, and hence to improve the accuracy of the power reduction estimate.

Moreover, the experimental validation of the dynamic model of the wind turbine system can be further developed in order to verify the analytical results of the power reduction. For instance, tests can be done with two turbines which are identical except their inertia. This could be artificially increased on one turbine by adding a mass to the rotor.

Appendix A. Specifications of Commercial Wind Turbines

The following parameters for the commercial wind turbines are collected by Dr. David Whaley from the manufacturers' web sites.

Table A.1. The specifications of commercial wind turbines

Company	Model	Rated power (kW)	Rotor radius (m)	Rated speed (m/s)	C_{pmax}
Enercon	E33	330	16.7	13	0.5
	E44	900	22	17	0.5
	E48	800	24	14	0.5
	E53	800	26.5	13	0.49
	E70	2300	35.5	16	0.5
	E82	2000	41	13	0.5
Entegrity	EW15	50	7.5	11.3	-
Nordex	N80	2000	40	15	0.434
	N90	2300	45	13	0.436
	S70	1500	35	13	0.431
	S77	1500	38.5	13	0.411
	N90	2500	45	14	~0.43
GE	3.6sl	3600	55.5	14	-
	1.5sl	1500	38	14	-
	25xl	2500	50	12.5	-
Northern	NW100	100	10	15	-
Vestas	V52_UK	850	26	16	-
	V80_UK	2000	40	15	-
	V80_US	1800	40	15	-
	V82_UK	1650	41	13	0.46
	V82_UK	900/1650	41	13	0.46
	V90-2_UK	1800	45	12	-
	V90-2_UK	2000	45	13	-
	V90-3_UK	3000	45	15	-

Appendix B. Principles and Simulation of Over-Speed Protection

B.1. Principles of Over-Speed Protection

The over-speed protection needs to be taken into account in the analysis of the power reduction. This is because the maximum power point tracking only operates under a speed limit. Therefore, the output power is not the maximum value when the wind turbine operates at a wind speed above the speed limits.

Typical control strategies for over-speed protection include aerodynamic torque control, generator torque control, brake torque control and yaw orientation control (or furling control). Aerodynamic torque control basically regulates the aerodynamic torque through changing the geometry of blades in order to adjust the C_p curve to protect the wind turbine at high wind speeds, for instance using blade pitch control. Generator torque control adjusts the generator torque to slow the turbine to safe speeds by using the control of the AC/DC converter or the dump resistor (resistive load in series with a switch to ground). Brake torque control uses a mechanical brake system to stop the wind turbine at high wind speeds. Yaw orientation control changes the direction of the turbine away from the wind direction in order to reduce the turbine speed. This is commonly seen in small wind turbines.

Aerodynamic torque control, brake torque control and yaw control basically adjusts the turbine torque by mechanical regulation of the wind turbine. This can cause high noise levels, increased capital investment and maintenance costs. These mechanical methodologies of over-speed protection are commonly used in large wind turbines where the electrical methodology performs much slower due to their large inertia. In comparison, the electrical methodology of over-speed protection appears a better option for a small-scale wind generation system.

Reference [39] provides an electrical methodology of over-speed protection by regulating the duty-cycle of the switch in a switched-mode rectifier under an open-loop condition where the duty-cycle is used to change the generator torque, hence the turbine speed. Fig. B.1 shows the simulation results in this paper.

NOTE:
This figure is included on page 120 of the print copy of the thesis held in the University of Adelaide Library.

Fig. B.1.Turbine power and torque versus wind speed (a) and turbine speed versus wind speed (b) [18]

In Fig. B.1, the output power of the wind turbine follows the maximum power locus when the wind speed is lower than 12 m/s, and is kept constant at 1.5 kW from the wind speeds from 12 m/s to 25 m/s. The wind turbine is shutdown when wind speed goes higher than 25 m/s using a mechanical brake.

B.2. Simulation of Over-Speed Protection

Based on the above analysis, a simulation has been done with the sample 400 W wind turbine, where the trajectory of the generator torque versus generator speed in the direction of increasing wind speed is highlighted with the dotted lines.

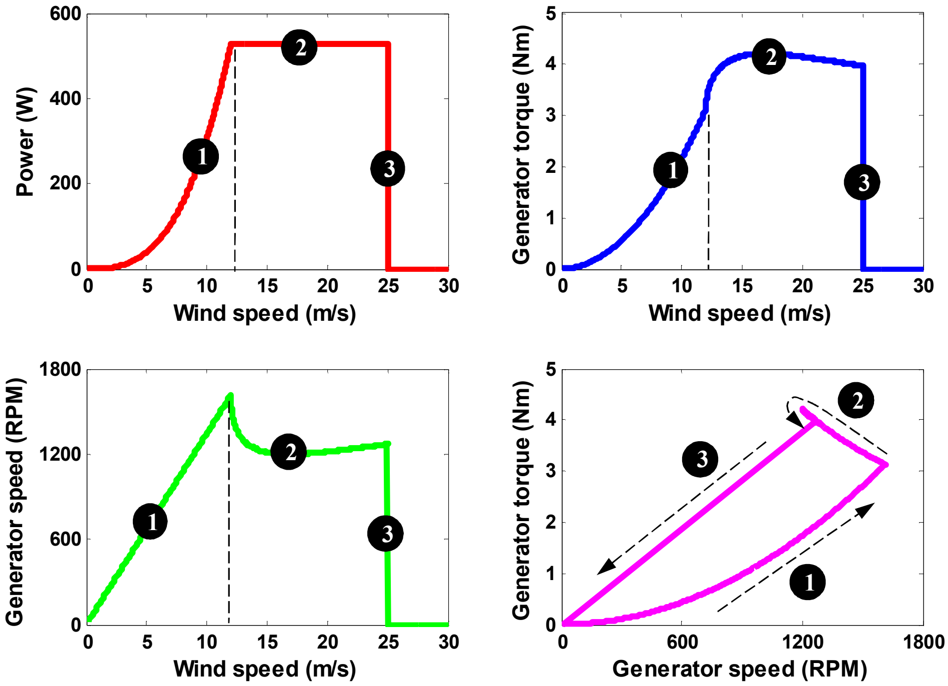

Fig. B.2 Generator Torque Control: the output power, generator torque, generator speed with the changes of wind speed and the generator torque versus generator speed with the increasing wind speed direction highlighted.

In Fig. B.2, it can be seen from the generator torque versus generator speed that, for a given generator speed there are more than one possible result of the generator torque, which correspond to the maximum power mode and the constant power mode respectively. Therefore, the generator torque versus generator speed characteristic is not sufficient to construct the Generator Torque Control model. Instead, the generator torque versus wind speed is required for the control, where the information of wind speed is needed.

In the above analysis of power reduction due to the inertia, the wind turbine operates with the MPPT control ($v \leq v_{\mathrm{rated}}$) and with the constant output power control ($v > v_{\mathrm{rated}}$). The wind speed limit, with which the wind turbine is shutdown, has not been involved in the investigation.

Appendix C. Average Turbine Speed Changes with Inertia

C.1. Introduction

In Chapter 4, an assumption that the turbine speed with infinite inertia is equal to the average turbine speed with zero inertia was made. In this appendix, this assumption was justified by a series of numerical simulations using the wind turbine system model.

C.2. Average Input and Output Power Reductions

The average turbine input power ($\overline{P_{in}}$) is a function of the power coefficient and the wind speed, which is obtained as

$$\overline{P_{in}} = \frac{1}{\mathrm{T}}\int_0^{\mathrm{T}} P_{in}(t)dt = \frac{1}{\mathrm{T}}\int_o^{\mathrm{T}} \frac{1}{2} C_p(t)\rho\pi R^2 \cdot v(t)^3\, dt \qquad \text{(c. 1)}$$

For a finite inertia wind turbine, the power coefficient $C_p(t)$ is time-varying when the wind speed changes. Only in the case of a constant value of power coefficient C_{pmax}, can Equation (c. 1) be changed into,

$$\overline{P_{in(max)}} = \frac{1}{2} C_{pmax} \rho \pi R^2 \cdot \frac{1}{\mathrm{T}} \int_o^{\mathrm{T}} v(t)^3 \, dt$$

$$= \frac{1}{2} C_{pmax} \rho \pi R^2 \cdot v_{CMC}^3 \qquad \text{(c. 2)}$$

However, in practice the power coefficient is less than the maximum value most of the time, $C_p(t) \leq C_{pmax}$, due to the fact that the turbine inertia delays the changing of the turbine speed. Therefore,

$$\overline{P_{in}} < \overline{P_{in(max)}} \qquad \text{(c. 3)}$$

Equations (c. 2) and (c. 3) show that a wind turbine of finite inertia is not able to capture the entire power available in the effective wind speed (v_{CMC}) in reality. The difference between the available input power and the actual input power then causes the reductiuon of the average turbine output power, due to

$$\overline{P_{in}} = \overline{P_{out}} \qquad \text{(c. 4)}$$

The reduction in the average input power then causes the reduction in the output power.

Under MPPT control, the optimal parameters (λ_o, C_{pmax}) are given by the controller. Therefore, the average output power ($\overline{P_{out}}$) is proportional to the cube-root mean-cube of turbine speed ($\overline{n_{J(CMC)}}$ or $\omega_{J(CMC)}$),

$$\overline{P_{out}} = \frac{1}{\mathrm{T}} \int_0^{\mathrm{T}} P_{out}(t) dt = \frac{1}{\mathrm{T}} \int_o^{\mathrm{T}} \frac{1}{2} \frac{C_{pmax}}{\lambda_o^3} \rho \pi R^5 \cdot \omega_J(t)^3 \, dt$$

$$= \frac{1}{2} \frac{C_{pmax}}{\lambda_o^3} \rho \pi R^5 \cdot \frac{1}{\mathrm{T}} \int_o^{\mathrm{T}} \omega_J(t)^3 dt$$

$$= \frac{1}{2} \frac{C_{pmax}}{\lambda_o^3} \rho \pi R^5 \cdot \omega_{J(CMC)}^3 \qquad \text{(c. 5)}$$

Therefore, the reduction in the average output power can be then obtained as,

$$\Delta P = \left(\overline{P_{out(J=0)}} - \overline{P_{out(J)}}\right)/\overline{P_{out(J=0)}}$$

$$= \left(\omega_{J=0(CMC)}^{3} - \omega_{J=0(CMC)}^{3}\right)/\,\omega_{J=0(CMC)}^{3} \qquad \text{(c. 6)}$$

According to the above analysis, the reduction of average output power is equivalent to the reduction of $\omega_{J(CMC)}^{3}$ which depends on the average turbine speed $\left(\overline{\omega_J}\right)$ and the maximum variation of turbine speed $\left(\Delta\omega_J\right)$ for a sinusoidal turbine speed waveform,

$$\omega_{CMC} = \sqrt[3]{\frac{1}{\mathrm{T}}\int_{o}^{\mathrm{T}} \omega(t)^3 dt} = \sqrt[3]{\frac{1}{T}\int_{0}^{T} \left(\omega_m + \Delta\omega_J \cdot \sin 2\pi f t\right)^3 dt}$$

$$= \sqrt[3]{\omega_m^3 + \frac{3}{2}\,\omega_m \Delta\omega^2} \qquad \text{(c. 7)}$$

where, it will be shown later that the average turbine speed is $\left(\overline{\omega_J}\right)$ affected by the shape of C_p (λ) curve, while the maximum variation of turbine speed $\left(\Delta\omega_J\right)$ is determined by the turbine inertia.

C.3. Turbine Speed with Infinite Inertia

Firstly, it should be noted that the “effective average wind speed” (v_{CMC}) is different from the concept of the “equivalent wind speed” which is a new concept introduced in this thesis. The equivalent wind speed is the scaling of the turbine speed, so the equivalent wind speed and the turbine speed are directly proportional in this thesis.

From a series of simulations, it is found that the average turbine speed of a finite inertia wind turbine is approximately constant at the average turbine speed of a zero inertia wind turbine as the natural time constant increases, which is shown in Fig. C. 1. This figure is based on a sinusoidal input wind speed of the mean value 8 m/s and maximum variation 3m/s.

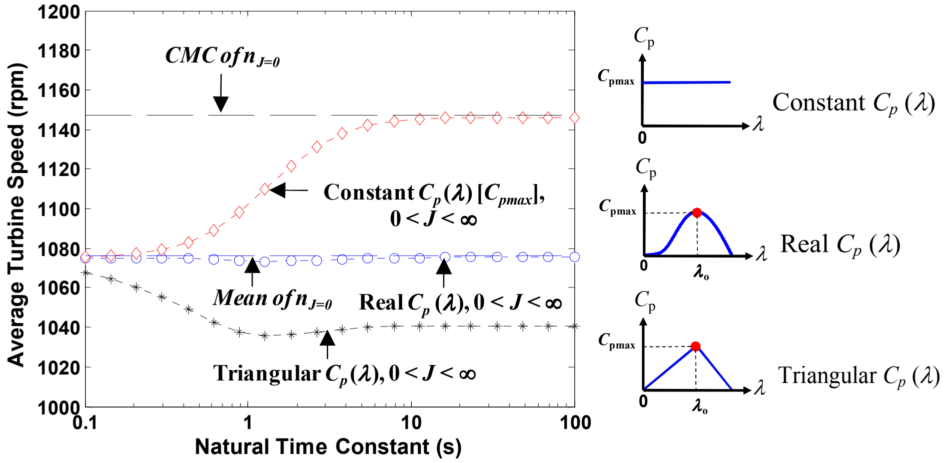

Fig. C. 1 Average turbine speed for the different $C_p(\lambda)$ curve profiles as the turbine inertia increases.

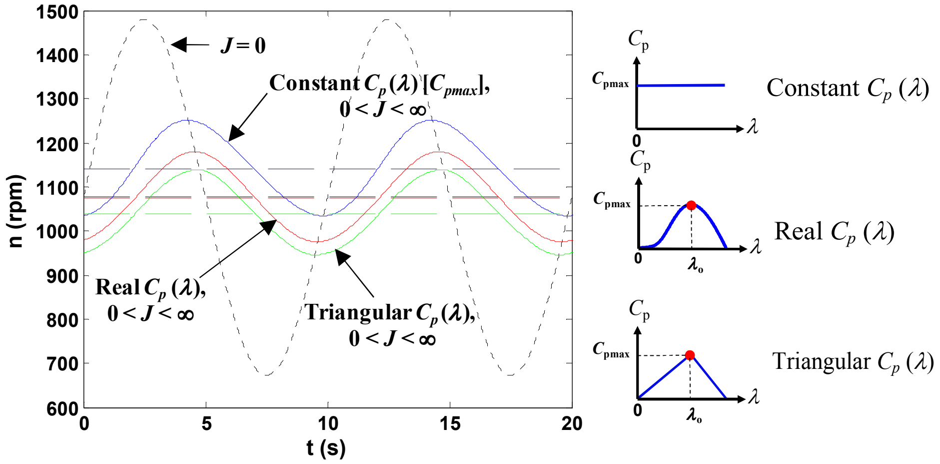

Fig. C. 2 A sample turbine speed variation with $\tau_o = 4.9$s for different $C_p(\lambda)$ profiles

As indicated above, the average turbine speed $(\overline{\omega_J})$ is affected by the shape of the $C_p(\lambda)$ curve, where the example $C_p(\lambda)$ model used in this thesis demonstrate an approximately constant average turbine speed as the turbine inertia increases. It can then be predicted that when the turbine inertia increases to infinity, the turbine speed will stay constant at the average turbine speed of zero inertia while the variation of turbine speed is reduced to zero. The equivalent wind speed of this turbine speed is thus equal to the average wind speed v_m. It then comes to the assumption in the thesis that the equivalent wind speed of infinite inertia is the average wind speed, or else an infinite inertia wind turbine operates at the average speed of a zero inertia wind turbine.

Fig. C. 1 also shows that the average turbine speed for a constant $C_p(\lambda)$ [C_{pmax}] wind turbine increases from the average turbine speed, for a zero inertia wind turbine, to the cube-root mean-cubed turbine speed. The increase of the average turbine speed then compensates for the decrease in the turbine speed maximum variation caused by the inertia (see Equation (c.7)). Thus the cube-root mean-cubed turbine speed for a constant $C_p(\lambda)$[C_{pmax}] wind turbine does not change as the inertia increases (see Fig. C. 3). Therefore, no power reduction due to inertia occurs for a constant $C_p(\lambda)$ [C_{pmax}] wind turbine.

In contrast, the average turbine speed of a real $C_p(\lambda)$ wind turbine does not change much as the inertia increases (it was assumed as a constant in this thesis). The reason for this is not understood. The drop of the turbine speed maximum variation with the increase of the inertia then causes the cube-root mean-cubed turbine speed to decrease (see Fig. C. 3) according to Equation (c.7). This then causes the total output power for finite inertia to be less than that for zero inertia. Both Equation (c.7) and the simulation results in Fig. C. 3 show that the cube-root mean-cubed turbine speed for a finite inertia has an upper limit set by the cube-root mean-cubed turbine speed for a zero inertia wind turbine (with the maximum Δv), and a lower limit set by the turbine speed for infinite inertia (or average turbine speed of a zero inertia wind turbine, with the zero Δv).

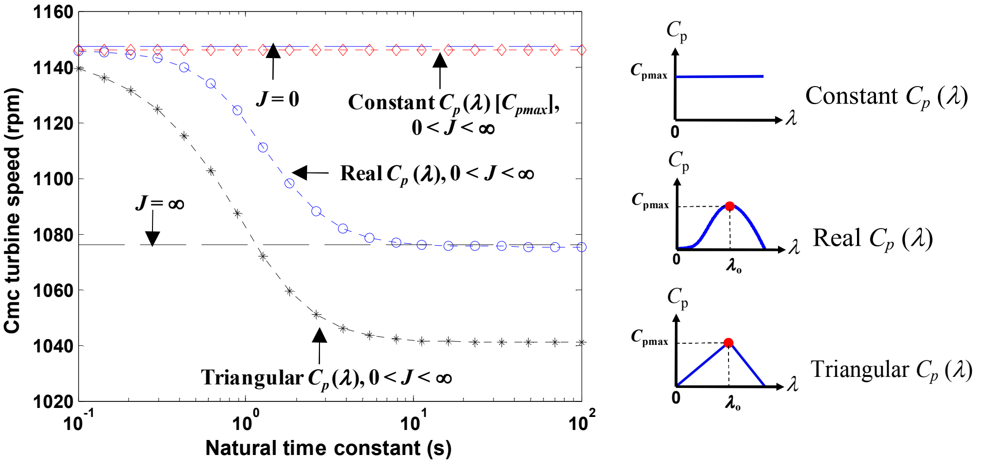

Fig. C. 3 Cube-root mean-cubed turbine speed for the different $C_p(\lambda)$ curve profiles as the turbine inertia increases.

The average output power is proportional to the the cube-root mean-cubed turbine speed according to Equation (c.5). Therefore, the decrease on the cube-root mean-cubed turbine speed then results in the reduction in the average output power as shown in Fig. C. 4,

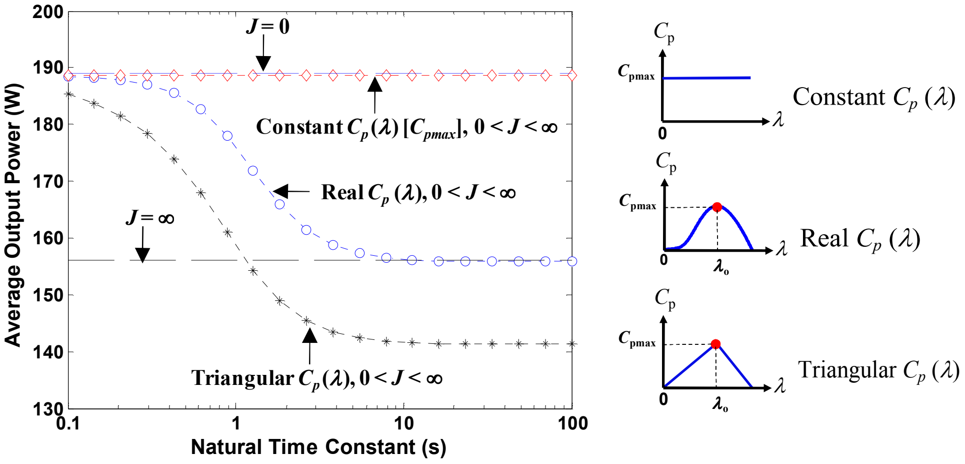

Fig. C. 4 Average output power for the turbine speed with the different $C_p(\lambda)$ curve profiles as the inertia increases.

Fig. C.4 shows the maximum average output power is obtained at zero inertia (no power reduction) while the minimum average output power is obtained at infinite inertia (maximum power reduction) for the real $C_p(\lambda)$ wind turbine.

C.4. Turbine Speed and Equivalent Wind Speed

The equivalent wind speed is defined in Chapter 5 in order to simplify the analysis. For a zero inertia wind turbine, it has,

$$\overline{P_{out(J=0)}} = \frac{1}{2} C_{pmax} \rho \pi R^2 \cdot v_{CMC}^3 \tag{c. 8}$$

where, v_{CMC} is the cube-mean cube-root of the actual wind speed.

From Equation (c. 5), the average output power for a finite inertia wind turbine is obtained as,

$$\overline{P_{out(J)}} = \frac{1}{2} C_{pmax} \rho \pi R^2 \cdot v_{J(CMC)}^3 \tag{c. 9}$$

where, $v_{J(CMC)}$ is the cube-mean cube-root of the equivant wind speed of a finite ineria wind turbine, which correspond to the cube-mean cube-root of the turbine speed $\omega_{J(CMC)}$ in Equation (c. 5).

Therefore, the power reduction defined by Equation (c.6) can be then written as,

$$\begin{aligned}\Delta P &= \left(\overline{P_{out(J=0)}} - \overline{P_{out(J)}}\right)/\overline{P_{out(J=0)}} \\ &= \left(v_{CMC}^3 - v_{J(CMC)}^3\right)/v_{CMC}^3 \qquad \text{(c. 10)}\end{aligned}$$

The above discussion explains the key assumptions and the background information which are not included in Chapters 4 and 5.

C.5. Suggestions

The average turbine speed for an infinite inertia wind turbine is affected by the $C_p(\lambda)$ curve profile. Based on the typical example of the $C_p(\lambda)$ model used in this study, the average turbine speed does not change much as the inertia increases. Therefore the assumption that the average turbine speed of an infinite inertia wind turbine is equal to the average turbine speed of a zero inertia wind turbine is appropriate under sinusoidal wind speed variations with a small to medium amplitudes. It is recommended that further research be conducted into this point (see the section on Future Research in Chapter 9).

A future study would be worthwhile to investigate how to quantify the effect of $C_p(\lambda)$ curve profile on the average turbine speed.

References

[1] World Wind Energy Association, "World total installed capacity in MW", available at www.renewableenergyfocus.com/view/2468/wwea-predicts-25-wind-energy-growth-in-2009/, 23rd July, 2009.

[2] F. D. Bianchi, H. De Battista, and R. J. Mantz. "Wind Turbine Control Systems: Principles, Modelling and Gain Scheduling Design", Advances in Industrial Control, Springer, 2006.

[3] O. Wasynczuk, D.T. Man, J.P. Sullivan, "Dynamic Behaviour of a Class of Wind Turbine Generators during Random Wind Fluctuations", *IEEE Transactions on Power Apparatus and System*, vol. PAS-100, June 1981, pp 2837-2845.

[4] S.R.J. Powles, "The effects of tower shadow on the dynamics of a horizontal-axis wind turbine", *Wind Engineering*, Vol. 7, 1983, pp 26-42.

[5] D.S.L. Dolan, P.W. Lehn, "Simulation Model of Wind Turbine 3p Torque Oscillations due to Wind Shear and Tower Shadow", *IEEE Transactions on Energy Conversion*, vol. 21, September 2006, pp 717-724.

[6] H.D. Battista, P.F. Puleston, "Sliding Mode Control of Wind Energy Systems with DOIG—Power Efficiency and Torsional Dynamics Optimization", *IEEE Transactions on Power Systems*, vol. 15, May 2000, pp 728-734.

[7] T. Thiringer, J. Dahlberg, “Periodic Pulsations from a Three-Bladed Wind Turbine”, *IEEE Transactions on Energy Conversion*, vol. 16, pp 128-133, June 2001

[8] T. Thiringer, J. Dahlberg, “Power quality measurements performed on a low-voltage grid equipped with two wind turbines”, *IEEE Transactions on Energy Conversion*, vol. 11, September 1996, pp 601-606.

[9] C. C. Johnson and R. T. Smith, “Dynamics of wind generators on electric utility networks”, *IEEE Transactions on Aerospace & Electronic Systems*, vol. AES-12*,* July 1976, pp 483-493.

[10] P.S. Dokopoulos, A.X. Patralexis, I.M. Manousaridis, "Improvement of power quality distortion in a grid caused by wind turbines," *8th International Conference on Harmonics and Quality of Power*, pp.917-922, vol.2, 1998

[11] S.A. Papathanassiou, M.P. Papadopoulos, "Dynamic behaviour of variable speed wind turbines under stochastic wind", *IEEE Transactions on Energy Conversion*, vol.14, no.4, pp.1617-1623, Dec 1999.

[12] J. Morren, J. Pierik, S.W.H. de Haan, “Inertial response of variable speed wind turbines”, *Electric Power Systems Research*, vol. 76, pp. 980-987, July 2006

[13] J. Morren, S.W.H. de Haan, W.L. Kling, J.A. Ferreira, "Wind turbines emulating inertia and supporting primary frequency control", *IEEE Transactions on Power Systems*, vol.21, no.1, pp. 433-434, Feb. 2006

[14] T. Nakamura, S. Morimoto, M. Sanada, Y. Takeda, “Optimum Control of IPMSG for Wind Generation System”, *Power Conversion Conference*, pp. 1435-1440, 2002.

[15] S. Morimoto, H. Nakayama, M. Sanada, Y. Takeda, “Sensorless Output Maximization Control for Variable-Speed Wind Generation System Using IPMSG”, *IEEE Transactions on Industry Applications*, vol. 41, No. 1, January/February 2005

[16] E. Koutroulis, K. Kalaitzakis, "Design of a maximum power tracking system for wind-energy-conversion applications"*,* *IEEE Transactions on Industrial Electronics*, vol.53, no.2, pp. 486-494, April 2006

[17] R. Datta, V.T. Ranganathan, "A method of tracking the peak power points for a variable speed wind energy conversion system"*,* *IEEE Transactions on Energy Conversion*, vol.18, no.1, pp. 163-168, Mar 2003

[18] G.D. Moor, H.J. Beukes, “Maximum Power Point Trackers for Wind Turbines”, *Power Electronics Specialists Conference, 2004. PESC 04. 2004 IEEE 35th Annual*, vol.3, pp. 2044-2049, June 2004

[19] A. Mirecki, X. Roboam, F. Richardeau, “Architecture Complexity and Energy Efficiency of Small Wind Turbines”, *IEEE Transactions on Industrial Electronics*, vol.54, no.1, pp.660-670, Feb. 2007.

[20] A.Z. Mohamed, M.N. Eskander, F.A. Ghali, “Fuzzy logic control based maximum power tracking of a wind energy system”, *Renewable Energy*, vol. 23, Issue 2, Pages 235-245, June 2001.

[21] K. Tan, S. Islam, “Optimum Control Strategies in Energy Conversion of PMSG Wind Turbine System without Mechanical Sensors”, *IEEE trans. on Energy Conversion*, vol. 19, Issue 2, pp. 392 – 399, June 2004.

[22] E. Muljadi, C.P. Butterfield, "Pitch-controlled variable-speed wind turbine generation", *IEEE Transactions on Industry Applications*, vol.37, no.1, pp.240-246, Jan/Feb 2001.

[23] N. A. Cutululis, M. Ciobotaru, E. Ceanga, “Real Time Wind Turbine Simulator Bas ed on Frequency Controlled AC Servomotor”, *The Annals of “Dunarea de Jos”* Un iversity of Galați, Fascicle III, 2004, pp. ISSN 1221 – 454X, available at www.ann.ugal.ro/eeai/archives/2002/15%20-%20Real%20time%20wind%20turbine%20simulator%20-%20Emil%20CEANGA%20.pdf on 17th November, 2009.

[24] L.A.C. Lopes, J. Lhuilier, A. Mukherjee, M.F. Khokhar, "A Wind Turbine Emulator that Represents the Dynamics of the Wind Turbine Rotor and Drive Train," *Power Electronics Specialists Conference*, pp.2092-2097, June 2005

[25] M. Monfared, H. M.Kojabadi, H. Rastegar, “Static and dynamic wind turbine simulator using a converter controlled dc motor”, *Renewable Energy*, 2008.

[26] H.M. Kojabadi, L. Chang, T. Boutot, "Development of a novel wind turbine simulator for wind energy conversion systems using an inverter-controlled induction motor", *IEEE Transactions on Energy Conversion*, vol.19, no.3, pp. 547-552, Sept. 2004

[27] J. Darbyshire and C. Nayar, “Modelling, Simulation and Testing of Grid Connected Small Scale Wind Systems”, *Australasian Universities Power Engineering Conference*, pp.1-6, 9-12th Dec. 2007.

[28] S. Heier, “Grid Integration of Wind Energy Conversion Systems”, John Wiley & Sons, 2nd Edition, 2006

[29] Matlab-Simulink V13, Mathworks 2006.

[30] Air X Specifications, available at www.solar-electric.com/PDF_files/sp_airx.pdf on 27th June, 2008.

[31] F.P. Beer, E.R. Johnston, Jr, “Mechanics for Engineers, Statics”, 3rd ed. McGraw-hi ll International Book Company, pp. 329-330, 1976.

[32] Specifications, available at www.westwind.com.au/images/ww%20brochure%20page2.pdf on 27th June, 2008.

[33] 1.5MW, 2.5MW and 3.6MW Wind Turbine Brochures, available at www.gepower.com/prod_serv/products/wind_turbines/en/index.htm on 27th June, 2008.

[34] Specifications, available at http://www.resec.cz/en/web/wind-energy/ on 29th, July, 2009.

[35] N90/2300kW Wind Turbine Specification, available at http://vetropark.org/d/59743/d/nordex_n80-n90_gb.pdf on 29th, July, 2009.

[36] K. Kaiser, W. Langreder, H. Hohlen and J. Højstrup, "Turbulence Correction for Power Curves ", available at www.springerlink.com/content/u30x2h58754k1235/fulltext.pdf, on 16th, November, 2009.

[37] Picologger ADC-11 Macro, available at www.picotech.com/support/topic1451.html on 16th, November, 2009.

[38] Plastics Comparison Table, available at http://www.machinist-materials.com/comparison_table_for_plastics.htm on 22nd June, 2009

[39] D.M. Whaley, W.L. Soong and N. Ertugrul, "Investigation of switched-mode rectifier for control of small-scale wind turbines", *Proceedings of IEEE Industry Applications Society Annual Meeting*, vol. 4, pp. 2849-2856, 2005.

[40] K. E. Johnson and L. J. Fingersh, "Methods for Increasing Region 2 Power Capture on a Variable Speed HAWT", Paper No. AIAA-2004-0350, *Proc.23rd ASME Wind Energy Symposium*, Reno, NV, pp. 103–113.

[41] D.H. Wood, A three-dimensional analysis of stall-delay on a horizontal-axis wind turbine. *Journal of Wind Engineering and Industrial Aerodynamics* **37** (1991), pp. 1–14.

[42] Hu D, Hua O, Du Z. A study on stall-delay for horizontal axis wind turbine. *Renewable Energy* 2006; **31**:821-836.

[43] Fingersh, L. J., and Carlin, P. W., 1998, ''Results from the NREL Variable-Speed Test Bed,'' Paper No. AIAA-98-0050, *Proc. 17th ASME Wind Energy Symposium*, Reno, NV, pp. 233–237